Advanced Functional Materials / Volume 34, Issue 11 / 2310195

Review | Full Access

Optimization Strategies of Covalent Organic Frameworks and Their Derivatives for Electrocatalytic Applications

Liyuan Xiao, Zhenlu Wang, Jingqi Guan

First published: 27 November 2023
https://doi-org.fgul.idm.oclc.org/10.1002/adfm.202310195
Citations: 6

Abstract

Covalent organic frameworks (COFs) are crystalline organic porous polymers that can be precisely integrated by building blocks to achieve pre-designed composition, components, and functions, making them a powerful platform for the development of molecular devices in the field of electrocatalysis. The precise control of channel/dopant positions and highly ordered network structures of COFs provide an ideal material system for the applications of advanced electrocatalysis. In this paper, the topological structure design and synthesis methods of COFs are reviewed in detail, and their design principles are deeply analyzed. In addition, the applications of COFs and their derivatives in the field of electrocatalysis are systematically summarized and the optimization strategies are proposed. Finally, the application prospects of COFs and their derivatives in electrocatalysis and the challenges that may be encountered in the future are prospected, providing helpful guidance for future research.

1 Introduction

Covalent organic frameworks (COFs) are a new type of crystalline porous materials connected by organic secondary building units (SBUs) through strong covalent bonds.[1] Due to the ordered pore structure, low density, structural measurability and diversity, relatively large porosity, easy functionalization, high chemical and thermal stability, and the certainty of pore wall chemical properties,[2] COFs show great potential in gas storage and separation,[3] sensing,[4] proton conduction,[5] energy storage,[6] photocatalysis[7] and electrocatalytic applications.[8] According to the connectivity and geometric shape of the selected organic

building units, 3D and 2D layered materials can be prepared.[9] According to the geometric structure and symmetry of the monomer, it can be divided into C1, C2, C3, C4, C6 and Td types.[10] 2D COFs extend along the *x* and *y* axes, forming a rigid layer-by-layer stacked network structure. Their uniqueness is that they not only have completely ordered π arrays but also have 1D open channels.[11] 3D COFs are selected by a specific ligand, allowing the backbone main chain to grow in the *x*, *y*, and *z* directions, which is usually accompanied by the mutual penetration and folding of the chain.[12] The construction unit of Td geometric structure or orthogonal geometric structure is often used to design 3D COFs network structures. An important feature is that all nodes and surfaces used to construct frame structure from the hole have complete accessibility.[13] One of the advantages of COFs is that they can combine building units with large ring-conjugated structures, mainly triazine, porphyrin, phthalocyanine, and pyridine to construct metalized COFs with different functions.[14]

Covalent triazine frameworks (CTFs) are nitrogen-containing aromatic heterocyclic rings with conjugated structures, which have good thermal stability, chemical corrosion resistance, and strong electronic affinity.[15] CTFs are rich in N atoms, which makes them easy to coordinate with transition metal ions. Porphyrin has a highly conjugated π electronic structure and excellent conductivity.[16] The N atom in the porphyrin center can coordinate with most transition metals to form stable complexes. Metalloporphyrin complexes have clear crystal structures and open metal active sites. Their structures are conducive to regulating electronic properties, enabling people to achieve strict catalytic control through structural modification of synthetic chemistry. Similar to porphyrin, phthalocyanine is an 18-electron macroconjugated compound composed of four isoindole units, which contain a special 2D π electron structure and can coordinate with transition metals to form stable metal phthalocyanine complexes.[17] Metal phthalocyanines have tunable structures and strong chemical stability. 2, 2′-bipyridine is a kind of compound with a bidentate chelating ligand, which can form complexes with many metal ions.[18] In addition, porphyrins and bipyridine organic units can coordinate different transition metal ions, and thereby they are suitable for constructing bimetallic COFs. In this type of bimetallic COFs, porphyrins can coordinate with Co and Fe, while bipyridine is usually coordinated with Re.

In 2005, Yaghi et al. synthesized topological organic polymers for the first time by using reversible chemical bonds of borate anhydride and borate ester (**Figure 1**).[19] In 2007, Yaghi et al reported the first case of 3D COF, which makes the development of COFs become a complete discipline in the field of crystal materials.[20] Later, with the growth of COF family, a series of Schiff bases, triazines, and imines appeared. In 2008, Thomas et al. prepared CTFs by ionic heat method.[21] In 2011, Wang et al. synthesized the first COF connected by an imide bond, which laid the foundation for the further application of COFs.[22] In 2016, Jiang et al. first synthesized hexagonal and tetragonal multicomponent COFs based on multicomponent [1+2] and [1+3] condensation systems.[23] So far, COFs have developed a mature concept both in structure and morphology control (Figure 1), which lays the

foundation for applications in various fields, especially in the field of electrocatalysis. The advantages of COFs have gradually become prominent, and have broad development prospects.

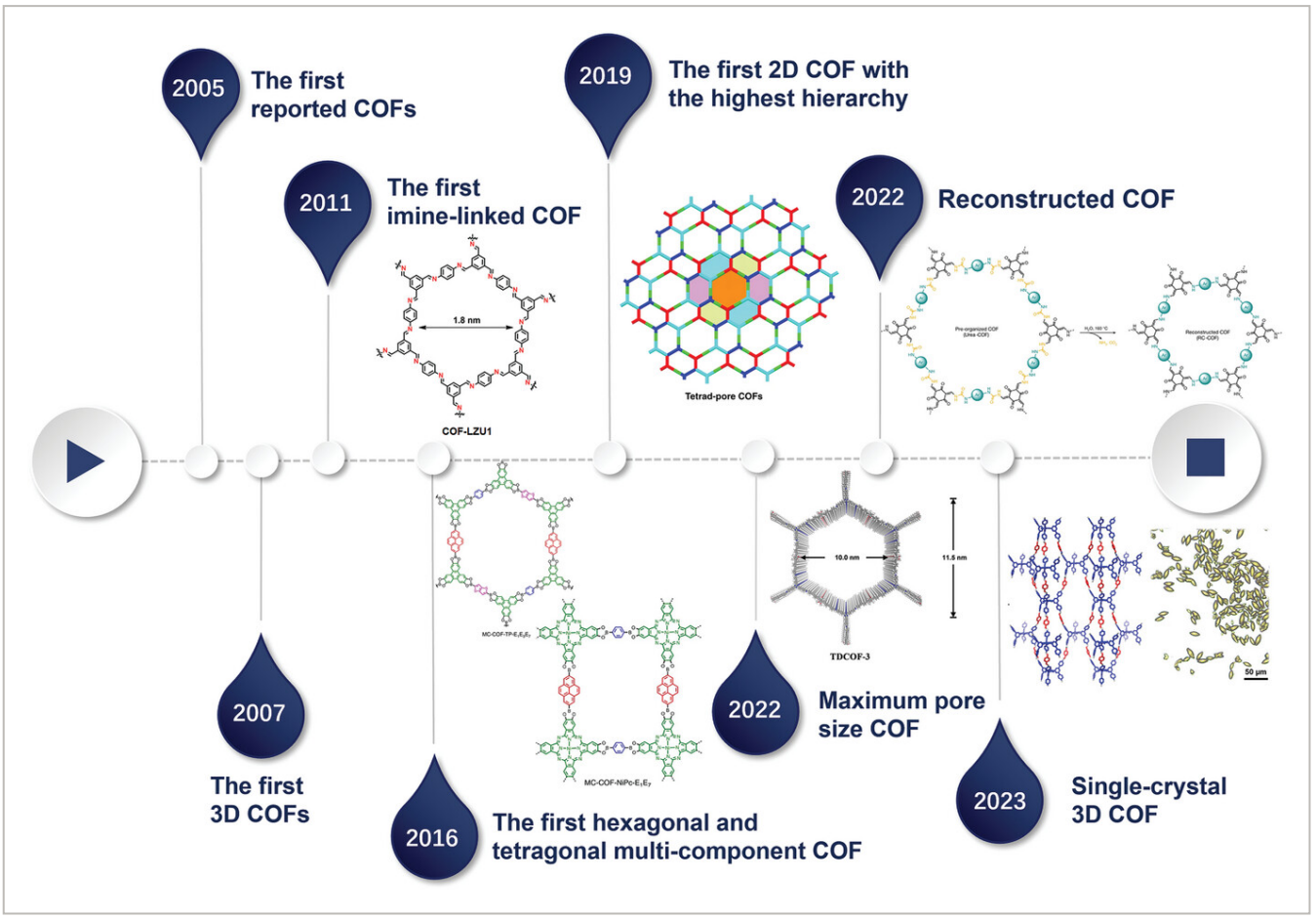

Figure 1

Open in figure viewer | PowerPoint

The development process of COFs. Reproduced with permission.[22] Copyright 2011, American Chemical Society. Reproduced with permission.[23] Copyright 2016, Springer Nature. Reproduced with permission.[24] Copyright 2019, Springer Nature. Reproduced with permission.[25] Copyright 2022, American Chemical Society. Reproduced with permission.[26] Copyright 2022, Springer Nature. Reproduced with permission.[27] Copyright 2023, American Chemical Society.

At present, electrocatalysis is one of the most effective methods to solve energy shortage and environmental pollution, including oxygen evolution reaction (OER),[28] hydrogen evolution reaction (HER),[29] oxygen reduction reaction (ORR)[30] and CO_2 reduction reaction (CO_2RR).[31] COFs have been widely used in the field of electrocatalysis due to their low skeleton density, strong stability, adjustable pore size, and molecular network. The hierarchical nanostructures with microchannels in COFs can be used as high-speed channels for ion diffusion and fast channels for OER and ORR. Mondal et al. synthesized metal-free C_4-SHz COF by solvothermal method.[32] The high specific surface area, porosity, and network

structure composed of π-conjugate units make C_4-SHz COF exhibit a low OER overpotential (η_{10}) of 320 mV. Based on Co-TpBpy, Zhao et al. synthesized macro-TpBpy with macropores and micropores (**Figure 2a**).[33] Co^{2+} coordinated with N to form the active site of OER, reducing its η_{10} to 380 mV. COFs can also bind to transition metal macrocyclic clusters (porphyrins, phthalocyanines, etc.). Lin et al. calculated the free energy and overpotential of ORR/OER on metal-porphyrin COFs and plotted the volcano plots of catalytic activities versus descriptors as shown in Figure **2b,c**.[34] To improve the electrical conductivity, COFs can be converted into COF-derived carbon materials by pyrolysis or other methods, in which heteroatoms can be doped to produce more active sites. Heteroatoms can effectively affect the charge distribution of surrounding carbon atoms, and the co-doping of heteroatoms with different electronegativity produces a synergistic effect.[35] Sulfur atom not only has a strong ability to replace carbon atoms but also has a strong synergistic effect with nitrogen.

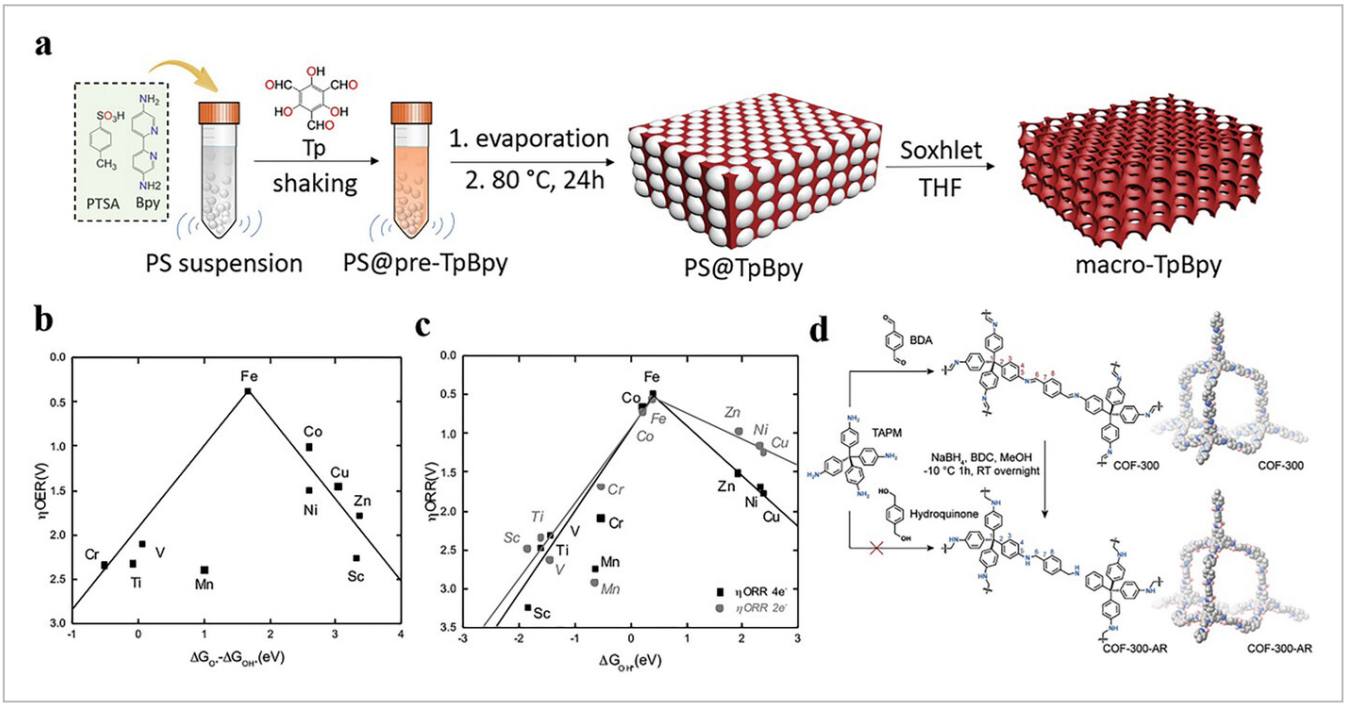

Figure 2

Open in figure viewer | PowerPoint

a) Synthesis of macro-TpBpy. Reproduced with permission.[33] Copyright 2019, American Chemical Society. Volcano plots of b) OER and c) ORR catalytic activities. Reproduced with permission.[34] Copyright 2017, Wiley-VCH. d) Synthesis of COF-300-AR. Reproduced with permission.[39] Copyright 2018, Elsevier Ltd.

COFs have an adjustable pore structure, which can adsorb a large amount of CO_2. The π–π stacking structure in COFs can promote charge transfer and greatly improve CO_2 reduction efficiency. Hence, COFs have an excellent catalytic effect on CO_2RR. In 2015, Lin et al. prepared COF-366-Co and COF-367-Co as electrocatalysts for the CO_2RR.[36] Since then, the electroreduction of CO_2 on COFs has attracted more and more attention. Metalized porphyrin has high electron transfer ability and can enhance the electrical conductivity of

COFs. Lu et al. prepared COF-366-$(OMe)_2$-Co@CNT by combining porphyrin-based COFs with carbon nanotubes for the CO_2RR, exhibiting FE_{CO} of 93.6% at −0.68 V versus RHE.[37] Phthalocyanine and transition metal are combined to form a stable metal phthalocyanine complex with an adjustable structure and stable chemical properties. Especially in CO_2RR, cobalt phthalocyanine has high selectivity for CO. Compared with monometallic COFs, bimetallic COFs can significantly improve the catalytic efficiency, but their synthesis is relatively difficult. Gong et al. prepared Fe/Cu-COFs and Ni/Zn-COFs for CO_2RR,[38] on which HER could be effectively inhibited and CO selectivity can be enhanced. Compared with metal-functionalized COFs, non-metallic COFs lack catalytic active sites, and the transfer efficiency of free electrons is relatively low, resulting in less research on non-metallic COFs in the field of CO_2RR. However, researchers found that non-metallic amine bond COFs and perfluorinated CTFs can catalyze CO_2RR and have high CO selectivity. Liu et al. prepared a non-metallic amine bond COF (COF-300-AR) (Figure **1d**), and its FE_{CO} could reach 80% at −0.85 V versus RHE.[39]

To set up a positive paradigm for the deep understanding of COFs toward advanced electrocatalysis, in this comprehensive review, we summarize the topological structure design of COFs in detail, including two parts: dimension and connection bond type, which fully reflects the designability of COF structure. Secondly, the common synthesis methods of COFs are summarized, including solvothermal synthesis, ionic liquid synthesis, microwave-assisted synthesis, mechanical grinding, and other synthesis methods. The advantages and disadvantages of several methods and the morphological characteristics of the synthesized COFs are briefly summarized. In addition, the applications of COFs and their derivatives in OER, HER, ORR, and CO_2RR are systematically reviewed from three perspectives: metal (including monometallic and polymetallic) based COFs, metal-free COFs, and derivatives. In particular, their optimization strategies of COFs for electrocatalytic applications are afforded. Finally, this review concludes with some of our insights about the research challenges and future development directions, hoping to arouse continuous innovations for advancing COFs and their derived functional materials for electrocatalytic applications. Compared to other reviews on COFs in the field of electrocatalysis,[40] this review paper has the following three characteristics: 1) We have detailedly discussed how to regulate the structures and properties of COFs by modulating the dimension and pore structure. 2) We have summarized the structure-activity relationship of COFs and their derivatives for the OER, HER, ORR, and CO_2RR. 3) We have proposed reasonable optimization strategies for regulating COFs and their derivatives in the field of electrocatalysis by combining detailed experimental analysis and theory research, providing guidance for future research.

2 Structure Design of COFs

2.1 Dimension of COFs

COFs are crystalline frame materials with periodically arranged building units through covalent bonds, and their spatial configuration can be designed in advance according to the size, shape, and expansion direction of the building units. According to the geometric structure and symmetry of the monomer, it can be divided into C1, C2, C3, C4, C6 and Td type. 2D COFs have a high π–π conjugate structure, and the topological network structure can be a hexagon, square, diamond, triangle, or mixed structure. As shown in **Figure 3**, the crystal forms corresponding to different topological structures are different, and the hexagonal channel is a common channel structure in 2D COFs. In 2013, Guo et al. reported that C3-symmetric hexaaminobenzophen (TPHA) reacted with C2-symmetric benzopyrene tetraone (PT) to obtain phenazine-linked 2D-COF (CS-COF), which has a rigid structure with a high plane in the lamellar.[41] In 2015, Mahmood et al. polymerized C3-symmetric hexaaminobenzene (HAB) and C3-symmetric hexaketone cyclohexane (HKH) to obtain layered 2D crystal structure C_2N-h2D.[42] Both 2D-COFs have periodic structures and hexagonal honeycomb pores. Using the combination of [C2+C4], the topological structure containing quadrilateral pores can be constructed. COFs with a topological structure are divided into two skeletons containing porphyrin and phthalocyanine. Lang et al. prepared sp^2 carbon conjugated porphyrin Por-sp^2 c-COF.[43] Huang et al. prepared 2D NiPc-COF containing phthalocyanine structure by reacting 2,3,9,10,16,17,23,24-octaaminophthalocyanine Ni (II) with tert-butylpyrene-tetraone (**Figure 4a**).[44] In addition, [C4+C2] combination can form 2D COFs with dual-pore topological structure, which is generally polymerized with two nodes centered on tetraphenylethylene (TPE). Zhao et al. synthesized 2D COFs containing two different pores using monomers with D_{2h} symmetry (4,4′,4′ ″,4′″ '-(ethene-1,1,2-tetrakis) tetraaniline (ETTA) and monomers with C2 symmetry (terephthalaldehyde) (Figure **4b**).[45] One is a hexagon, and the other is triangle. Triangular channel COFs can be obtained by [C6+C2] combination. Jiang et al. synthesized HFPTP-BPDA-COF with only triangular pores by polycondensation of 2,3,6,7,10,11-hexa (4-formylphenyl) triphenyl (HFPTP) and 1,1′-biphenyl-4,4′-diamine (BPDA) (Figure **4c**).[46]

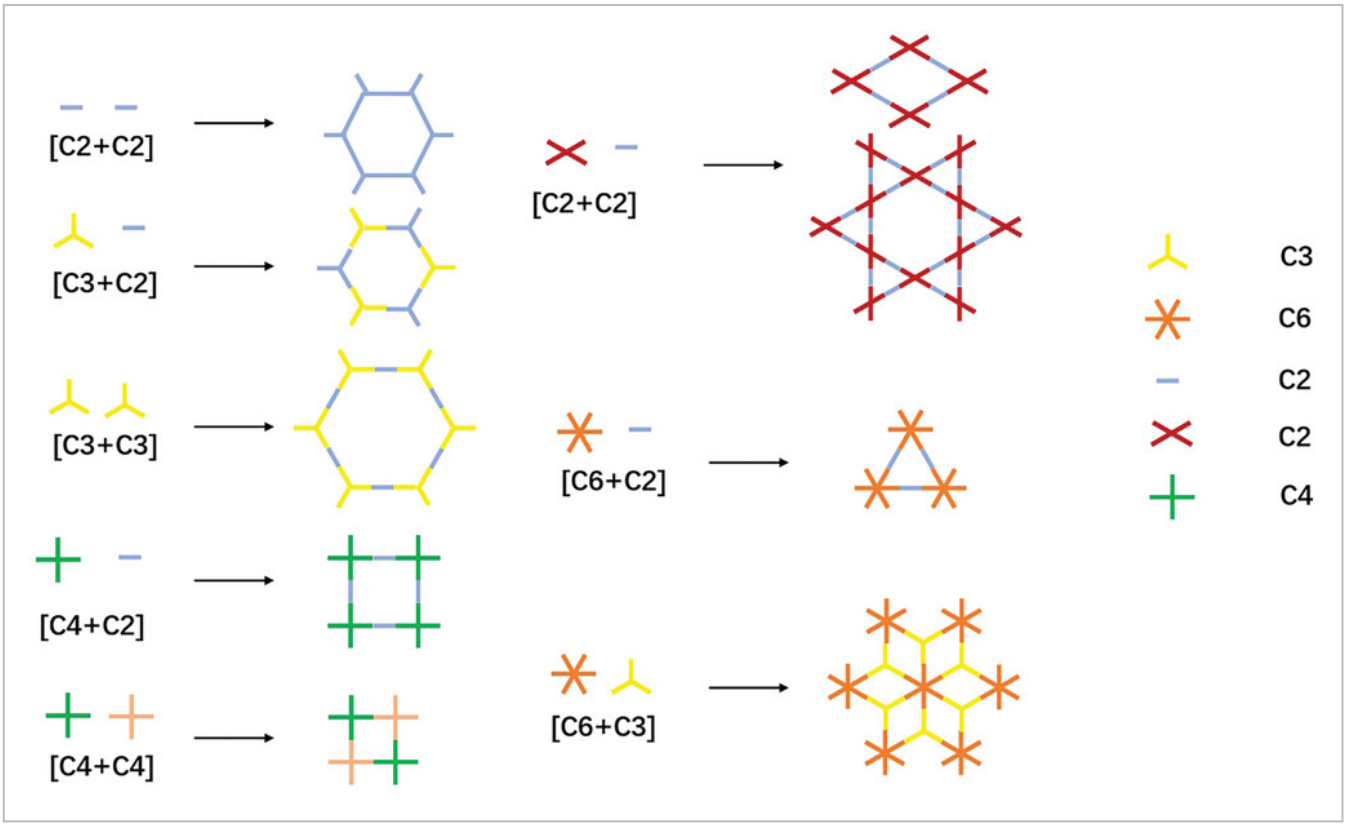

Figure 3

Open in figure viewer | PowerPoint

Topological structure of 2D COFs.

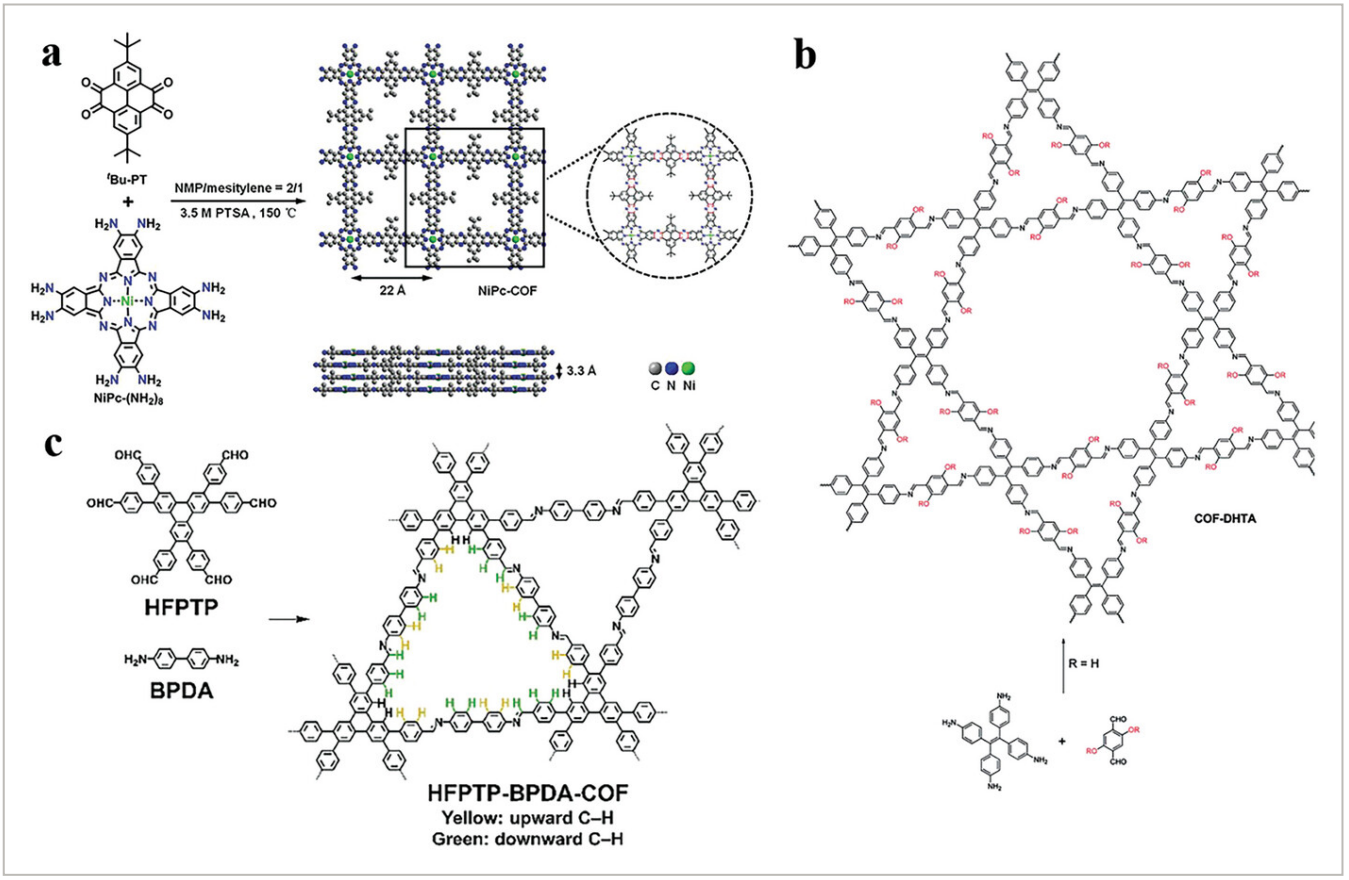

Figure 4

a) Synthesis of 2D conductive NiPc-COF. Reproduced with permission.[44] Copyright 2020, Wiley-VCH. b) Synthesis of a dual-pore COF. Reproduced with permission.[45] Copyright 2017, Royal Society of Chemistry. c) Synthesis of HFPTP-BPDA-COF. Reproduced with permission.[46] Copyright 2019, Wiley-VCH.

Different from 2D COFs, the pores of 3D COFs are interconnected. The common topological structures are shown in **Figure** 5a. The pore shapes of different topological structures are different, and the different pore structures would lead to different functions and applications. At present, the common 3D topological structures are ctn,[47] bor,[47] dia,[48] pts,[49] rra,[50] srs,[51] ffc,[52] lon,[53] stp,[54] acs,[55] tbo,[56] bcu,[57] fjh,[58] and ceq[59] (Figure 5b). [Td+C2] combination can obtain dia topological structure of diamond mesh. Liu et al. constructed SP-3D-COF-BPY with seven interpenetrating dia structures using orthogonal biplane spirodifluorene and bipyridine.[60] Gao et al. prepared a fully π-conjugated BUCT-COF-1 with a 13-fold interpenetrating dia topology.[61] Fang et al. constructed a non-interpenetrating dia topology, and the synthesis method is shown in **Figure** 6a.[62] This structure is mainly caused by the connection of tetrahedral and linear building units and the spatial steric effect. [Td+C4] can form pts topology, which is likely to form a mutual penetration structure. Lin et al. prepared 3D-Por-COF and 3D-CuPor-COF with double interpenetrating pts topology by [4+4] condensation reaction (Figure 6b).[49] Wang et al. prepared 3D-PdPor-COF with five-fold interpenetrating pts topology.[63] Later, Wang et al. synthesized acetylene-supported 3D COFs with seven-fold interpenetrating pts topology.[64] Fang et al. synthesized a new 3D COF with stp topological structure by solvothermal method, which was constructed using 2,3,6,7,14,15-hexa (4′-formylphenyl) tributene (HFTP) as a unit.[65] The acs topology is a triangular prism. Zhu et al. prepared 3D-CageCOF-1 with acs topological structure using Cage-6—NH_2 and 2,5-dihydroxy terephthalaldehyde (DHTPA) (Figure 5c).[66] Thomas et al. synthesized 3D SiCOF-5 with double interpenetrating srs topology with octahedral silicate as the center and ternary phthalate (Figure 5d).[51] Since the types of 3D ligands are limited, the number of topological types of 3D COFs is far less than that of 2D COFs.

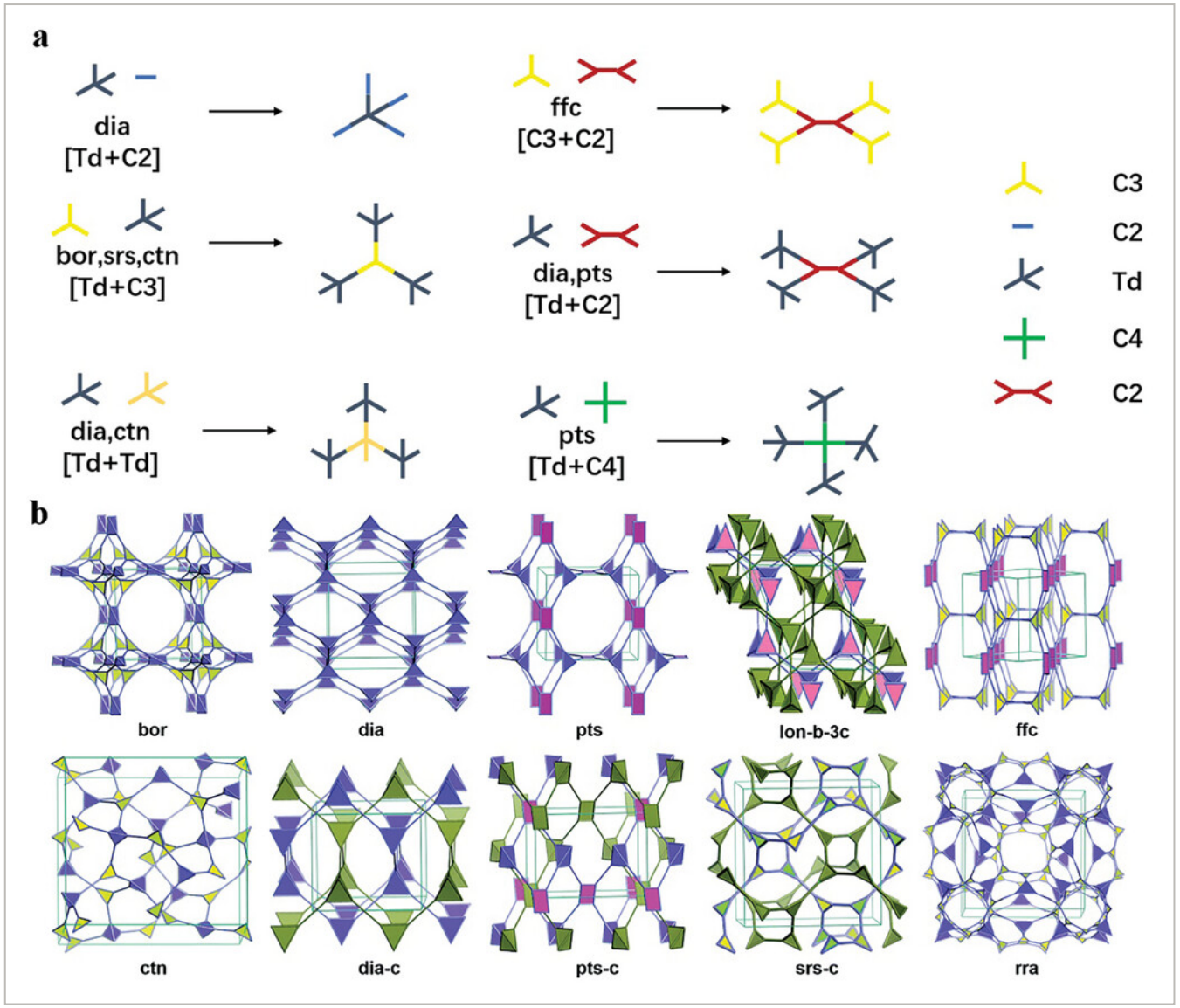

Figure 5

Open in figure viewer | PowerPoint

a) 3D topology design. b) 3D topological structure. Reproduced with permission.[67] Copyright 2020, Royal Society of Chemistry.

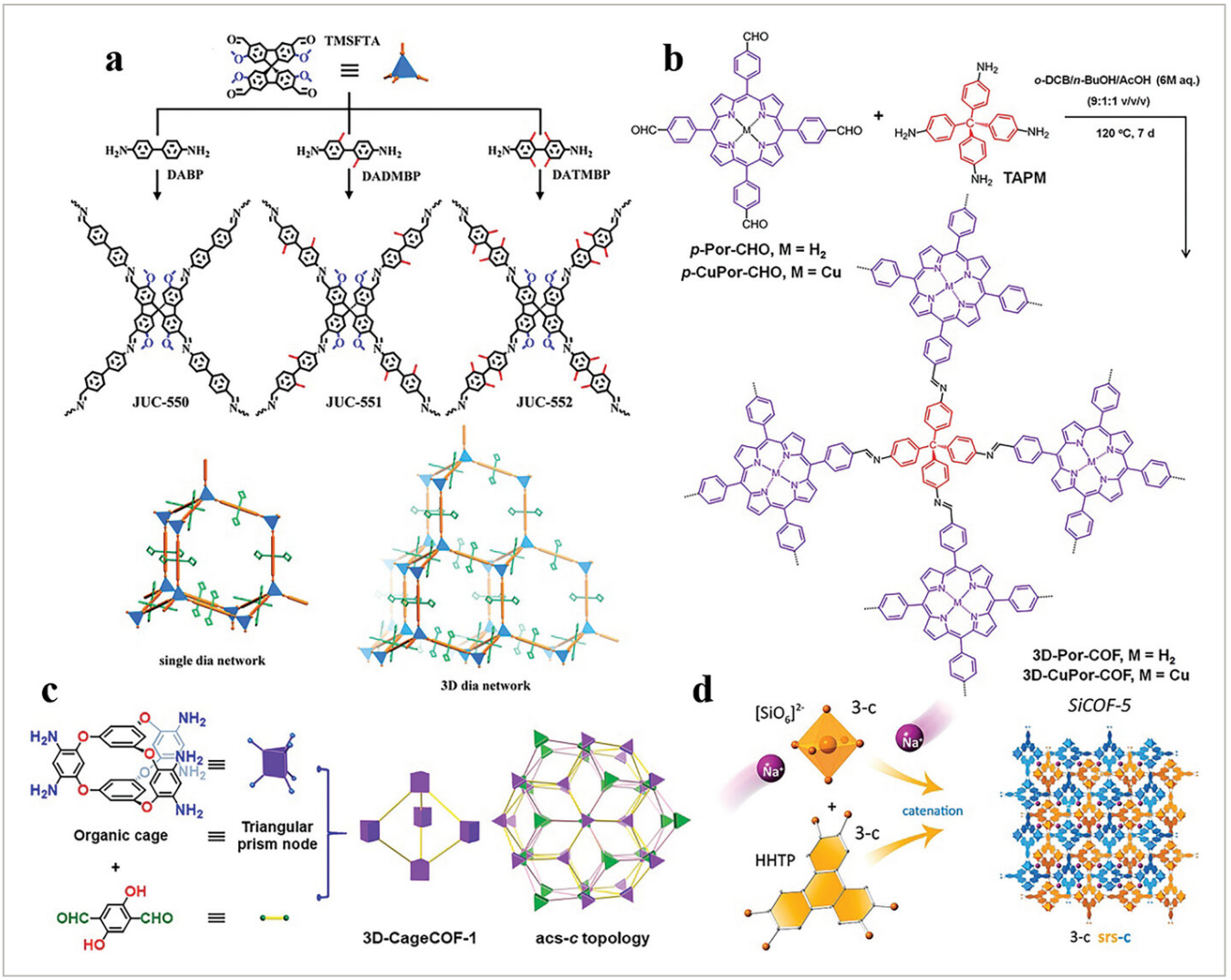

Figure 6

Open in figure viewer | PowerPoint

a) Synthesis and dia structure of JUC-500, JUC-551 and JUC-552. Reproduced with permission.[62] Copyright 2020, American Chemical Society. b) Synthesis of 3D-Por-COF and 3D-CuPor-COF. Reproduced with permission.[49] Copyright 2017, American Chemical Society. c) Synthesis of 3D-Cage COF-1. Reproduced with permission.[66] Copyright 2020, American Chemical Society. d) Synthesis of 3D SiCOF-5. Reproduced with permission.[51] Copyright 2018, American Chemical Society.

2.2 Type of Connection Linkages

2.2.1 Boron-Containing COFs

As mentioned above, Yaghi synthesized COFs with boron-oxygen bonds using borate anhydride and borate ester. Since then, the reactions of self-condensation of boric acid and dehydration condensation of boric acid with o-diol to form hexaborane and pentaborates have been widely used for the synthesis of COFs. In addition, tetraborate can also react with tert-butylsilane to form a borate ester bond. **Figure 7** illustrates a common structure containing boron bonds.[67] Borate ester bond promotes the formation of a planar skeleton

and promotes the stacking of DPP molecules. Feng et al. prepared 2D COF with a borate ester bond by linking porphyrin macrocycle with phenyl or naphthalene.[68] COFs based on boron-containing bond types such as boron-oxygen six-membered ring and borate ester have good thermal stability, low skeleton density, and large specific surface area. However, the boric acid bond is easily destroyed and even can be decomposed by water vapor in the air at room temperature.

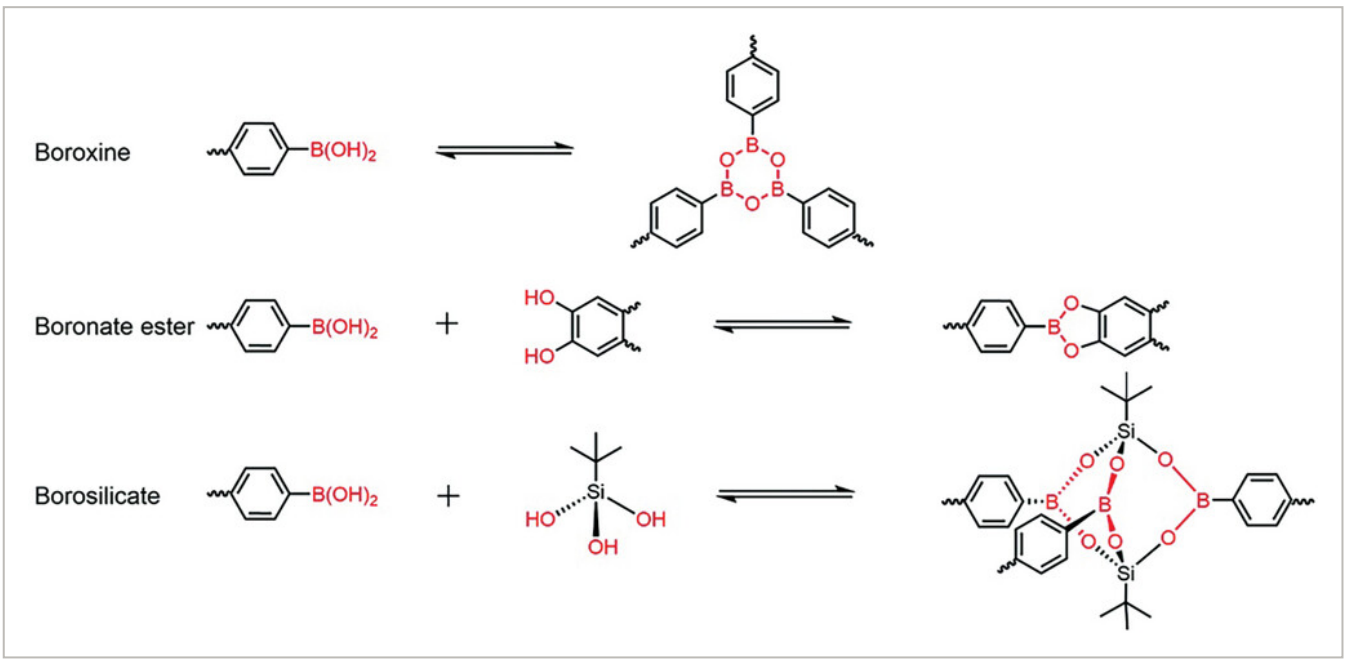

Figure 7

Open in figure viewer | PowerPoint

Boron-containing bond structure. Reproduced with permission.[67] Copyright 2020, Royal Society of Chemistry.

2.2.2 Schiff Base COFs

To solve the problem that boron-containing bonds are easy to destroy, researchers found COFs with an imide bond, acylhydrazone bond, hydrazine bond, and urea bond based on the Schiff base. The imine bond is the most widely used bond type, which is mainly produced by dehydration of primary amines and aldehydes. Qiu et al. prepared a TFPB-TA COF with an imine bond using 1,3,5-tri (4-formylphenyl) benzene (TFPB) and 2,4,6-tri (4-aminophenyl) −1,3,5-triazine (TTA) (**Figure** 8a).[69]

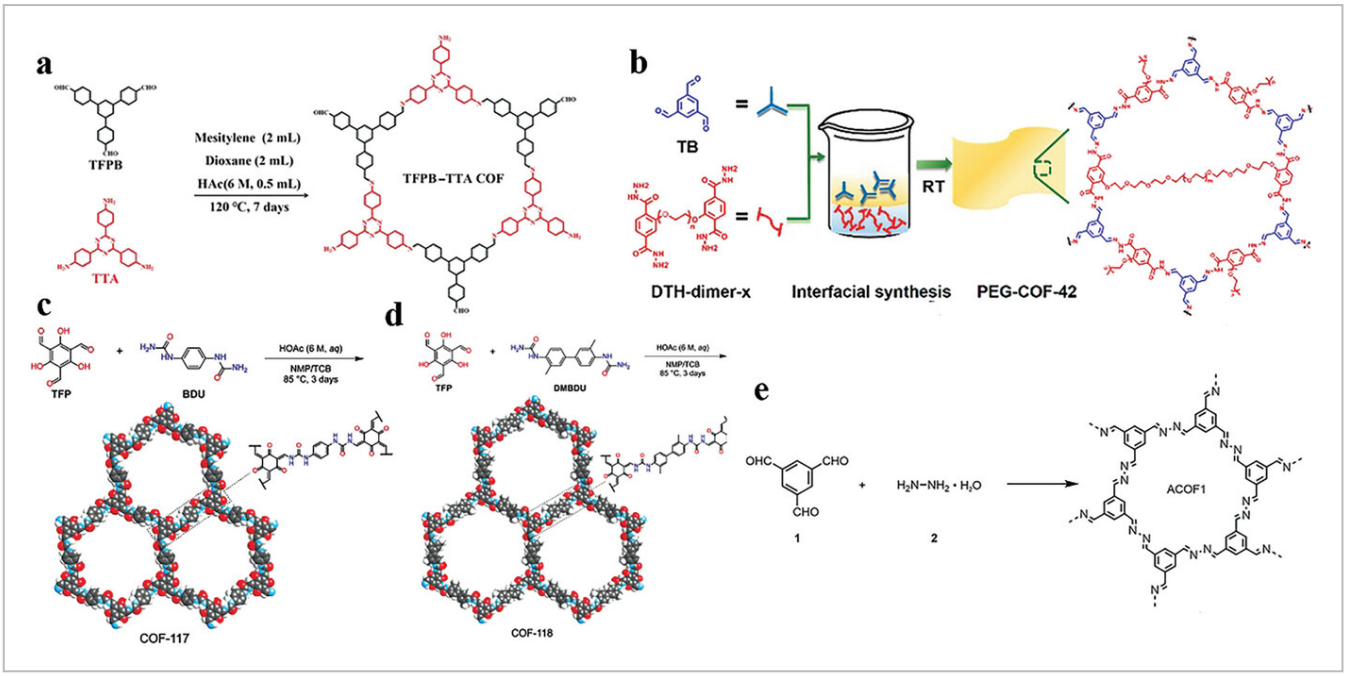

Figure 8

Open in figure viewer | PowerPoint

a) Synthesis of TFPB-TA COF. Reproduced with permission.[69] Copyright 2022, American Chemical Society. b) Synthesis of PEG-COF-42. Reproduced with permission.[70] Copyright 2020, American Chemical Society. Synthesis of c) COF-117 and d) COF-118. Reproduced with permission.[71] Copyright 2018, American Chemical Society. e) Synthesis of ACOF1. Reproduced with permission.[72] Copyright 2017, Wiley-VCH.

The structure formula of acylhydrazone bond is R_1-CH═N─NH─C(O)-R_2, which contains three groups of carbonyl, secondary amine, and tertiary amine. The lone pair electrons on the secondary amine form p-π conjugate with C ═ O and C ═ N, and thereby they are more stable than ordinary imide bonds. Guo et al. condensed 1,3,5-benzenetrialdehyde (TB) and 2,5-diethoxy-terephthaloylhydrazine (DTH) dimers to form PEG-COF-42 linked by acylhydrazone bond (Figure 8b).[70] The formation of acylhydrazone bonds is conducive to improving the performance of light response and steam response.

The urea bond is very similar to the acylhydrazone bond. Yaghi et al. condensed 1,3,5-formyl phloroglucinol (TFP) with 1,4-benzodiurea (BDU) and 1,1′- (3,3′-dimethyl- [1,1′-biphenyl]−4,4′-diphenyl) diurea (DMBDU) to produce COF-117 and COF-118, respectively (Figure 8c,d).[71] According to X-ray crystallography analysis, keto-enol structure alternation occurred after condensation. Jin et al synthesized ACOF1 and found that the molecular network structure formed acridine bond by FTIR analysis (Figure 8e).[72] Compared with boron-containing bonds, the N-containing bonds are not easy to destroy, but their thermal and chemical stability are still challenging.

2.2.3 Polyimide COFs

Polyimide (PI) COFs contain cyclic imide groups, and the synthesis process is shown in **Figure** 9a.[73] Compared with Schiff base COFs, PI-COFs with pentacyclic structures have better thermal and chemical stability, and they can also provide various skeletons and pores. Guo et al. heated melamine with pyromellitic dianhydride and naphthalene dianhydride to form PI-COF 201 and PI-COF 202 with polyimide bonds, respectively (Figure 9b).[74] The two COFs can emit strong fluorescence in appropriate solvents. Nagai et al. prepared four kinds of COFs by combining aromatic triamine and aromatic dianhydride (Figure 9c).[75] Density functional theory (DFT) calculations showed that the imide bond will form at a certain angle, which will break the 2D symmetry and reduce the pore width.

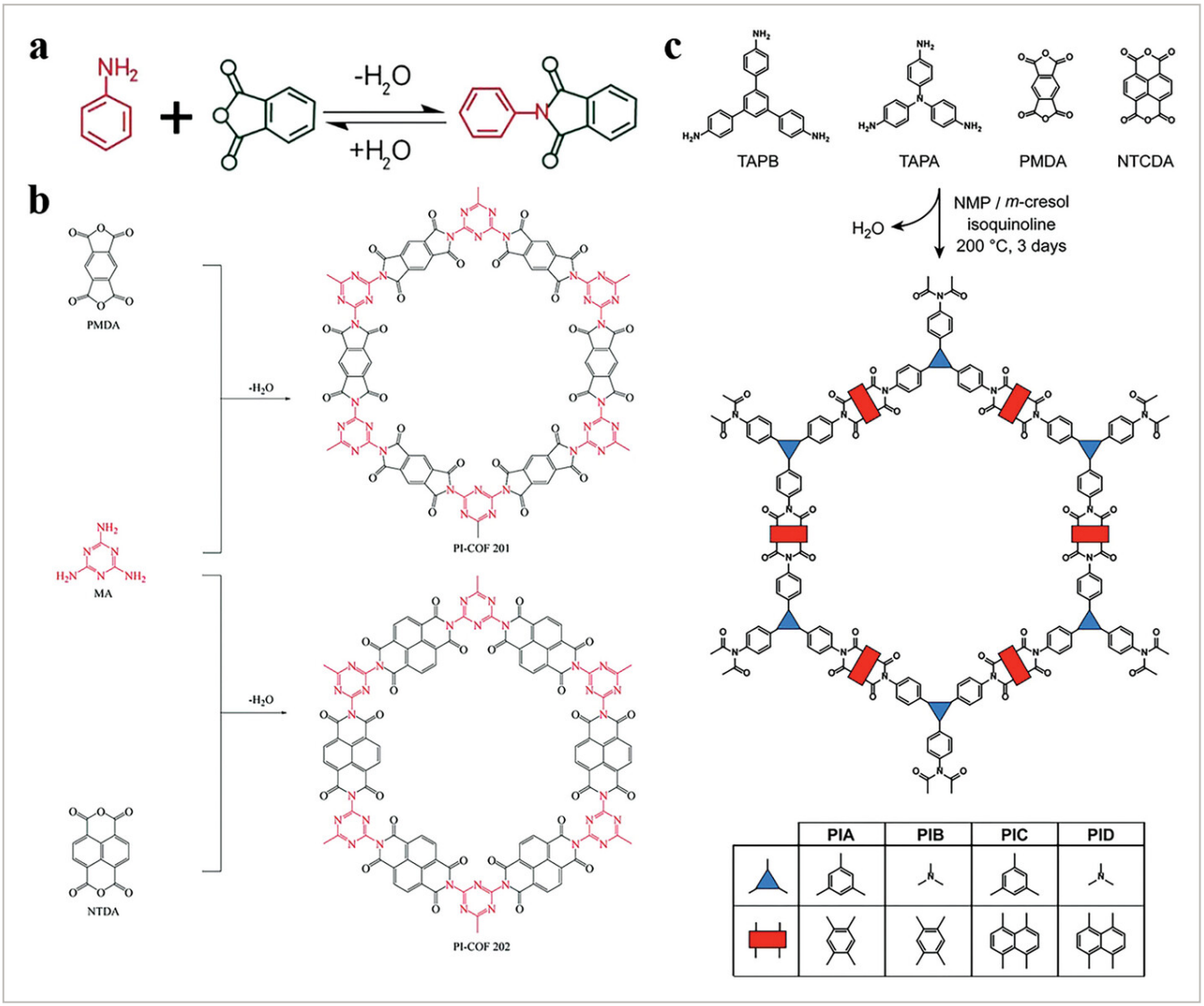

Figure 9

Open in figure viewer | PowerPoint

a) The imidization reaction. Reproduced with permission.[73] Copyright 2019, American Chemical Society. b) Synthesis of PI-COF 201 and PI-COF 202. Reproduced with permission.[74] Copyright 2017, Royal Society of Chemistry c) Synthesis scheme and the tags. Reproduced with permission.[75] Copyright 2021, American Chemical Society.

2.2.4 Irreversible Bond-Type COFs

The irreversible nucleophilic aromatic substitution reaction can produce many irreversible bond types, such as dioxin bonds and phenazine bonds. Dioxin bonds are planar and can weaken in-plane conjugation, leading to anisotropic charge transport through out-of-plane conduction channels. Jin et al. prepared a COF based on dioxin bond linkage by nucleophilic aromatic substitution.[76] DFT calculations showed that the weakening of the in-plane conjugation of the dioxin bond promotes the formation of anisotropic charge transport in the organic monomer, thereby generating a charge transport channel in the COF. Lei et al. prepared metal titanocyanine COFs (CoPc-dx-COFs) connected by dioxin bonds through nucleophilic aromatic substitution reaction. The irreversible dioxin bond is highly stable, which leads to the structural stability of CoPc-dx-COFs under various harsh conditions such as boiling water, concentrated acid (12 mol L^{-1} aq. HCl), concentrated alkali (12 mol L^{-1} aqueous NaOH), oxidation (30% H_2O_2) and reduction (1 mol L^{-1} $NaBH_4$). This allows CoPc-dx-COFs to be directly used as efficient electrocatalysts for ORR without the need for pyrolysis treatment as commonly used in previous studies.[77] The phenazine bond has nitrogen-rich characteristics and can provide a specific N content and N doping position. 2D-COFs with phenazine linkage not only have a highly planar rigid structure in the porous graphene-like monolayer but also can introduce uniform hexagonal pores and N atoms.[78] The β-ketoamine bond is formed by the tautomerism from enol to ketone. For example, the polycondensation reaction between 1,3,5-triformylphloroglucinol (Tp) and amines first forms a reversible imine bond and then forms a β-ketoamine-linked COF with excellent stability through irreversible enol-ketone tautomerization, which can maintain its porosity and crystallinity even under harsh chemical conditions.[79]

2.2.5 Other Types of COFs

Jin et al. condensed tetra (4-formylphenyl) pyrene with 1,4-benzenediacetonitrile to form a C ═ C-linked sp^2 c-COF, which is fully π conjugated and extends along the 2D direction.[80] Steven et al. first synthesized imine-linked COFs, and then modified them to obtain cyclic carbamates and thiocarbamate-linked COFs.[81] Zhao et al. prepared COFs connected by ester bonds through an ester exchange reaction.[82] Zhou et al. reported a synthetic strategy for the synthesis of azo bond COF.[83] Qian et al. reported the first COF connected with thiourea, in which thiourea is not only used as a connecting bond but also adsorbs Hg (II).[84] Yang et al. constructed a 2D COF with aromatic amine bonds.[85] Dong et al. prepared COFs connected with α-amino nitrile and quinoline under solvothermal conditions.[86] Liu et al. prepared imidazole-linked COFs through the Groebke-Blackburn-Bienayme (GBB) reaction.[87] At present, the bond type of COFs has been widely studied. Different reactions, monomers, and spatial configurations will produce different functional COFs.

The connection type determines the stability and synthesis conditions of COFs. To obtain crystalline COFs, dynamic covalent chemistry (DCC) is used to make their chemical bonds form, break, and reorganize under certain conditions, finally forming reversible covalent bonds. The B-O bond constructed by borate ester and boroxane has good thermal stability and high specific surface area. COFs containing C ═ N bonds such as imine bonds,

hydrazone bonds, and acridine bonds show better hydrolysis stability. Compared with Schiff-base COFs, COFs connected by imide, amide, and β-ketoamine bonds have better thermal stability and chemical stability due to the saturated C—N bond. With the further research of COFs in recent years, researchers have successfully expanded COFs with irreversible bond types through irreversible nucleophilic aromatic substitution reactions, greatly promoting the development of COFs. COFs connected by C = C have a more complete π-conjugated system, which is conducive to charge separation and transfer. Due to the irreversibility of sp^2 carbon bond formation, vinyl-linked COFs have extremely high chemical stability. In addition, 1,4-dioxin, phenazine, pyrazine and other irreversible bonds connected COFs also have excellent stability due to the irreversibility of formation. The connection types of COFs have constantly been explored (**Figure** 10). By designing the connection type and regulating the synthesis method, the diverse framework structures of COFs will provide unlimited possibilities for electrocatalytic applications.

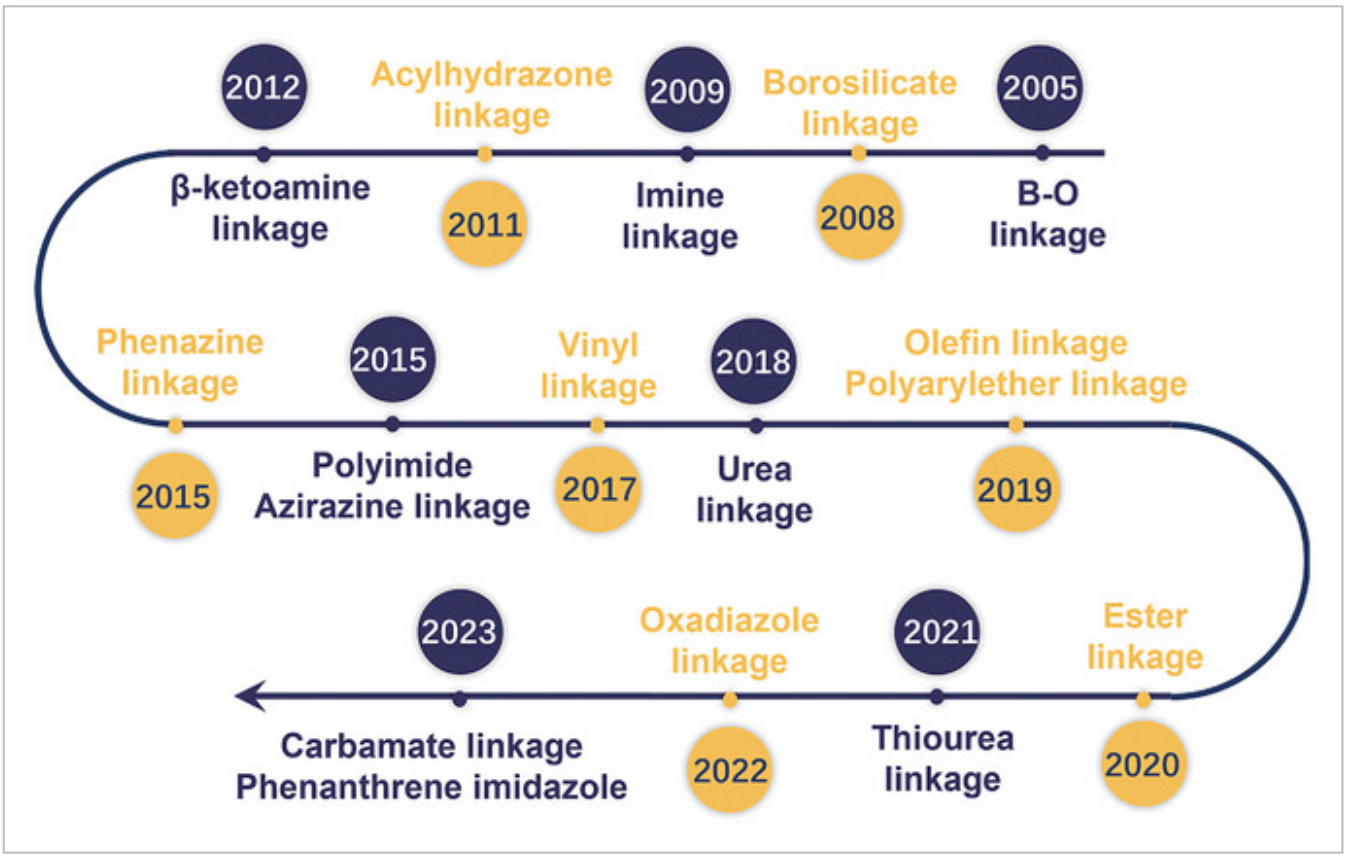

Figure 10

Open in figure viewer | PowerPoint

The formation process of linkages in COFs.

3 Synthesis Methods

During the formation of covalent bonds, adjusting thermodynamic equilibrium is the key to forming a highly ordered covalent network. Especially for polycondensation reactions,

reversible reactions can generate thermodynamically stable polymers. At present, the common synthesis methods of COFs include solvothermal synthesis, ionic liquid synthesis, interface synthesis, microwave-assisted synthesis, and mechanical grinding method (**Figure 11**). Covalent bonds are formed by adjusting appropriate temperature, solvent, and thermodynamic equilibrium.

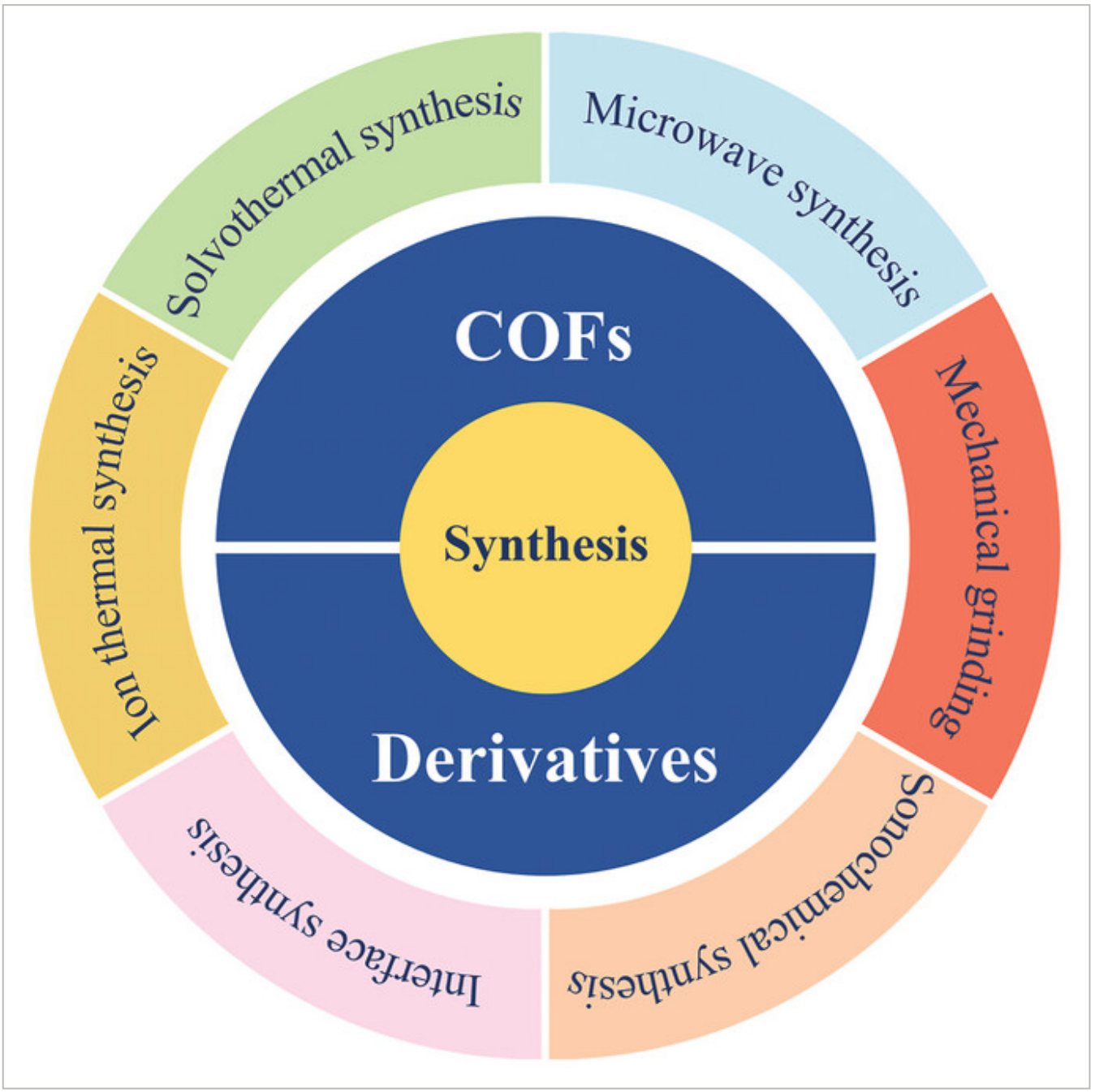

Figure 11

Open in figure viewer | PowerPoint

Synthesis of COFs and their derivatives.

3.1 Solvothermal Synthesis

Solvothermal method is the most classical method for the synthesis of COFs. The monomer and mixed solvent were placed in a Pyrex tube. After several freezing-extraction-argon-thawing cycles, the tube was sealed and heated at a specified temperature for a while. The precipitate was collected by centrifugation, and the unreacted monomer and oligomer were removed by washing with appropriate organic solvents. Then the powdered COFs were obtained by vacuum drying. In general, the combination and proportion of solvents are important factors affecting skeleton formation and crystallization. At the same time, the reaction temperature is also a necessary condition to ensure the reversibility of the reaction. Generally, the synthesis temperature of COFs is ≈85—120 °C. Peng et al. used supercritical CO_2 as a solvent to rapidly synthesize single-crystal 3D COF (**Figure 12a**).[88] Supercritical CO_2 accelerated the construction of a 3D network and realized the formation of single crystals within 1–5 min, which is 2–5 orders of magnitude faster than the traditional solvothermal method. Compared with traditional organic media, supercritical CO_2 promotes the penetration and diffusion of molecules and promotes the collision between reactants.

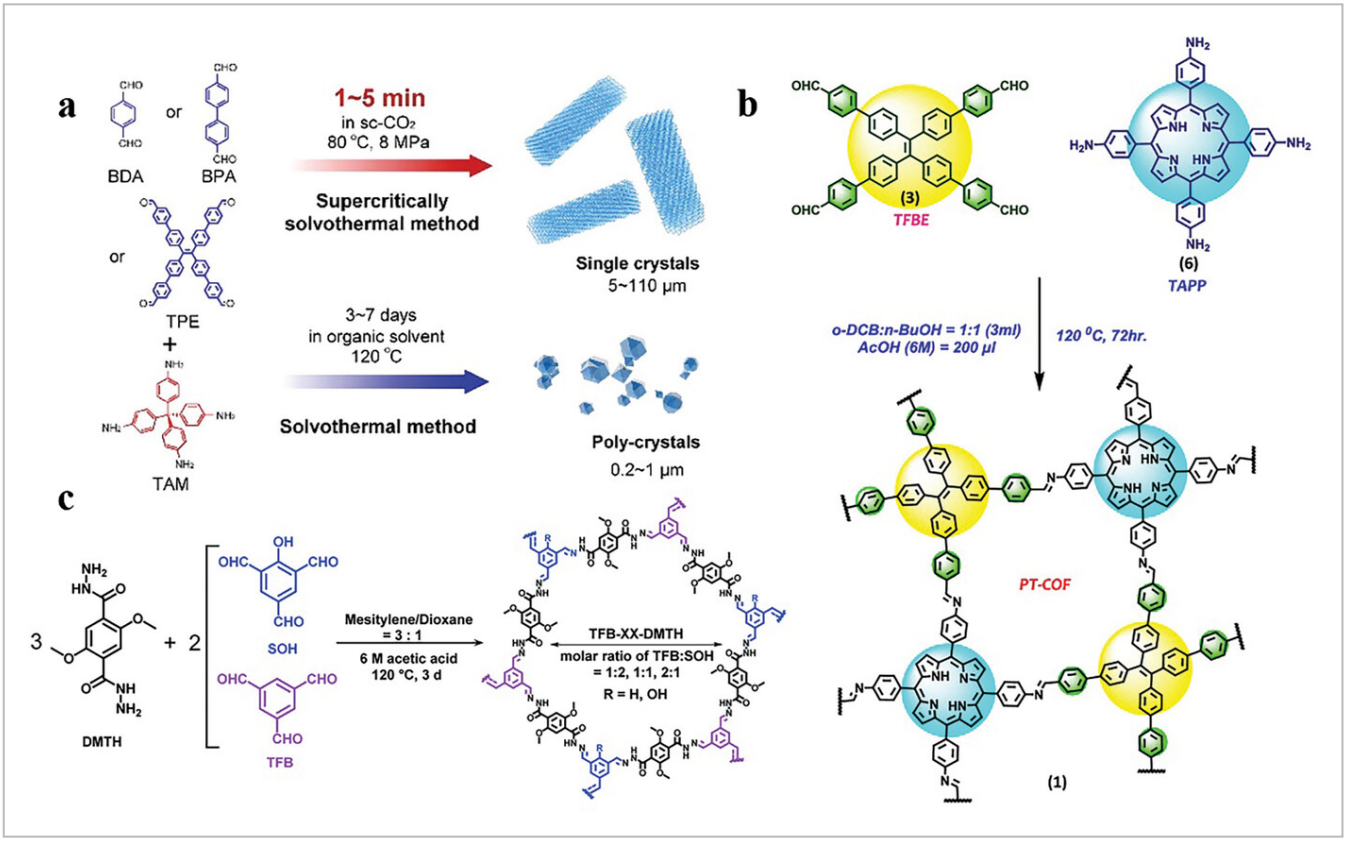

Figure 12

Open in figure viewer | PowerPoint

a) Synthesis of 3D COF. Reproduced with permission.[88] Copyright 2022, American Chemical Society. b) Synthesis of PT-COF. Reproduced with permission.[89] Copyright 2021, American Chemical Society. c) Synthesis of TFB-XX-DMTH. Reproduced with permission.[90] Copyright 2022, Royal Society of Chemistry.

Boric acid condensation, Schiff base reaction, and cyclotrimerization are the main synthesis methods for synthesizing crystalline 2D-COFs. The reaction conditions are highly dependent on the solubility and reactivity of compound ligands and the reversibility of the reaction. Bhattacharya et al. synthesized porphyrin-based 2D PT-COF through Schiff base condensation reaction at 120 °C (Figure 12b).[89] Liu et al. condensed 2,5-dimethoxy terephthalic hydrazine (DMTH), 1,3,5-triformylbenzene (TFB), and 2-hydroxy-1,3,5-benzaldehyde (SOH) to form hydrophilic 2D TFB-XX-DMTH (XX: TFB/SOH molar ratio) at 120 °C (Figure 12c).[90]

3.2 Ion Thermal Synthesis Method

Ionic liquid (IL) is a molten organic salt with low melting point, which is environmentally friendly, nonvolatile, and nonflammable. The physical and chemical properties can be adjusted. Guan et al. successfully synthesized 3D-IL-COFs with interpenetrating **dia** structure using 1-butyl-3-methylimidazolium bis ((trifluoromethyl) sulfonyl) imine ([BMIm] [NTf_2]) as the solvent at room temperature and atmospheric pressure for the first time.[91] Compared with solvothermal synthesis, ionic liquid synthesis is faster, and high-crystalline 3D-IL-COFs can be obtained in only 3 min. More importantly, ionic liquids can be screened out by simple filtration and reused at least three times. Gao et al. successfully synthesized a series of imine-linked COF films by using IL-H_2O as the interface (**Figure** 13a).[92] The specific surface area of the COF membrane prepared by this method was 4.3 times that of the dichloromethane-H_2O interface synthesis. The more carbon atoms in the alkyl chain of IL, the smaller the interface size, the greater the viscosity of IL, and the higher the crystallinity of the membrane. However, the reaction conditions of ionothermal synthesis are harsh, and the higher reaction temperature requires higher thermal stability of the building unit.

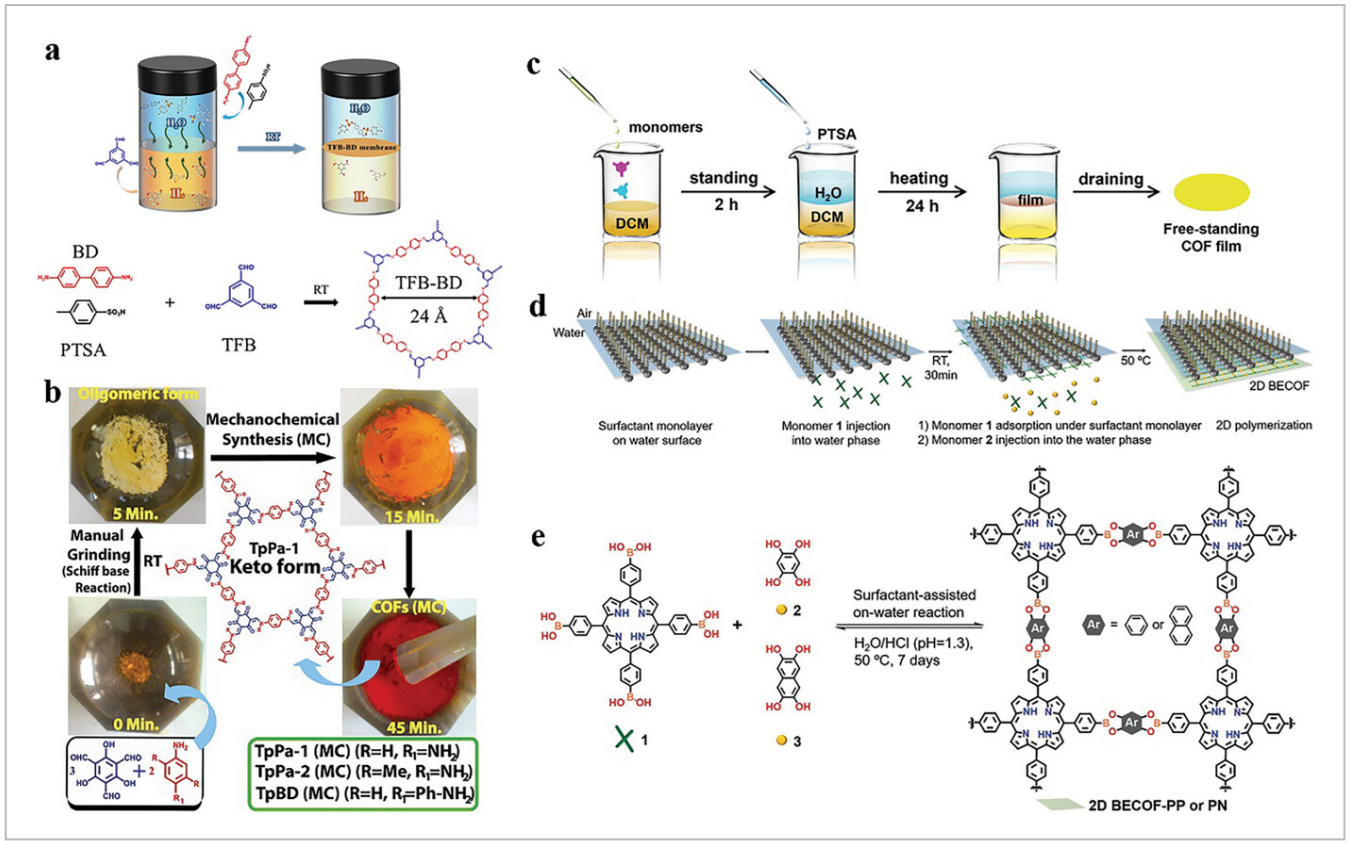

Figure 13

Open in figure viewer | PowerPoint

a) Ionic liquid synthesis method for the synthesis of TFB-BD. Reproduced with permission.[92] Copyright 2021, American Chemical Society. b) Mechanical grinding synthesis method. Reproduced with permission.[95] Copyright 2013, American Chemical Society. c) Liquid-liquid interface synthesis. Reproduced with permission.[99] Copyright 2021, American Chemical Society. d) SMAIS method. e) Synthesis of BECOF-PP or PN. Reproduced with permission.[68] Copyright 2020, Wiley-VCH.

3.3 Microwave Synthesis Method

The solvothermal synthesis method usually takes a long time. To improve the synthesis speed, researchers developed a microwave-assisted synthesis method to rapidly synthesize porous COFs. For the microwave method, the reaction system was placed in a microwave reactor, and COFs were synthesized by dynamic covalent reactions. This method not only improves the synthesis speed but also can remove impurities in the pores, improving specific surface area. In addition, compared with solvothermal synthesis, this method does not require closed containers, and the operation is simpler, which can realize the large-scale production of COFs. Microwave solvent extraction combined with extraction can effectively remove oligomers in COF so that it has better porosity. Ji et al. used microwave-assisted synthesis to prepare high crystallinity TH-COF connected by irreversible bond dioxins.[93] TH-COF had a specific surface area of 1254 $m^2 g^{-1}$, which is much higher than that of COF prepared under solvothermal conditions. In addition, TH-COF can be obtained at 70 °C in

30 min. Compared with the several hours required for solvothermal reaction, the microwave-assisted method significantly improves the synthesis speed. Zhao et al. prepared COF-Co with π–π stacking effect and rich defects by microwave irradiation, which improved conductivity and large reversible capacity of PIBs.[94]

3.4 Mechanical Grinding Method

In mechanical grinding method, two monomers are placed in an agate bowl with a pestle grinding initiation reaction. In 2013, Banerjee et al. first synthesized TpPa-1, TpPa-2 and TpBD (Tp = 1,3,5-triformylresorcinol, Pa-1 = p-phenylenediamine, Pa-2 = 2,5-dimethyl-p-phenylenediamine, BD = benzidine) by solvent-free mechanical grinding method.[95] The synthesis process is shown in Figure 13b. Compared with COFs synthesized by the solvothermal method, COFs synthesized by this method have layered structures like graphene, but the porosity and crystallinity are relatively poor. To solve this problem, in 2014, Banerjee et al. successfully synthesized hydrazone-linked TpTh by liquid-assisted grinding. COFs with higher purity and higher yield can be obtained by liquid-assisted mechanical grinding.[96] Lv et al. studied the morphological changes of COFs obtained under different auxiliary conditions by ball milling.[97] They found that the crystallinity and morphology of the product were extremely low in the absence of solvent or less solvent. When the solvent volume increases, no matter what solvent, the obtained product morphology is similar if the solvent volume is the same. In addition, compared with solvothermal method, the preparation time of ball milling mechanical grinding method is shortened by 36 times and the amount of solvent is reduced by eight times. Grinding synthesis method has low reversibility, which cannot form, destroy and modify chemical bonds like solvothermal method. The crystallinity and specific surface area of the obtained material are low, and its practicability remains to be further explored.

3.5 Interface Synthesis Method

Interface synthesis is a new method to prepare COF films with controllable thickness. Interface synthesis mainly includes solid-liquid interface synthesis, liquid-liquid interface synthesis, and liquid-gas interface synthesis. The solid–liquid interface is suitable for preparing COF films under solvothermal conditions. The COFs synthesized by condensation of aldehydes and amines have a hexagonal lattice structure. Shi et al. introduced salt into the reaction system to produce a liquid–solid interface and successfully prepared 2D COFs connected with imines.[98] During the reaction, COFs grow only on the salt surface, and their size and thickness can be adjusted by salt concentration. The generated COF nanosheets can be obtained by simple water washing. Compared with solvothermal method, COF nanosheets synthesized by salt-solution interface have a higher yield of up to 85%. Liquid-liquid interface is a common method to prepare COF films, which can be used to prepare large-area COFs. Huang et al. synthesized defect-free COF films using liquid–liquid interface (Figure 13c),[99] in which dichloromethane is used as organic phase, pure water is used as the water phase, and p-toluenesulfonic acid is used as catalyst. The synthesis of liquid–liquid

interface has the advantages of fine sealing and self-termination. Hence, the synthesized COF film has high mechanical strength, softness, and integrity even under vacuum drying conditions. In addition, the thickness of the prepared film can be controlled at the nano or even atomic level. Feng et al. prepared 2D BECOF films by the surfactant-single-layer assisted interfacial synthesis (SMAIS) method (Figure 13d,e).[68] They evaporated chloroform to form a SOS monolayer and water phase to form a liquid-gas interface, at which porphyrin macrocycles were combined with phenyl (PP) or naphthalene (PN) to prepare 2D BECOF-PP and 2D BECOF-PN. There are borate ester bonds in BECOF-PP, and the film can be transferred to different substrates, which have high mechanical properties. The thickness of BECOF-PP was 11 nm, the crystal size could reach 60 μm^2, and the average size of a single crystal would increase with the increase of reaction time.

3.6 Other Synthesis Methods

The sonochemical synthesis method makes bubbles grow and rupture in liquid by ultrasound and then produces acoustic cavitation, which can accelerate the reaction. This method is simple and cheap. Duan et al. prepared 2D COF-5 by a simple sonochemical method.[100] The boron-based ring group was formed in COF-5 with a BET area of 964.9 $m^2 g^{-1}$ and a pore size of 27.683 Å. The high porosity structure promoted the gas permeability and improved the selectivity of CO_2/N_2. Compared with COFs synthesized by traditional solvents, COFs synthesized by the sonochemical synthesis method have higher crystallinity and larger porosity.[101] In the sonochemical synthesis method, water was very important for the formation of imine-linked COF, which could be formed in high concentrations of AcOH.

Continuous flow synthesis is a modern synthesis method that can achieve accurate control of the reaction process. Continuous flow synthesis is a modern synthesis method that can achieve accurate control of the reaction process. In addition, the yield and efficiency are very high, which can achieve large-scale production of COFs. The continuous flow method has three advantages: 1) It can provide controllable catalyst diffusion layer thickness. The higher the flow rate, the smaller the thickness of the diffusion layer and the height of the material growth is limited. 2) It can provide stable reactant concentrations. Continuous refresh of the input stream can keep the reactant concentration stable. 3) It creates an easy separation environment for the manufacture of 3D SBFdiyne-COF. In addition, the reported synthesis methods include photocatalytic method, twin screw extrusion method, microfluidic method, steam-assisted synthesis method, in situ top-down growth method, and melt polymerization synthesis method.

At present, most COFs are synthesized by solvothermal method, and the crystallinity of the final reaction product depends on the solubility of the reaction ligand in the solvent, the reactivity, and the reversibility of the reaction. COFs prepared by ionothermal synthesis have the characteristics of high crystallinity and high specific surface area, but the reaction conditions are very harsh. The mechanical grinding method has low reversibility and cannot form, destroy, and transform chemical bonds like the solvothermal method. The microwave

synthesis method does not require a closed container, and the operation is simple and easy to implement, which can be used for rapid synthesis under solvothermal conditions. Although with the development of COF materials for more than ten years, the synthesis technology has gradually matured, it is still challenging to accurately control the synthesis speed, particle size, and crystallinity. Therefore, the synthesis processes and mechanisms of COFs need to be further studied in detail.

4 Electrocatalytic Applications

4.1 Oxygen Evolution Reaction

OER is a major obstacle to water electrolysis, requiring high-performance catalysts to accelerate the process. At present, IrO_2 and RuO_2 are the benchmark electrocatalysts with high catalytic activity.[17] However, the high cost and small reserves of precious metals limit their large-scale applications. COF has strong mechanical strength, low density, large specific surface area, rich active sites, and excellent stability, which has the potential to replace noble metal electrocatalysts for the OER.

4.1.1 Non-Metallic COFs

Electrocatalysts need to have good conductivity so that the electrodes can work at high current densities. Compared with metal-functionalized COFs, non-metallic COFs lack metal active sites and have low free electron transport efficiency, hence, there are few studies in the field of electrocatalytic OER. The C/N atoms in metal-free COFs are generally considered to be the main active sites. 2D COFs with phenazine bonds have good chemical stability and nitrogen-rich properties, mainly because the 2D monolayer has a highly planar rigid structure and uniform hexagonal holes and N atoms can be introduced. Yang et al. designed a new phenazine bond COF (COF-C_4N) (**Figure** 14a,b) with four fused phenazine-linked rings to replace the double bonds in graphene, and predicted its OER catalytic activity by DFT calculations.[78] From Figure 14c, when COF-C_4N absorbs energy, the holes are mainly concentrated on the C atom, which is transferred from the C atom to the N atom. The electrons are mainly concentrated on the N atom, which transfers from N atom to C atom. At U = 1.579 V (Figure 14d), the OER path shows a reasonable downward trend, which indicates that the edge C4 site is a potential active site. Bhaumik et al. prepared an imino-linked thiadiazole-based COF (C4-SHz COF) by Schiff base condensation of 1,3,5-tri (4-formylphenyl) benzene (C4-CHO) and 2,5-dihydrazide-1,3,4-thiadiazole (SHz) (Figure 14e).[32] The C4-SHz middle layers are self-assembled by weak π–π stacking and the whole framework shows low crystallinity. They constructed the theoretical optimization structure of C4-SHz monolayer and the most stable structure of OH* adsorption (Figure 14f,g), and calculated the free energy distribution of OER pathway at U = 0 and 1.23 V at C2 site, as shown in Figure 14h, displaying the rate-determining step of OER process with the most positive free energy value of OOH* adsorption. According to the free energy distribution at 1.48 V (Figure 14i), C2 as the active site of C4-SHz shows low OER overpotential. The 2D

layered structure can not only maintain a highly planar rigid structure but also expose more active sites and increase the contact area with the reactants. In addition, the doping of N atoms can regulate the energy band structure of graphene/graphene-like and promote electron transfer.

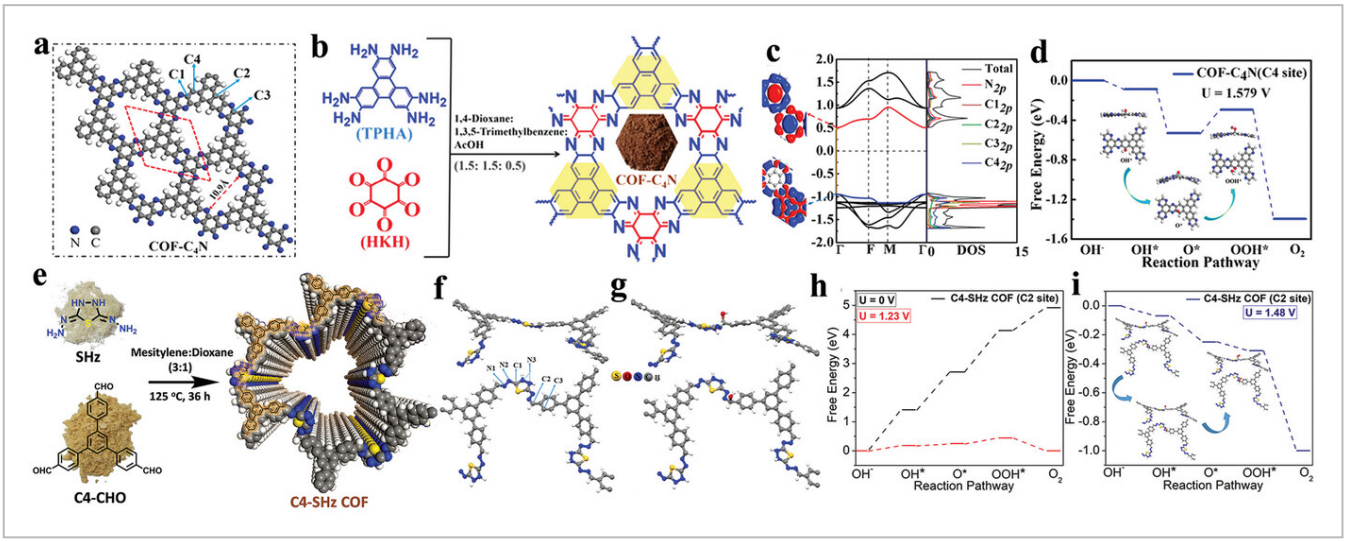

Figure 14

Open in figure viewer | PowerPoint

a) A 1 × 3 × 3 super cell of optimized COF-C4N. b) Synthesis of COF-C4N. c) Band structures, DOS, and wave functions of the conduction band minimum and valence band maximum for COF-C4N. d) Free energy profile at U = 1.579 V. Reproduced with permission.[78] Copyright 2019, American Chemical Society. e) Synthesis of C4-SHz. f) Theoretically optimized structure. g) Most stable structure of the OH* adsorbed. Free-energy profile at U = 0 and 1.23 V h) and U = 1.48 V i) for the C4-SHz. Reproduced with permission.[32] Copyright 2020, American Chemical Society.

4.1.2 Metal-based COFs

As a kind of low-cost catalyst, Co-based catalysts have good catalytic activity for the OER. Porphyrins can provide a strict and stable four-coordination environment ($M{-}N_4$), and Co porphyrins can provide redox active sites in the multi-electron transfer catalysis process. Gong et al. reported a 3D porphyrin-based COF based on stp topological network structure (named ZJUT-1 (ZJUT = Zhejiang University of Technology)) (**Figure** 15a) and then introduced cobalt ions through metallization to form ZJUT-1@Co (Figure 15b).[102] The efficient mass transfer in the ZJUT-1@Co skeleton and the fully accessible Co-based porphyrin active sites make its OER catalytic performance close to commercial RuO_2. DFT calculations showed that the introduction of Co enhances the charge density of the porphyrin center and regulates the interaction between the porphyrin-based COF and the *O intermediate (Figure 15c). In addition, the 3D COF based on the stp topology network structure can expose the active centers more thoroughly, thus greatly improving the catalytic performance.

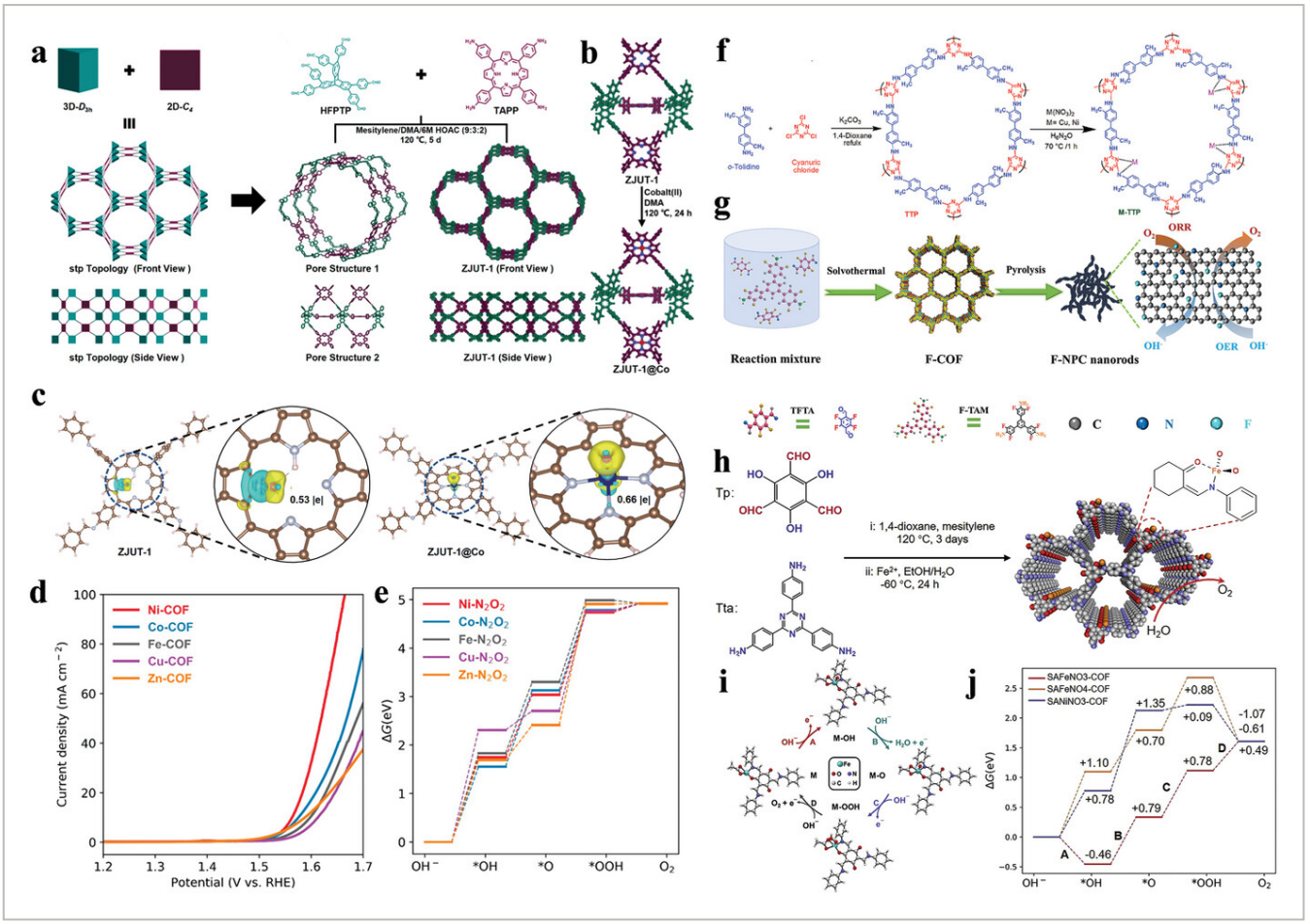

Figure 15

Open in figure viewer | PowerPoint

a) Synthesis of ZJUT-1 with **stp** topology structure. b) Synthesis of ZJUT-1@Co via post-modification. c) Charge density difference and Bader charge of the intermediate *O adsorbed on ZJUT-1 and ZJUT-1@Co. Reproduced with permission.[102] Copyright 2023, Royal Society of Chemistry. d) LSV curves of M-COF. e) Free energy profiles of the OER pathway. Reproduced with permission.[103] Copyright 2021, American Chemical Society. f) Synthesis of M-TTP. Reproduced with permission.[104] Copyright 2022, Elsevier Ltd. g) Synthesis of F—NPC—T. Reproduced with permission.[107] Copyright 2023, Elsevier Ltd. h) Synthesis of Fe-SAC@COF. i) The catalytic OER mechanism cycles of Fe-SAC@COF. j) OER volcano plot. Reproduced with permission.[109] Copyright 2022, Elsevier Ltd.

Ni element is abundant on the earth, and Ni-based compounds exhibit good oxygen evolution catalytic properties. Deng et al. used DFT to analyze the catalytic OER performance of COF coordinated by M—NxOy (M = 3d transition metal).[103] Subsequently, they prepared Ni-THPM by Schiff base condensation reaction, showing that the COF has high crystallinity and exhibits a 3-fold interpenetrating dia topology. The 3D interpenetrating channel helps to produce abundant accessible active sites and a high active specific surface area. Ni is in a positive charge state in Ni-THPM, in which Ni is coordinated with two N atoms and two O atoms. In 0.1 M KOH, Ni-THPM exhibited an overpotential of 335 mV at 10 mA·cm^{-2}, lower than Co-THPM (347 mV) and Fe-THPM (369 mV) (Figure 15d and **Table** 1). DFT calculations

showed that the free energy order of M-THPM prepared by M─N_xO_y (M = 3d transition metal) in the OER is Zn < Cu < Fe < Ni ≈ Co (Figure 15e). According to the experimental results, the OER activity of Ni-THPM is better than that of Co-THPM. Rajagopal et al. used Cu, Ni, and Cu─Ni alloys to modify o-tolylaminotriazine (TTP) for electrocatalytic OER (Figure 15f), [104] showing that Ni-TTP exhibited more prominent OER activity, which is mainly attributed to the presence of secondary amine bonds in the COF structure.

The Fe atom can adjust the electronic band gap of COF, and the free electrons in the d subshell of Fe can increase the electron density in the total density of states (DOS), resulting in changes in the crystal structure and electronic properties. Pakhira et al. prepared 3D COF (named COF-IITI-0) with P6m2 spatial group symmetry by using triborate, 2,4,6-triphenyl-1,3,5-triazine (TPT) and C_6H_4 ring.[105] Fe atoms were intercalated into the COF to form a sandwich structure, but the spatial group remained unchanged. After Fe atoms were embedded, the COF structure became more stable, and the Fe intercalation on the benzene ring of the TPT joint was more conducive to improving the binding energy. Muliken charge analysis showed that each Fe atom shares an electron with the connector to form a partial bond, and the electrons in the other d bands are completely free, and thereby the conductivity of COF after Fe atom intercalation was improved. Different transition metal atoms can be used to prepare new nanoporous COFs with different characteristics in the future.

The introduction of bimetallic elements into COFs can induce bimetallic electron interactions and further improve intrinsic activity. Zhou et al. designed 6 homonuclear and 15 heteronuclear 2D diatomic catalysts (DACs) and calculated the OER activity.[106] The calculated results showed that RhIr-COF has the best OER activity, and its initial overpotential is only 0.29 V, followed by CoNi-COF (0.33 V), RuRh (0.34 V) and NiIr-COF (0.37 V). The doped dual-metal atoms transfer a large amount of charge to the COF substrate, which means that the transition metal atoms have a high positive charge, which are the catalytic sites of OER.

Transition metal elements Ni, Fe, Co, and Mn have been widely doped into COFs, since they have large reserves, low cost, and are easy to combine organic units to form active metal sites. In addition, the factors affecting the OER catalytic activity include the topological structure of COFs, organic unit ligands, and connection bonds. The 3D topologies stp and dia usually have a penetrating structure and can expose active sites to a greater extent. However, the 3D topology will occupy most of the space of the pores due to multiple penetrations, resulting in small pore sizes and low porosity. Therefore, how to control the penetration is the key to improving the catalytic performance of 3D COFs.

4.1.3 COF Derivatives

The introduction of heteroatoms onto the carbon skeleton can change the charge distribution and spin density of adjacent carbon atoms, which is of great help to enhance

the catalytic activity of metal-free carbon materials. The doping of F can produce charge polarization on the carbon skeleton, resulting in the formation of edge-rich defects and significantly improving the OER reactivity. Ideal building units and heteroatom active sites can be generated in COFs by pre-designing, and therefore heteroatom-doped COFs can be used as precursors for the preparation of heteroatom-doped porous carbon materials. Li et al. prepared F, N co-doped porous carbon catalyst (F—NPC) by pyrolysis of F, N co-doped COF (Figure 15g).[107] Electron paramagnetic resonance (EPR) showed that F doping causes more unpaired electrons in the F—NPC, confirming the existence of edge defects. DFT calculations showed that the spin density of the F—NPC site exhibits a large change, indicating an increase in the diversity of reaction sites induced by F doping.

However, metal-free catalysts are limited for the OER due to the lack of active metal sites. Zhu et al. selected transition metals Fe and Co for the preparation of bimetallic porous carbon.[108] They chose triazine-based COFs (SNW-1) with abundant nitrogen atoms and abundant pores as the precursors to ensure that abundant functional groups and large specific surface area can be retained after pyrolysis. Bimetallic Fe/Co-based SNW-1 was pyrolyzed to form a nitrogen-rich porous FeCo@SNC, in which Fe, Co, N, and rich pore structures accelerate the transfer of electrons and protons. In addition, Co is considered to be the active center, and a small amount of Fe plays a regulatory role in the electronic structure of Co.

Single-atom catalysts (SACs) are considered to be one of the most promising OER catalysts due to their high atomic utilization and rich active species. The structure of COFs helps to immobilize single metal atoms through confinement effects and designated atom coordination. For example, metal titanocyanine COFs connected by dioxin bonds can construct M—N_4 mode. In addition, porphyrins can also provide a strict and stable M—N_4 coordination environment. Wang et al. restricted Fe-SAC to a π–π stacked COF with continuous layers to form Fe-SAC@COF (Figure 15h).[109] Fe exists in COF in the form of a single atom and coordinates with N/O to form a unique Fe—NO_3 coordination configuration. The highly efficient atomic utilization and unique metal coordination configuration make Fe-SAC@COF superior OER activity. DFT calculations confirmed that the coordination of Fe—NO_3 reduced the binding energy of oxygen-containing intermediates (Figure 15i,j), thereby improving the OER catalytic performance.

For COF derivatives, the porous properties of COFs and the diversity of organic unit ligands ensure that porous carbon with high conductivity and abundant heteroatoms can remain after pyrolysis. The addition of metal ions can not only increase active sites but also accelerate electron transfer and regulate electronic structure, which has a deeper impact on improving OER catalytic performance. In addition, the customizable structure of COFs can constrain single metal atoms, improving the utilization of metals. The coordination modes of M—N_4 and M—N_2O_2 formed by the coordination of single metal atoms with N/O in COFs can regulate the electronic structure of central metal atoms, thereby improving the catalytic activity.

In summary, non-metallic COFs lack active metal sites, and their catalytic performance is usually worse than that of metal COFs. However, the organic ligands containing conjugated structures make them maintain good stability and excellent electron transport efficiency. For example, the nitrogen-rich properties of s-triazine and phenazine bond help to provide non-metallic active sites. In addition, the creation of edge C or N sites is a method to enhance the catalytic activity of non-metallic COFs. The application of metal-based COFs in the OER is more extensive, such as metal porphyrins and metal titanocyanines. Among them, transition metals Co, Ni, Fe, and Mn can be used as independent active metal sites, and the free electrons in the d subshell can provide higher electron density. The interaction between two transition metals can optimize the electronic structure and improve the intrinsic activity of OER. Pyrolysis of COF precursors is a common method to prepare the derivatives, and thus the selection of suitable precursors is very important. COFs containing metal titanocyanine will generate M—N sites after pyrolysis, which helps to reduce the OER barrier. In addition, metal nanoparticles can be anchored on metal-free COFs to improve OER activity, such as triazine and imidazolium-rich COFs.

Table 1. Comparison of OER performance on COFs

Electrocatalyst	Substrate	Mass loading [mg cm^{-2}]	Electrolyte	η_{10} [mV]	Stability [h]	Reference
BEAB-Co	GCE [1]	/	1.0 M KOH	320	10	[110]
macro-TpBpy-Co	GCE	0.25	0.1 M KOH	380	10	[111]
TpBpy-Co	GCE	0.25	0.1 M KOH	430	/	[111]
CoNP-PTCOF	GCE	0.61	0.1 M KOH	450	20	[112]
CoNP-s-IMCOF	GCE	0.61	0.1 M KOH	500	10	[113]
Co@COF-Pyr	GCE	/	1.0 M KOH	450	/	[114]
CoS_2@BP-COP	NF [2]	0.6	1.0 M KOH	270	24	[115]
CoTPP	CFP [3]	0.29	1.0 M KOH	310	/	[116]

1 GCE: glassy carbon electrode;

2 NF: Ni foam;

3 CFP: carbon fiber paper;

4 CP: carbon paper;

5 CC: carbon fiber cloth;

6 CFC: carbon fiber cloth.

4.2 Hydrogen Evolution Reaction

At present, Pt-based catalysts are the best HER electrocatalysts. However, Pt is a precious metal, possessing small reserves and high cost, which is not conducive to large-scale use. COFs have porous structures and large specific surface areas, which are conducive to the mass transfer and the accommodation of active molecules. Their unique electronic properties and stability are also conducive to HER electrocatalysis.

4.2.1 Non-Metallic COFs

Triazine is a nitrogen-containing aromatic heterocycle with a conjugated structure, which has good thermal stability, chemical corrosion resistance, and strong electronic affinity. The abundant N atoms in the covalent triazine skeleton can produce defect sites and active centers. Voort et al. selected BINOL-CN (2,2′-dihydroxy-[1,1′-binaphthyl]−6,6′-dimethylnitrile) as the construction unit to prepare BINOL-CTF-x-y (x = 5eq./10eq. $ZnCl_2$, y = temperature) by thermal method (**Figure 16a**), which has a rigid extended π conjugate unit and isolated N-rich and O-rich sites.[127] Large specific surface area and uniform distribution of N active sites are conducive to improving the catalytic activity. Figure 16b shows that ─C═N exists at 1598 cm^{-1}, meaning that the nitrile group is converted to a triazine ring. In 0.5 M H_2SO_4, BINOL-CTF-10-500 had a low onset potential of 66 mV and η_{10} of 311 mV. Sarkar et al. calculated Bipy-linked CTF (Bpy-CTF),[128] and revealed the optimized geometric structure of 2 × 2 × 1 superlattice (Figure 16c). Figure 16d shows that Bpy-CTF is a direct band gap semiconductor with a band gap of 1.93 eV. To improve the electrochemical activity and reduce the band gap, Si and P atoms were co-doped into Bpy-CTF, and F atoms were used to replace the bipyridine hydrogen at the P site to synthesize SiPF-Bpy-CTF. The optimized geometric structure of 2×2×1 superlattice is shown in Figure 16e. The electronic band structure of SiPF-Bpy-CTF is shown in Figure 16f. The band gap of SiPF-Bpy-CTF is ≈ 7 meV. This low band gap promotes the electron transfer from the maximum valence band (VBM) to the minimum valence band (CBM), improves the conductivity, and promotes the charge transfer kinetics of HER. They calculated ΔG_{H*} under different H-coating ratios as shown in Figure 16g, and found that ΔG_{H*} is −0.06 eV at θ = 1/6, which is close to the ideal value. In addition, they plotted the volcanic curve of the average ΔG function of H atom adsorption. Figure 16h shows that SiPF-Bpy-CTF is almost at the peak, which is a promising HER catalyst.

Triazine skeleton has a large specific surface area, high stability, and N-rich characteristics, making CTFs have high catalytic HER activity.

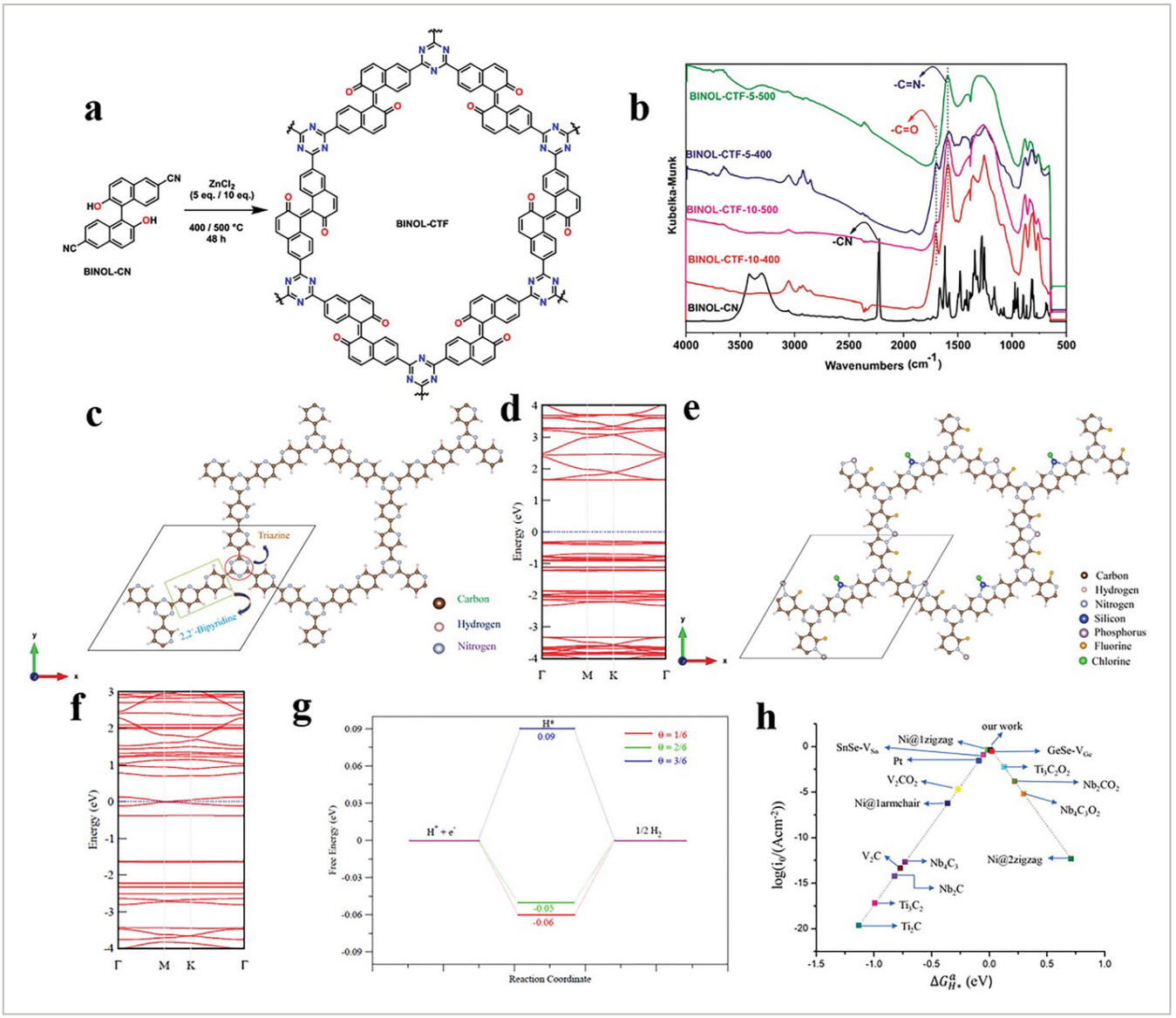

Figure 16

Open in figure viewer | PowerPoint

a) Synthesis of BINOL-CTF. b) DRIFT FT-IR spectra. Reproduced with permission.[127] Copyright 2020, American Chemical Society. Optimized geometric structure of the 2×2×1 supercell of c) Bpy-CTF and e) SiPF-Bpy-CTF. Band structure plot of d) Bpy-CTF and f) SiPF-Bpy-CTF. g) Free energy diagram of HER acting on SiPF-Bpy-CTF. h) Plot of a volcano curve. Reproduced with permission.[128] Copyright 2020, American Chemical Society.

The thiophene-based structure has high conductivity and fast charge transfer. The combination of thiophene and triazine unit can promote the electron transfer in HER and increase the electrocatalytic performance. Ma et al. prepared two thiophene-based metal-free COFs with 2,4,6-tri (4-aminophenyl)−1,3,5-triazine (TAPT) and thieno [3,2-b] thiophene-2,5-dicarboxaldehyde (TTDC) and 2,2′-dithiophene-5,5′-dicarboxaldehyde (bTDC), namely,

TTT-DTDA COF (JLNU-301) and TTT-BTDA COF (JLNU-302) (**Figure 17a**).[129] JLNU-301 is a spherical structure with a diameter of ≈ 1.5 µm and a specific surface area of 327 $m^2 \cdot g^{-1}$ (Figure 17b). The morphology of JLNU-302 is irregular flower-like crystallite with a specific surface area of 88 $m^2 \cdot g^{-1}$ (Figure 17c). The η_{10} on JLNU-301 and JLNU-302 was 136 and 91 mV in 1.0 M KOH (Figure 17d), 189 and 151 mV in 0.5 M H_2SO_4, and 282 and 320 mV in 1.0 M PBS, respectively. Figure 17e shows that compared with JLNU-301, JLNU-302 has a narrow band gap, which can inhibit electron-hole recombination and increase the electron transfer rate. Figure 17f shows that the ΔG on JLNU-301 and JLNU-302 was 0.15 and 0.11 eV, respectively. The lower energy barrier on JLNU-302 is mainly due to the enhancement of pentacyclic thiophene-S unit. High conductivity, high crystallinity, and permanent porosity make the material have a faster electron transfer rate in HER and promote catalytic activity.

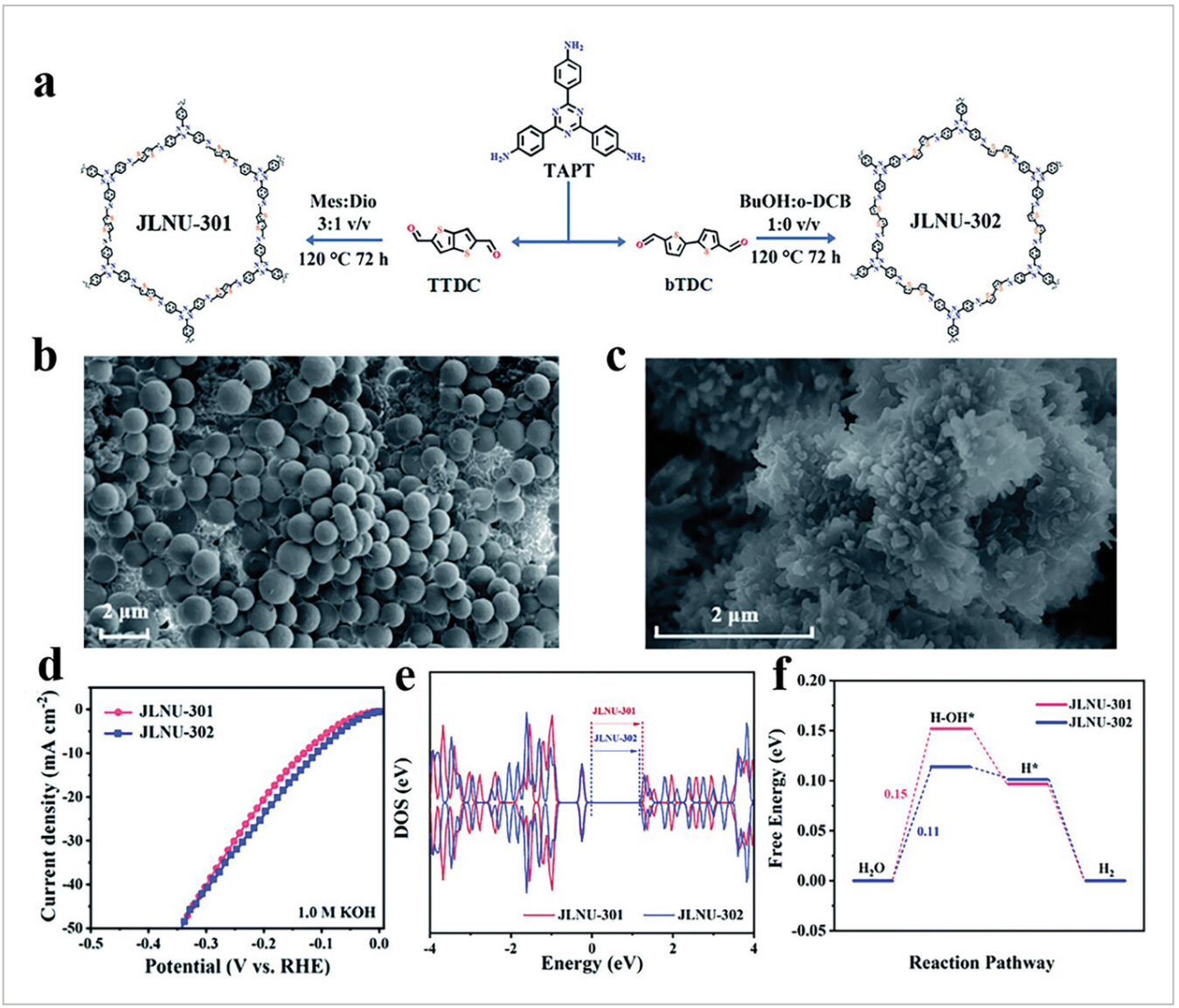

Figure 17

Open in figure viewer | PowerPoint

a) Synthesis of JLNU-301 and JLNU-302. SEM of b) JLNU-301 and c) JLNU-302. d) Polarization curves. e) DOS. f) Free energy diagrams. Reproduced with permission.[129] Copyright 2022, Royal Society of Chemistry.

4.2.2 Metal-Based COFs

Transition metals Ru, Co, Ni, Mo, and Rh have HER catalytic activity. The transition metal ions encapsulated in the pores of COFs can be used as heterogeneous catalysts to improve the catalytic HER activity and stability. Ru ions are combined with COF with sp^2 carbon, which is conducive to HER due to the high stability and high porosity of COF. Chen et al. prepared sp^2 carbon conjugated COF (COF-1) with triazine as the core by condensation reaction.[130] The sp^2 C═C bond is conducive to improving stability and enhancing the delocalized π bond. Triazine contains heterocyclic functional groups with multiple pyridine nitrogen atoms, which can coordinate with various metals and improve conductivity. Ru ions were loaded on COF-1 to prepare Ru@COF-1 (**Figure** 18a), whose crystal structure did not change. In 0.5 M H_2SO_4, COF-1 had almost no catalytic activity, but Ru@COF-1 had an η_{10} of 200 mV (**Table** 2) and had no decay of activity after 1000 CV cycles (Figure 18b,c). They assumed the HER process catalyzed by Ru@COF-1 as shown in Figure 18d. They designed three Ru coordination structures as shown in Figure 18e, where ΔG_{H^*} of Model-3 ($Ru{-}N_2Cl_2$) was ≈ 0.09 eV (Figure 18f). Ru has high electronegativity and strong binding ability with the H atom, and the strong interaction with N enhances conductivity and stability.

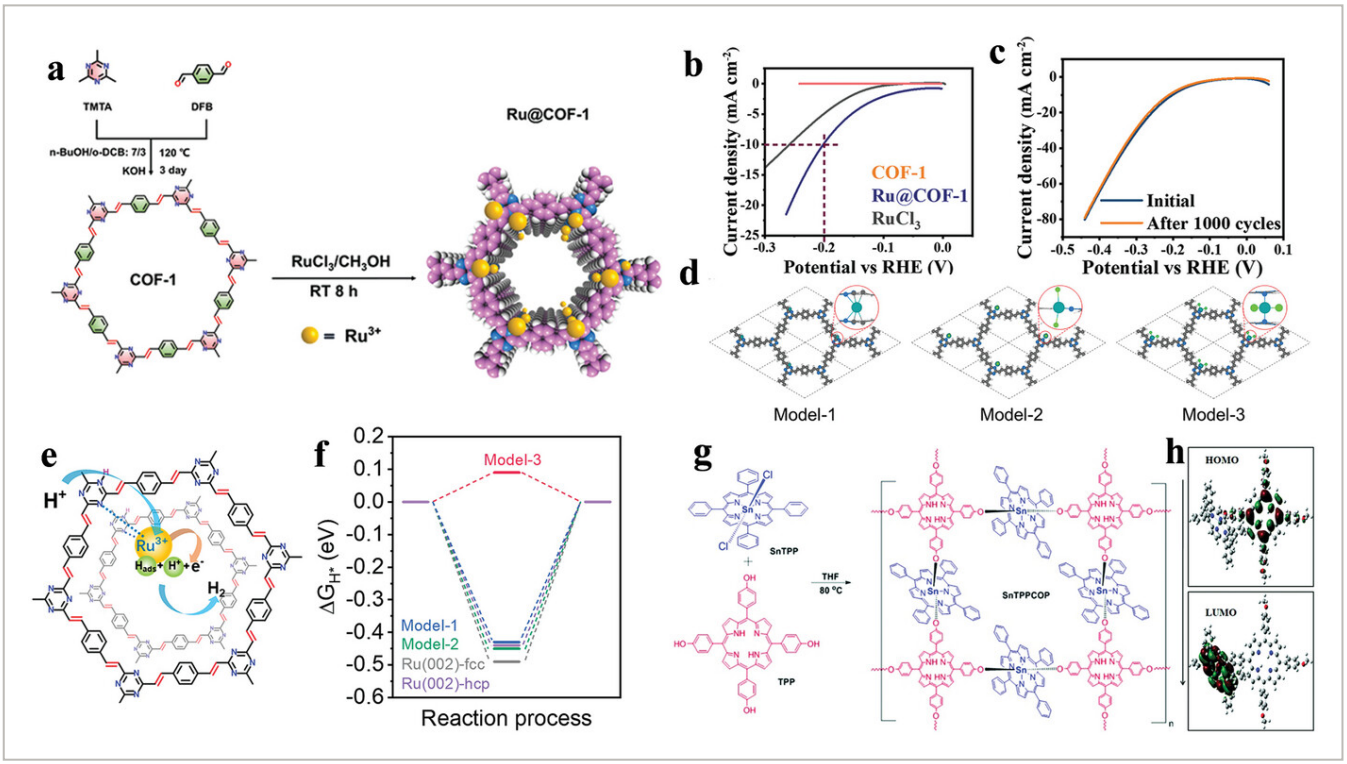

Figure 18

Open in figure viewer | PowerPoint

a) Synthesis of Ru@COF-1. b) LSV curves. c) LSV curves before and after 1000 CV cycles. d) Three Ru coordination structures. e) HER process on the Ru@COF-1. f) Calculated Gibbs free energy. Reproduced with permission.[130]

Copyright 2022, Wiley-VCH. g) Synthesis of SnTPPCOP. h) HOMO−LUMO plot of SnTPPCOP. Reproduced with permission.[131] Copyright 2022, Royal Society of Chemistry.

Table 2. Comparison of HER performance on COFs

Electrocatalyst	Substrate	Mass loading [mg·cm^{-2}]	Electrolyte	η_{onset} [mV]	η_{10} [mV]	Stability [h]	Reference
Ru@COF	GC	3.1	1.5 M H_2SO_4	159	212	/	[135]
Ru@COF-1	GCE	5	0.5 M H_2SO_4	/	200	/	[130]
Cu-TTP	GCE	/	0.5 M H_2SO_4	/	115	24	[136]
Cu—Ni -TTP	GCE	/	0.5 M H_2SO_4	/	225	24	[136]
C—Fe,Co—COF	GCE	0.6	0.5 M H_2SO_4	120	280	20	[123]
JLNU-301	GC	0.57	0.5 M H_2SO_4	/	136	20	[129]
JLNU-302	GC	0.57	0.5 M H_2SO_4	/	91	20	[129]
JLNU-301	GC	0.57	1.0 M KOH	/	189	20	[129]
JLNU-302	GC	0.57	1.0 M	/	151	20	[129]

7 RDE: Rotating disk electrode.

COPs with conjugated structure and large ring hollow channels have high HER activity, and 2D COPs with large specific surface area and fast electron transfer efficiency have small overpotential and excellent HER stability. Li et al. prepared 2D SnTPPCOP by nucleophilic substitution of 5,10,15,20-tetrakis (4-hydroxy-phenyl) porphyrin (TPP) and dichloro (5,10,15,20-tetraphenylporphyrinato) tin (IV) (SnTPP) (Figure 18g).[131] In SnTPPCOP, there is a strong π–π* interaction, and the characteristic band in the porphyrin monomer has a slight deviation. In 1.0 M KOH, SnTPPCOP exhibited an η_{10} of 147 mV, which is better than that of SnTPP (251 mV) and TPP (297 mV). DFT calculations showed that in SnTPPCOP, TPP located in HOMO is the donor, while SnTPP located in LUMO is the acceptor (Figure 18h). Electrons

are transferred from the donor TPP to the acceptor SnTPP, and holes are transferred from SnTPP to TPP, which can stably adsorb H atoms and promote the generation of H_2. Sn can promote the rapid transfer of electrons and promote the adsorption of H atoms. Large surface area, porous structure, and fast charge transfer make SnTPPCOP have excellent HER catalytic activity.

N, *N*'-bis (salicylidene) ethylenediamine (Salen) has a porphyrin-like coordination environment, which can stabilize metal ions to form macrocyclic compounds, enhancing the rigidity of the connector. Qiao et al. prepared Zn-Salen COF_{EDA} by the condensation of Salen with 1,3,5-tris (4′-hydroxy-5′-formylphenyl) benzene (THB) and obtained M-Salen COF_{EDA} (M = Cu, Ni, Co, Mn, and Fe) by ion exchange of Zn ions (**Figure 19a**).[132] Zn-Salen COF_{EDA} has an AA stacking structure (Figure 19b), and its lattice fringe is 2.1 nm. Zn-Salen COF_{EDA} has a porous structure with a specific surface area of 572 $m^2 \cdot g^{-1}$ (Figure 19c). According to XPS analysis, the binding energy of metal ions moved upward, and electrons transferred from metal to COF_{EDA}, stabilizing single metal ions and re-distributing the charge. In 0.5 M H_2SO_4, Co-Salen COF_{EDA} showed high HER activity with η_{10} of 320 mV (Figure 19d). After the introduction of PEDOT, the catalytic HER activity of PEDOT@Zn, Cu, Ni, Co, Fe, and Mn-Salen COF_{EDA} generally increased, and the η_{10} on Mn-Salen COF_{EDA} was 150 mV (Figure 19e). DFT calculations showed that more electrons were accumulated around the metal ions (Figure 19f), and the electrons around N_2—O_2 were consumed, illustrating that there was a strong charge interaction between metal ions and COF. Figure 19g shows that Co-Salen COF_{EDA} has a higher ΔG_{H^*}, and the d orbital of Co is more compatible with the s orbital of H. After the introduction of PEDOT, a heterogeneous structure with a highly active interface can be formed. The HER mechanism on PEDOT@Metal-Salen COF_{EDA} is shown in Figure 19h. Figure 19i shows that electrons accumulate at the interface between PEDOT and Mn-Salen COF_{EDA}. In addition, the electronic state of s in PEDOT overlaps with that of Mn, which indicates that there is a strong electron-interface interaction between PEDOT and Mn-Salen COF_{EDA}.

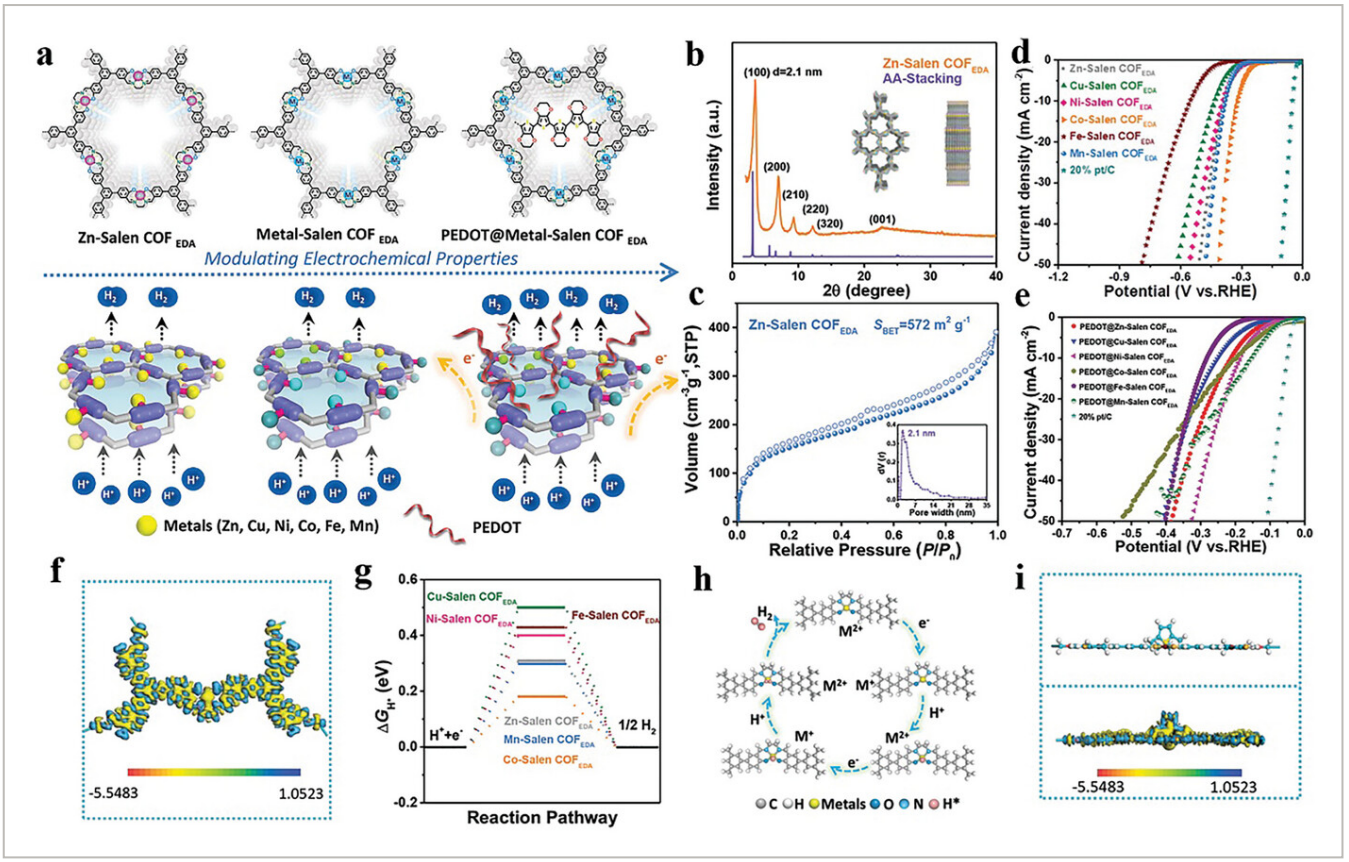

Figure 19

Open in figure viewer | PowerPoint

a) Schematic diagram of M-Salen COF_{EDA} and PEDOT@M-Salen COF_{EDA} electrocatalysts in HER. b) P-XRD pattern. c) N_2 adsorption/desorption isotherms. LSV of d) M-Salen COF_{EDA} and e) PEDOT@M-Salen COF_{EDA}. The calculated charge density difference of f) Co-Salen COF_{EDA} and i) PEDOT@Mn-Salen COF_{EDA}. g) Gibbs free energy for H_{ads} adsorption. h) Reaction mechanism. Reproduced with permission[132]. Copyright 2022, Wiley-VCH.

The diversity of building units provides a basis for the crystal structure and various applications of COFs. From aromatic hydrocarbons, nitrogen-containing heterocycles, and sulfur-containing heterocycles to macrocyclic compounds, COFs can not only inherit the inherent characteristics of these monomers but also develop their own structural characteristics to enhance various properties and functions. For example, triazine, as a nitrogen-containing aromatic heterocycle containing a conjugated structure, can provide abundant N atoms to generate defect sites. As a macrocyclic molecule containing a planar conjugated 18-π electron array, phthalocyanine has good physical and chemical stability. Porphyrins and porphyrin-like organic units can stabilize metal ions and enhance the rigidity of the connector.

4.2.3 COF Derivatives

Low conductivity is an important factor affecting COFs for electrocatalytic applications, which limits the full utilization of active sites. Combining COFs with graphene can improve

conductivity and effectively prevent graphene stacking. Zhao et al. first prepared COF/rGO composites by mixing COF with graphene oxide (rGO) through multi-step reflux, and then confined Ru ions in the composites to prepare COF/rGO-Ru.[133] According to XRD analysis, two peaks observed at 1342 and 1952 cm^{-1} indicated the presence of sp^3 defect sites and sp^2 in-plane stretching vibration, revealing that there are abundant defects in the catalyst. XPS analysis showed that there was an interaction between Ru, COF, and rGO, and electrons were transferred from N to Ru, resulting in electron delocalization, which is beneficial to enhancing HER catalytic performance. In an alkaline medium, the onset potential of COF/rGO-Ru was close to 0 mV, and the η_{10} was 42 mV, which was lower than that of Pt/C (52 mV). Both Ru atom binding COF/rGO and N atom binding carbon skeleton lead to the redistribution of electrons, increasing the carrier density and reducing the band gap of the catalyst. Ru and Ru—N in COF are the central active sites of HER, and the combination of rGO improves conductivity.

N doping can modify the electron-donating properties of carbon-based materials, in which pyridine-N or graphite-N can form the main catalytic sites. Sun et al. coordinated Ru to COF (C_4N) synthesized by polycondensation and annealed at 900 °C to form Ru@C_4N-900.[134] XPS showed that Ru^{3+} was reduced to Ru^0 after annealing. There were three configurations of C—NH_2, pyrazine-like C—N and graphite-N in Ru@C_4N-900, among which graphite-N was the main configuration. The electronic structure of Ru was modified after coordination with N, and the synergistic effect of highly dispersed Ru NPs in C_4N improved HER performance. The catalytic activity of N-doped C materials is influenced by the microstructure of the carbon matrix. Hollow nanostructures have open void space and low density, which can alleviate volume changes and promote charge transfer in electrocatalysis. The graphite-N and pyridine-N formed after N doping can be used as active sites. Owing to the advantages of large surface area, short diffusion path, and low density, electrocatalysts with hollow nanostructure obtained by N doping show potential application for the HER. In addition to N doping, B, F and P doping can also adjust the electronic structure of C. The co-doping of N and P with different electronegativity will produce more abundant active sites, making carbon-based electrocatalysts exhibit unique properties.

In summary, the triazine skeleton in non-metallic COFs has rich N sites and defect sites, which is conducive to the exposure of active sites and promotes HER kinetics. The combination of triazine unit with thiophene structure improves high conductivity, thus promoting the electron transfer in HER. The combination of transition metal ions with sp^2 carbon conjugated COF is one of the main methods to improve HER catalytic activity. In addition, triazine contains heterocyclic functional groups with multiple pyridine nitrogen atoms, which can coordinate with a variety of transition metals to form metal-based HER catalysts. Porphyrin has a highly conjugated π-electron structure, which can stably adsorb H atoms and promote the production of H_2. In the derivatives, N doping can form pyridine-N and graphite-N active sites, thus modifying the electron-donating properties of carbon-

based materials. In addition, the co-doping of N and P with different electronegativity will produce more abundant active sites and improve HER activity.

4.3 Oxygen Reduction Reaction

The ideal ORR catalyst should have an appropriate binding energy with the intermediate since the adsorption is a key step. If the adsorption is too weak, it will influence the transfer of electrons or protons to the adsorbed O_2, while if the adsorption is too strong, it will lead to difficult desorption of H_2O, thus limiting the subsequent adsorption of O_2.[148] COFs are considered to be one of the most promising ORR electrocatalysts due to their precisely controllable active sites, chemically adjustable pore structure, high stability, and fast charge transfer. In addition, a graphene-like structure can be formed by pyrolysis of COFs, onto which heteroatom B-, N-, and P-doping can improve the performance.

4.3.1 Non-Metallic COFs

O_2 tends to adsorb on the aromatic C═N in the triazine unit through a lateral mode, forming a quaternary ring as an ORR intermediate.[149] Tribani Boruah et al. prepared a triazine-based covalent organic polymerization (Trz-COP) using diformyl phloroglucinol (DFP) and TAPT (1,3,5-tri- (4-aminophenyl) triazine).[150] XPS showed that there were three different types of N-functional groups in Trz-COP, namely triazine-N, imine-N, and amine aldehyde-N. The presence of negatively charged triazine-N and imine-N in Trz-COP results in a partially positive charge (C*) on the C atom. According to the Pauling model, the adsorption of O_2 on C* causes the polarization of O═O bond, forming directionally preferred 5-membered and 6-membered ring intermediates (following the Yeager model). The push-pull interaction between C*, N, and O_2 promotes the dissociation of O═O and accelerates ORR (**Figure 20a**). Thereby, triazine and imine units act as dual active sites to promote ORR.

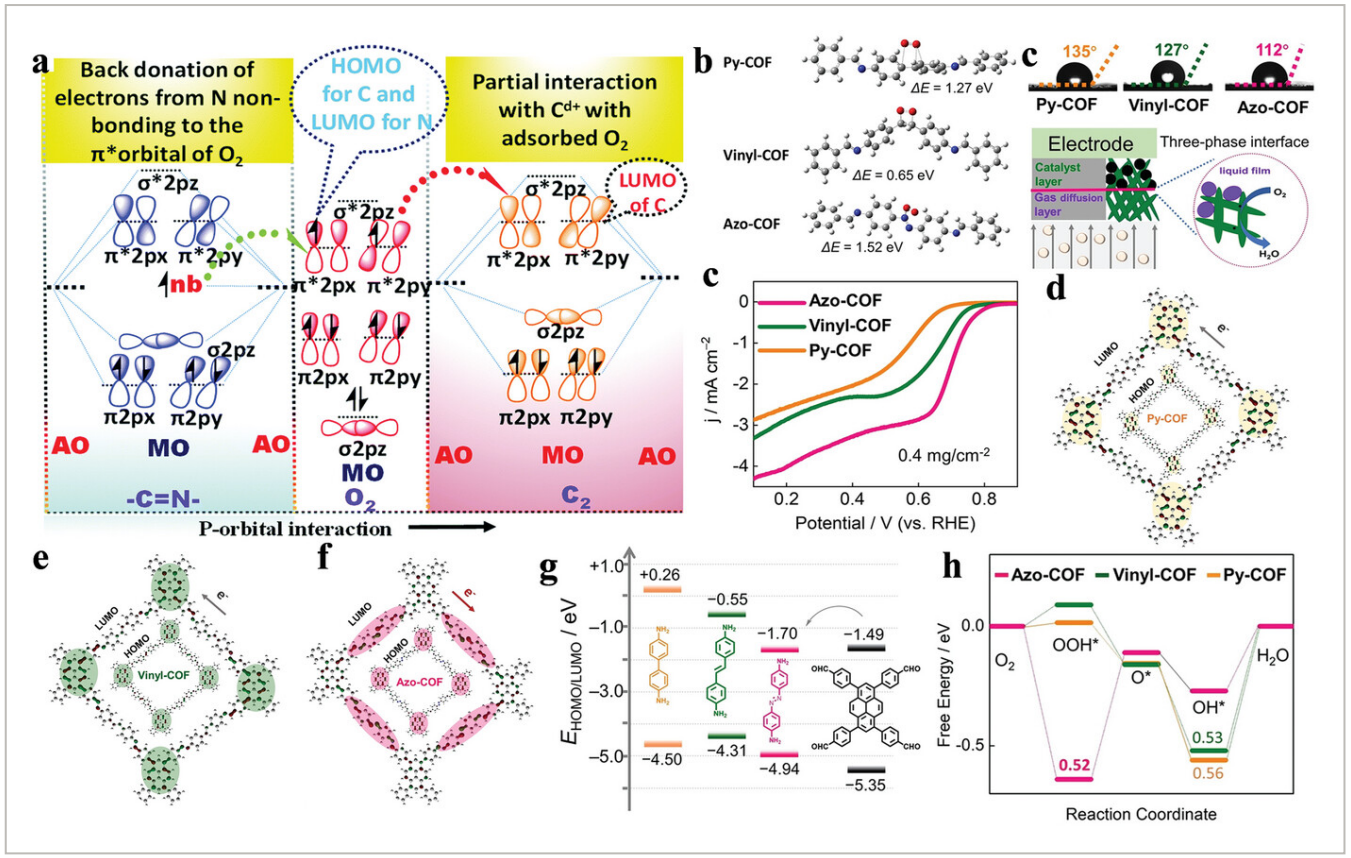

Figure 20

Open in figure viewer | PowerPoint

a) Schematic diagram of the molecular orbital interaction between C*, N, and O_2. Reproduced with permission.[150] Copyright 2022, Royal Society of Chemistry. b) Calculated oxygen binding energy. c) Contact angles and the three-phase interface of the ORR process. d) LSV curves. Kohn–Sham LUMOs and HOMOs of e) Py-COF, f) Vinyl-COF, and g) Azo-COF. k) LUMO/HOMO energy level alignments. h) Free energy diagrams at C═N (C) sites. Reproduced with permission.[152] Copyright 2022, Wiley-VCH.

The thiophene ring can significantly promote charge transfer and improve electrocatalytic efficiency. Bao et al. synthesized a 3D COF (BUCT-COF-11) with extended π-conjugated and thiophene structure by Schiff base polycondensation of 1,4-diaminobenzene (DAB) with a saddle-shaped ring octatetrathiophene derivative (COTHP-CHO) as a conjugated building block.[151] The conductivity of BUCT-COF-11 was 2.97×10^{-5} S·m^{-1}, which is ≈10 times higher than that of the control sample BUCT-COF-1 (1.94×10^{-6} S·m^{-1}). Similarly, the half-wave potential ($E_{1/2}$) of BUCT-COF-11/CNT (0.72 V vs RHE) was 40 mV higher than that of BUCT-COF-1/CNT (0.68 V vs RHE) in 0.1 M KOH (**Table 3**). DFT calculations showed that the introduction of thiophene into the COF not only reduced the band gap and improved the electron conduction efficiency, but also increased the adsorption capacity of the active sites and optimized the electronic structure, thereby improving the ORR performance.

Table 3. Comparison of ORR performances

Electrocatalyst	Substrate	Mass loading [mg·cm^{-2}]	Electrolyte	E_0 [V vs RHE]	$E_{1/2}$ [V vs RHE]	Reference
TRIPTA-COF	RDE	/	0.1 M KOH	0.77	0.68	[160]
BUCT-COF-11/CNT	RDE	/	0.1 M KOH	/	0.72	[151]
Pt@COF	RDE	0.6	0.1 M KOH	1.04	0.89	[161]
CoNP-PTCOF	RDE	/	0.1 M KOH	/	0.85	[112]
Co-TP-COF	RDE	/	0.1 M KOH	0.81	0.73	[153]
Mn-TP-COF	RDE	/	0.1 M KOH	0.75	0.68	[153]
Ni-TP-COF	RDE	/	0.1 M KOH	0.72	0.66	[153]
H-TP-COF	RDE	/	0.1 M KOH	0.71	0.65	[153]
CoTAPP-PATA-COF	GCE	0.2	0.1 M KOH	0.926	0.801	[162]
CoTAPP-BDTA-COF	GCE	0.2	0.1 M KOH	0.925	0.803	[162]
CoCOF-Py-0.05rGO	GC	/	0.1 M KOH	0.84	0.765	[163]
CoCOF	GC	/	0.1 M KOH	0.82	0.745	[163]
CoCOF-Py-0.1rGO	GC	/	0.1 M KOH	0.83	0.746	[163]
CoCOF-Py-0.25rGO	GC	/	0.1 M KOH	0.754	0.84	[163]
Ag/Ag$_2$O@MCOF(Co)	RDE	0.286	0.1 M KOH	0.87	0.76	[125]

Unsaturated bonds (UBs) can reduce the barriers of electron transfer, improve reactant affinity, increase cloud overlap, and enhance the ability to absorb electrons. In addition, it can optimize the electronic structure, adjust the catalytic reaction kinetics, and maintain the precise fixation of the molecular skeleton.[152] Yan et al. introduced UBs without changing the main chain and configuration to prepare vinyl-COF and azo-COF.[152] According to the calculation of oxygen binding energy (Figure 20b) and contact angle (Figure 20c), azo-COF had higher oxygen absorption capacity and smaller contact angle, which improved the activation of O_2 and promoted ORR performance. Azo-COF showed a half-wave potential of 0.68 V (vs RHE), better than pyridine-COF and vinyl COF (Figure 20d). Figure 20e,f shows that the HOMO and LUMO of pyridine-COF and vinyl-COF were located in the pyrene unit, while the HOMO of the azo-COF was located in the pyrene unit and the LUMO was located in the azobenzene unit. The minimum HOMO-LUMO gap was 2.28 eV, indicating that the azo-COF had typical donor-acceptor (D-A) characteristics, which were conducive to charge transfer (Figure 20g). As shown in Figure 20h, at the C═N (C) site, the free energy of the azo-COF and vinyl-COF was 0.52 and 0.53 eV, respectively, which was lower than that of the pyridine-COF

without unsaturated bond (0.56 eV), indicating that the unsaturated bond promotes the ORR.

4.3.2 Metal-Based COFs

COFs can be combined with transition metal ions to enhance the conductivity and increase active sites for the ORR. Metal-based porphyrin compounds have a conjugated π-electron macrocyclic structure, which can form a π-conjugated donor-acceptor in the plane with other building units. The structure-activity relationship can be observed at the atomic level by changing the metal atoms in transition metal-based porphyrin compounds. Yue et al. designed four porphyrin COFs (M-TP-COF, M = H_2, Co, Ni, and Mn) to study the relationship between the structure and ORR catalytic activity.[153] XPS showed that Co and Ni were divalent and Mn was trivalent in M-TP-COF. In 0.1 M KOH, the initial potential (E_0) and $E_{1/2}$ for Co-TP-COF were 0.81 and 0.73 V, respectively (Table 3). According to DFT calculations, Co-TP-COF had the lowest ORR energy barrier of 1.126 eV. The combination of diarylamine units with porphyrin COF can promote electron transport along the skeleton and increase the electrochemically active surface area since diarylamine is a typical electron donor.

Metal-based phthalocyanines are considered to be potential non-noble metal oxygen electrocatalysts due to their low cost and low overpotential in the four-electron ORR. The double-chain ladder structure has high thermal, chemical, and mechanical stability, which can improve the field effect mobility of electrons. Zhang et al. prepared a fully conjugated 2D Fe-phthalocyanine COF (FePc-BBL COF, BBL = benzimidazole phenanthroline) with a rigid double-chain trapezoidal structure by solvothermal condensation reaction.[154] In FePc-BBL COF, the atomic ratio between Fe and N elements is close to 1:4, and Fe—N_4 sites in the phthalocyanine iron-based material can be used as highly active sites. The trapezoidal fully aromatic conjugated skeleton and high active Fe—N_4 sites enhanced the conductivity, thermal/chemical stability, and corrosion resistance, improved the electron transfer rate and mass transfer efficiency, and increased the catalytic ORR activity.

For defects with different geometric shapes (such as pentagon, heptagon, octagon, and double vacancy doping), the pentagon defect introduced into graphite carbon is considered to be the ORR catalytic active center, for instance sulfur-containing pentagonal defects can promote charge transfer.[155] In addition, heteroatoms with different electronegativity redistribute the electrons and improve the ORR electrocatalytic efficiency, Hence, for designing COFs, the selection of nitrogen-containing and sulfur-containing monomers will help to improve the ORR electrocatalytic efficiency.

4.3.3 COF Derivatives

Single-atom M—N-C catalysts exhibit comparable ORR catalytic activity to Pt-based catalysts due to M—N_x active sites favoring the activation of adsorbed O_2. COFs with abundant nanopores and low diffusion/transport barriers are suitable precursors for the synthesis of M—N_x-C catalysts. The specific surface area, conductivity, and defect sites of M—N-C can be

adjusted by optimizing the pyrolysis temperature. Jiang et al. synthesized COF nanospheres using 1, 3, 5-triformylbenzene (TFB) and 1, 4-diaminobenzene (PDA) under solvothermal conditions and then pyrolyzed them with Fe^{3+} to form N-doped carbon nanospheres (Fe—N-CNS).[156] N-CNS had enhanced graphitization and appropriate defect pores obtained by optimizing the temperature, which synergized with the Fe—N active site to increase ORR activity. Fe—N-CNS had an $E_{1/2}$ and diffusion current close to 20% Pt/C. The pyrolysis temperature and pressure will affect the pore size and specific surface area of the synthesized material, and thus affect the ORR activity by changing the mass diffusion degree and the number of exposed active sites.

MOFs have large specific surface area, high porosity, and adjustable structure, showing high catalytic activity in the field of electrocatalysis.[157] The combination of COFs and MOFs can show higher catalytic activity than individual ones. The unique carbon support generated by pyrolysis of COF@MOF conjugates has a special core-shell morphology and abundant binding sites. Li et al. combined imidazole-functionalized COF-SM (SM = 2-mercaptoimidazole) with ZIF-67 to form COF-SM@ZIF-67, and then obtained H-NSC@Co/NSC by pyrolysis (**Figure 21a**).[158] H-NSC was a hollow N, S-doped carbon core derived from COF. The cavity has high permeability and low density, which is conducive to diffusion kinetics and active site exposure. Co/NSC was a carbon shell embedded with Co NPs derived from ZIF-67, which had a stable structure. In 0.1 M KOH, the E_0 of H-NSC@Co/NSC was 0.98 V (vs RHE), which is superior to ZIF-67-derived Co/NC (E_0 = 0.95 V vs RHE) and COF-derived NSC (E_0 = 0.87 V vs RHE) (Figure **21b**). As shown in Figure **21c–e**, the combination of Co and carbon matrix could promote electron transfer, adjust the electronic structure of the carbon matrix, produce a higher partial density state near the Fermi level, and optimize the adsorption of oxygen intermediates, thereby improving ORR activity. The hollow structure and abundant active sites led to high activity and high stability. Miao et al. limited Zn and FePc in ZIF-8 to obtain $COF@MOF_{800}$.[159] The centrally controlled structure not only provided high surface area and highly exposed active sites but also facilitated charge transfer and ion transport. Figure **21f** shows possible models for $COF@MOF_{800}$, FePc@O-C, and $COF@MOF_{800}$-Fe. Figure **21g,h** shows that the OOH * intermediate was the rate-determining step (RDS) of ORR on $COF@MOF_{800}$ and FePc@O-C, with overpotentials of 0.62 and 0.61 V, respectively. The RDS on Fe-site in $COF@MOF_{800}$-Fe was the formation of OOH* with the overpotential of 0.41 V, while the RDS on Zn-site in $COF@MOF_{800}$-Fe was the transformation of OOH* to O* with the overpotential of 0.54 V. The introduction of ZnN_4 site improved the activity of FeN_4O, and FeN_4O modulated the electronic state of ZnN_4. The synergistic effect reduced the RDS energy barrier and improved the ORR activity.

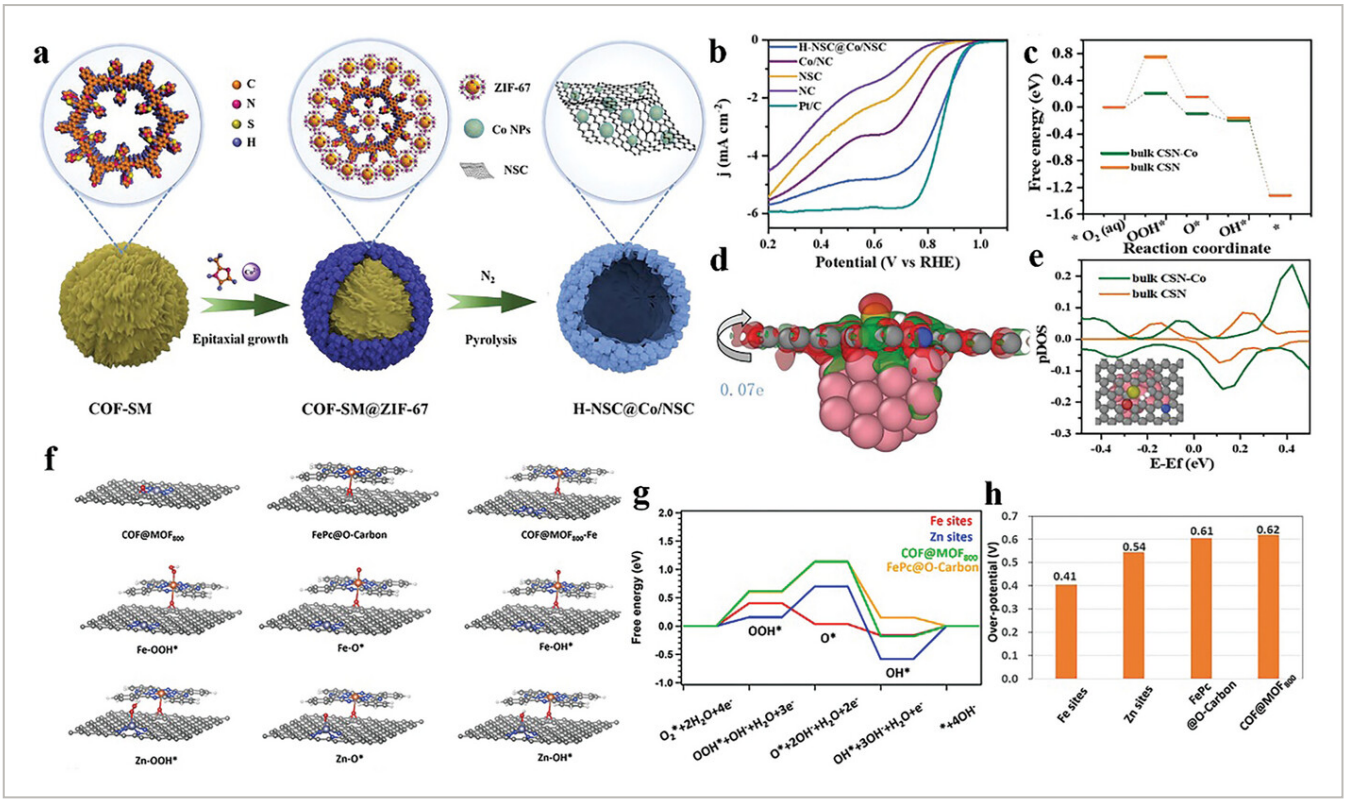

Figure 21

Open in figure viewer | PowerPoint

a) Synthesis of H-NSC@Co/NSC. b) LSV curves. c) The calculated free energy diagrams (FEDs). d) The charge difference. e) The calculated partial density of states (pDOS). Reproduced with permission.[158] Copyright 2022, Wiley-VCH. f) The model structure and proposed ORR mechanism on the Fe sites and Zn sites. g) Free energy diagram and h) the overpotentials. Reproduced with permission.[159] Copyright 2022, Wiley-VCH.

The precise framework structure in COFs can accommodate ordered catalytic active sites, and their high specific surface area and high porosity can increase mass transfer efficiency of the catalytic ORR process. Adsorption energy is the key to affect ORR kinetics. Compared with HER and OER, ORR can be more efficiently catalyzed by non-metal-based COFs, mainly because O_2 generally tends to adsorb on positively charged C atoms (C*). The interaction between C*, N, and O helps to promote the dissociation of O═O bond. The introduction of thiophene ring structure can improve the electron conduction efficiency, increase the adsorption capacity of active sites, and optimize the electronic structure. In addition, the introduction of unsaturated bonds will increase cloud overlap and improve strong electron-withdrawing ability. Common metal-based COFs for the ORR mainly include metal-based porphyrin compounds and metal-based titanium cyanine compounds. Metal-based titanium cyanine has a very low overpotential for the four-electron ORR. Among the COF derivatives, single-atom M─C─N catalysts prepared by pyrolysis can show comparable activity to the noble metal Pt in the activation of adsorbed O_2. By pyrolysis of MOF@COF conjugates, special core-shell dynamics and more binding sites are formed. In addition to converting

COFs into controllable metals and heteroatoms doped carbon materials by pyrolysis, the preparation of composite structures without pyrolysis is also an effective method for preparing ORR catalysts, which is not only simple in program and low in cost but more importantly, different functional units can be introduced to optimize the performance.

4.4 CO_2 Reduction Reaction

COFs have an excellent catalytic effect on CO_2RR mainly because the adjustable pore structure makes it possible to adsorb a large amount of CO_2, and the π–π stacking structure can promote charge transfer and greatly improve CO_2 reduction efficiency. In addition, the specific structural units in COFs can combine the advantages of efficient catalysis of molecular catalysts and the characteristics of high-stability framework structure, making them contain the characteristics of heterogeneous catalysts. In 2015, Yaghi et al. reported the use of COF after optimization for the CO_2RR.[174] They connected cobalt porphyrin molecules as building units into COF through imine bonds to form an π-conjugated system and a shorter interlayer distance, thus showing higher carrier mobility and conductivity. When the potential was −0.55 V (vs RHE), the Faraday efficiency (FE) of the product CO was as high as 90%, the conversion number was 290 000, and the initial TOF was 9400 h^{-1}. Since then, the use of COF materials as catalysts for the CO_2RR has received extensive research.

4.4.1 CO_2 Reduction to CO

In the CO_2RR, CO is the most common product in experiment, which requires only two-electron transfer. There are two paths for the conversion of CO_2 to CO. One is the coupled proton-electron transfer (CPET), which allows CO_2 to simultaneously obtain an electron and a proton to form *COOH. The *COOH intermediate is then converted to *CO by further proton-electron transfer. Finally, the CO product is generated by the dissociation of *CO bonded by the weak force.[175] The other is that the CO_2 molecule first accepts an electron to convert to $*CO_2^{\cdot-}$ radical, and then the $*CO_2^{\cdot-}$ radical is protonated to *COOH, which is further transformed into CO. In these transformations, electrocatalysts with appropriate catalytic activity are needed.

Metal phthalocyanine has an adjustable structure and strong chemical stability, which has outstanding performance in electrocatalytic CO_2RR. It is worth noting that the central metal has a great influence on the CO_2RR performance. For example, cobalt phthalocyanine can selectively reduce CO_2 to CO. Han et al. prepared 2D polyimide-linked phthalocyanine COFs (CoPc-PI-COF-1 and CoPc-PI-COF-2) by solvothermal reaction, which have a four-connected square lattice (**sql**) network structure and strong interlayer π–π interaction generated by AA stacking (**Figure 22a**).[176] At 25 °C and 1.2 bar, CoPc-PI-COF-1 and CoPc-PI-COF-2 had moderate CO_2 absorption values of 19.4 and 19.1 $cm^3 \cdot g^{-1}$, respectively. At −0.90 V (vs RHE), the mass activity of CoPc-PI-COF-1 was 573 $mA \cdot mg^{-1}$, which was superior to CoPc-PI-COF-2 (482 $mA \cdot mg^{-1}$) and CoPc (161 $mA \cdot mg^{-1}$). Figure **22b** shows that compared with CoPc (1.53 eV), the energy gaps of CoPc-PI-COF-1 (0.88 eV) and CoPc-PI-COF-2 (0.70 eV) were

smaller, which are more favorable for CO_2RR. Ignoring the long-range interaction between cobalt sites, a finite cluster model with A and B units was constructed. Figure 22c shows the Co coordination environments in CoPc, demonstrating that A and B units were similar. The Gibbs free energies of CoPc, A, and B were calculated as shown in Figure 22d. The Gibbs free energy of *CO showed that CoPc-PI-COF-1 was more favorable for CO desorption.

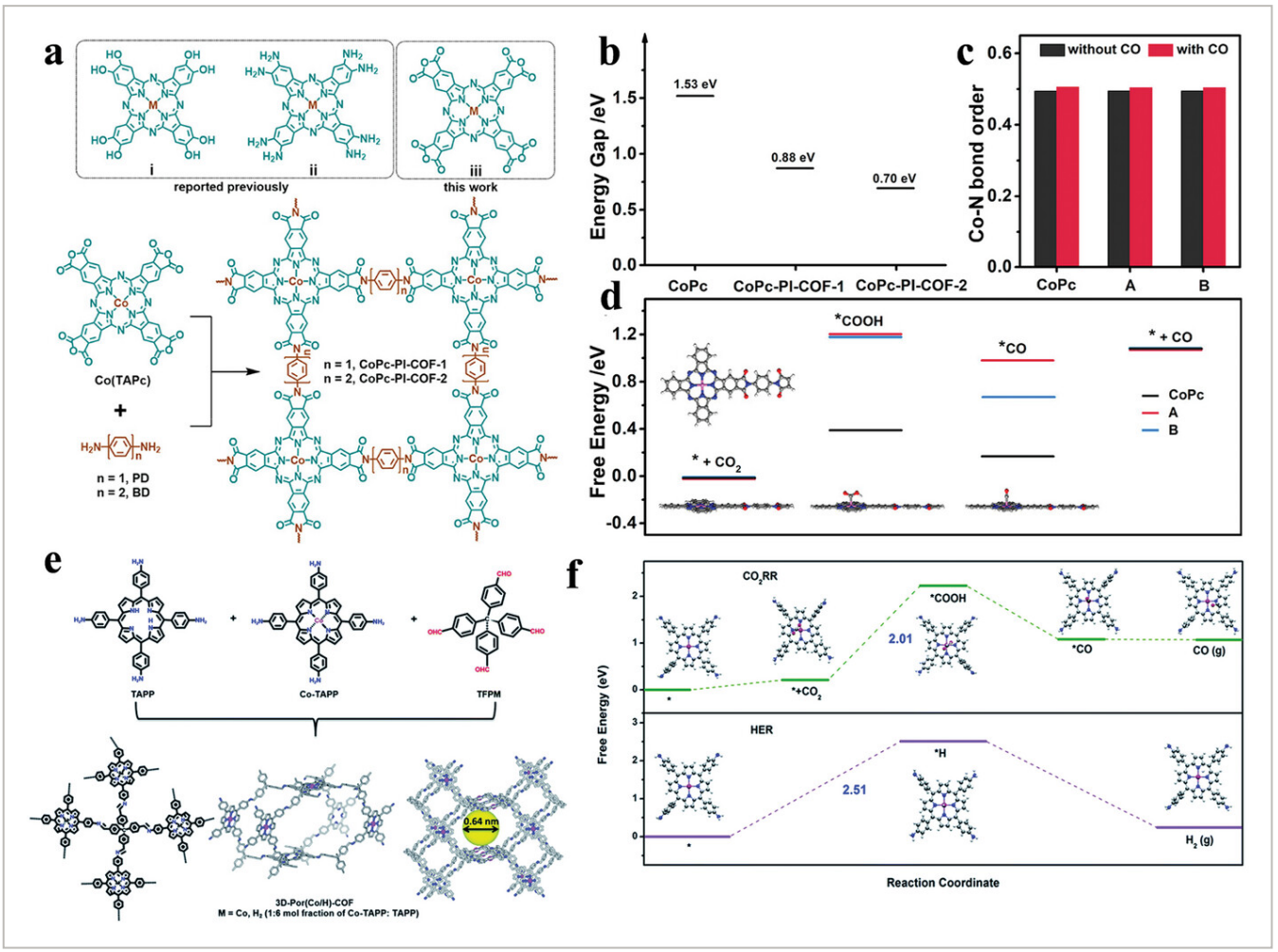

Figure 22

Open in figure viewer | PowerPoint

a) Synthesis of CoPc-PI-COF-1 and CoPc-PI-COF-2. b) Calculated energy gap. c) Co—N bond orders. d) Calculated free energy diagram. Reproduced with permission[176]. Copyright 2021, American Chemical Society. e) Synthesis of 3D-Por(Co/H)-COF. f) CO Faradaic efficiency. f) Calculated free energy diagrams. Reproduced with permission[177]. Copyright 2022, Royal Society of Chemistry.

Metal porphyrin complexes have a clear crystal structure and open metal active sites, which are conducive to adjusting electronic properties. Metalized porphyrin-based COFs have excellent stability, high electron transfer ability, and high CO selectivity. Huang et al. prepared porous 3D-Por(Co/H)-COF by Schiff base condensation reaction (Figure 22e).[177] Compared with 2D COFs, 3D COFs have spatially separated building blocks, which are more conducive to the complete exposure of active sites. According to DFT calculations

(Figure 22f), CO_2 adsorbed on the Co—N_4 site forms *COOH through proton-coupled electron transfer (PCET). The *COOH intermediate is then converted to *CO by PCET and finally desorbs from the Co site to form CO. The free energy of *COOH formation is lower than that of *H formation in the HER, which is not conducive to the occurrence of HER. Crown ethers (CEs) have ring cavities and electron-donating properties, and their combination with COF can improve hydrophilicity. In addition, combined with metal porphyrins, CEs can transfer electrons to the metal porphyrin core to enhance conductivity. Furthermore, triazines (CTFs) are rich in N atoms, which are conducive to coordinating with transition metal ions. Metal-functionalized CTFs have unsaturated coordination, which can significantly improve the FE in electrocatalytic CO_2RR. The clear metal center and high conductivity are beneficial to improve the conversion of CO_2 to CO, requiring a reasonable choice of metal–organic units or building units for the construction of COFs.

4.4.2 CO_2 Reduction to CH_4

The chemical reduction of CO_2 to CH_4 ($CO_2 + 4H_2 \rightarrow CH_4 + 2H_2O$) exhibits ΔH of −252.9 kJ mol^{-1} and Gibbs free energy (ΔG) of −130.8 kJ mol^{-1}. From the thermodynamic point of view, the reaction can proceed spontaneously, but the production of CH_4 involves an $8e^-$ reduction process and multiple proton transfer, which has poor kinetics and a slow reaction rate.[178] Hence, people have tried various ways to prepare new catalysts for the CO_2RR. COFs have large specific surface areas and accessible pore channels, which are conducive to the adsorption, diffusion, and activation of CO_2. Cu-based catalysts are currently recognized as efficient electrocatalysts for the production of hydrocarbons and oxygen-containing compounds. Cu aggregates, including single atoms (SA), nanoclusters (NCs), and nanoparticles, are confined in the rich channels of COFs to generate Cu-COFs to promote the reduction of CO_2 to CH_4. The abundant pores in COFs are conducive to the transfer and utilization of CO_2, and the large specific surface area increases the contact between CO_2 and intermediates. Wang et al. used 2, 4-diamino-6-cholyl-1, 3, 5-triazine as a functional exfoliating agent (Dct) to exfoliate Cu-Tph-COF-OH into ultrathin nanosheets (Cu−Tph-COF-Dct) (**Figure** 23a).[179] Dct was modified by a C—O covalent bond to modify COFs. TEM showed that Cu-Tph-COF-OH was cubic before modification (Figure 23b), while Cu−Tph-COF-Dct was a nanosheet structure with a large size of ≈ 1.0 µm and a thickness of 3.8 nm. The ultrathin sheet structure, uniformly dispersed Cu sites, and high porosity made Cu−Tph-COF-Dct have high catalytic activity in the CO_2RR. At −0.9 V, FE(CH_4) was ≈ 80%, and in the range of −0.8 to −1.0 V, FE(CH_4) remained above 68% (Figure 23c). DFT calculations showed that the Dct group could enhance the absorption and activation of CO_2, promote the formation of CO intermediates and further transfer to the Cu site, and promote the production of CH_4.

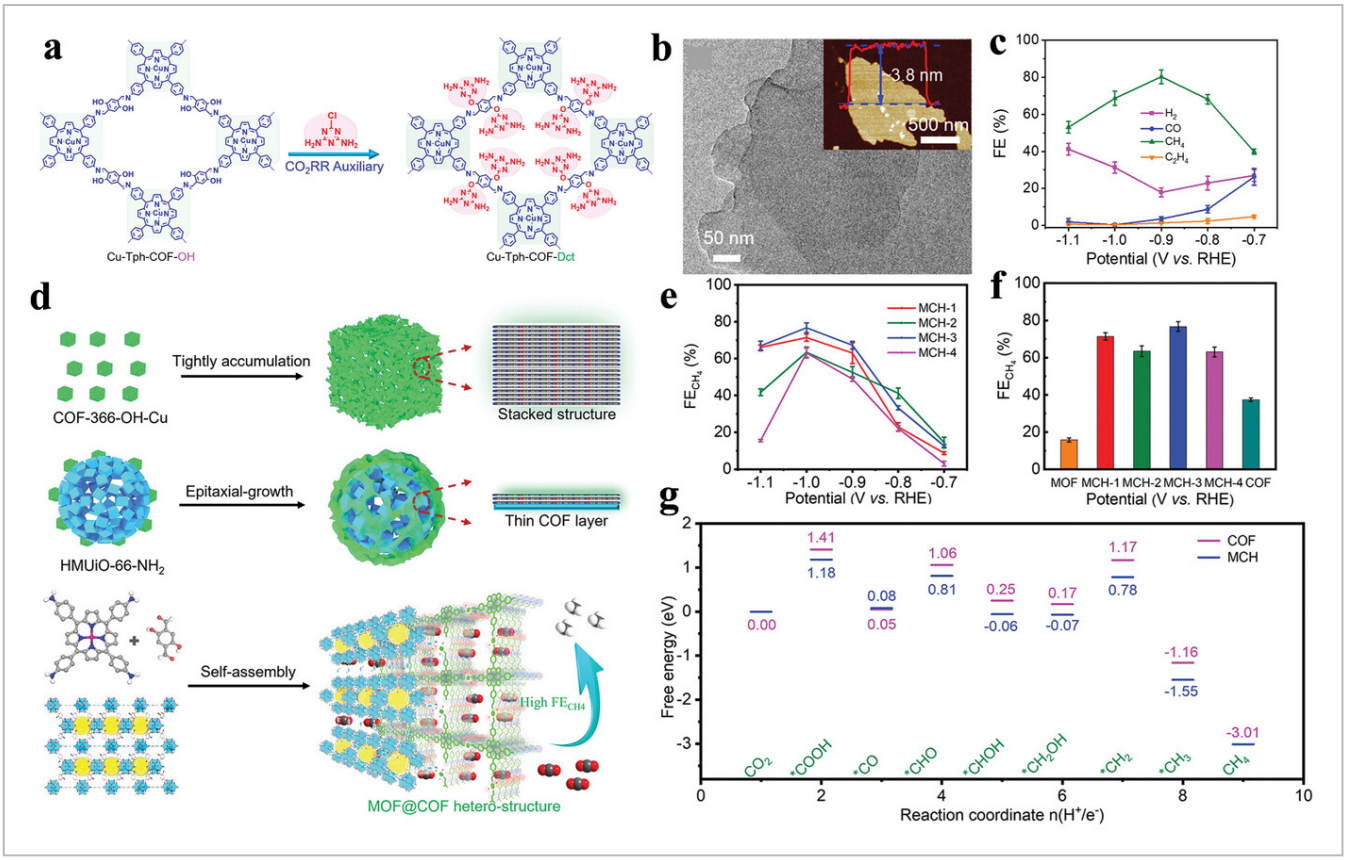

Figure 23

Open in figure viewer | PowerPoint

a) Synthesis of Cu-Tph-COF-Dct. b) TEM and AFM (insert) image of Cu−Tph−COF−Dct. c) FEs at different applied potentials. Reproduced with permission[179]. Copyright 2022, Wiley-VCH. d) Schematic illustration of MCH-X in electrocatalytic CO_2RR. e) FE(CH_4) of MCH-X. f) Comparison of FE(CH_4) at −1.0 V (versus RHE). g) Free energy profiles. Reproduced with permission[180]. Copyright 2022, Wiley-VCH.

COFs and MOFs have significant differences, and the combination is complementary. For example, in situ growth of COFs on the template of honeycomb MOFs with huge mesopores can form a unique heterostructure, which can greatly expose active sites for electrocatalysis. Yang et al. in situ grew Cu-porphyrin-based COFs containing Cu—N_4 sites on honeycomb MOFs to form MOF@COF honeycomb heterostructures (MCH-X, X-1-4, X represents different dose numbers of MOF) (Figure 23d).[180] MCH-X showed a honeycomb-like morphology, and MCH-3 showed a honeycomb-like heterostructure morphology with a diameter of ≈ 100 nm. At −1.0 V, the FE(CH_4) of MCH-3 was 76.7%, and the current density was −398.1 mA·cm^{-2}, which was superior to pure MOF (15.9%, −187.8 mA·cm^{-2}) and pure COF (37.5%, −374.4 mA·cm^{-2}) (Figure 23e,f). In the range of −0.9 to −1.1 V, FE(CH_4) can be maintained above 70%. DFT calculations showed that *COOH is the RDS of CO_2RR. At this time, the free energy on the MCH-3 is 1.18 eV, which is lower than that on COF (Figure 23g). This indicates that MOF can stabilize the intermediate and reduce the reaction energy barrier.

4.4.3 CO_2 Reduction to Methanol/Formic Acid

Formic acid is a commodity with industrial value, which is widely used in the pesticide, leather, dye, medicine, and rubber industries. Thermal stability is a stumbling block to the reduction of CO_2 to formic acid. To solve this problem, researchers found SACs with high stability and high catalytic activity. Qiao et al. first prepared 2D N-COF by reacting hexaaminotriphenylene hexahydrochloride (HATP) with hexaketocyclohexane octahydrate (HKH) and then used N-COF as the carrier to anchor Co atoms to form Co—N-COF.[181] DFT calculations showed that the band gap of Co—N-COF (0.67 eV) is reduced compared with N-COF (1.80 eV), proving that Co^{2+} promotes electron transfer and the absorption/activation of CO_2. The adsorption energies of CO_2 on Co-site and Co—N site are −0.66 eV and −0.31 eV, respectively, which are much stronger than that of CO_2 on N-COF (−0.12 eV). The Co—N-COF can achieve a maximum $FE_{formate}$ of 97% and remain above 90% in the range of −0.75 V to −1.05 V. The current density of formate was ≈ 446 $mA{\cdot}cm^{-2}$. The Co sites and Co—N sites reduce the electronic band gap, which is beneficial to the absorption and activation of CO_2, enhances the catalytic activity of CO_2RR, and improves the selectivity of the product.

N-heterocyclic carbenes (NHCs) are highly active species that can form NHC—CO_2 molecular adducts with CO_2 and can catalyze CO_2RR to form methanol. Chang et al. prepared NHC—CO_2 functionalized COFs for CO_2 reduction to methanol.[182] They used Im-COF-1 formed by the condensation of 4, 7-bis (4-formylbenzyl)−1-methyl-1H-benzimidazole (BFMBIm) and 4, 4′, 4′′, 4′′′-(ethylene-1,1,2,2-tetrayl)-tetraphenylamine (ETTA) as the precursor. COF—NHC—CO_2 was formed by post-synthesis modification, and finally, CO_2 was removed by heating to form COF—NHC. After heating, NHC sites were formed and exposed to the substrate. Im-COF-1 crystallized in the triclinic *P1* space group with 1D channel, which was conducive to the next post-synthetic modification. After modification, COF—NHC—CO_2 maintains the crystallinity and framework structure of the precursor, but the CO_2 absorption capacity is significantly enhanced, mainly because NHC—CO_2 has strong CO_2 affinity. DFT calculations showed that the exposed NHC is the real active site, and there are two possible pathways to form the key intermediate product $Ph_2SiH(OCHO)$. In addition, NHC—CO_2 can be regenerated under a CO_2 atmosphere, meaning that COF—NHC—CO_2 is recyclable.

4.4.4 CO_2 Reduction to C_2/C_{2+}

Cu-based catalysts are currently the only metal catalysts that can effectively generate C_2 products due to their moderate binding force with *CO. C_2 products are usually more valuable than single carbon (C_1) products such as CO and are more widely used in the chemical and energy industries. However, the formation processes of C_2 products are more complicated than those of C_1 products, which involve not only the tearing of C═O bond, and the rearrangement of C−O bond and C−H bond, but also the C−C coupling process involving multiple electrons. Mao et al. prepared (Cu/ICTFs) by stabilizing Cu NPs with imidazolium-functionalized cationic covalent triazine skeleton (ICTFs) (**Figure 24a**).[183] The imidazole groups in ICTFs are conducive to the adsorption and activation of CO_2, and the in situ generated NHC can prevent the agglomeration of Cu NPs. Cu/ICTFs still retained imidazole groups and the layered structure had not changed. The imidazole group and triazine

nitrogen improved the affinity for CO_2 and increased the capture capacity of CO_2. The layered structure accelerated the electron transfer to Cu/Cu_2O sites and improved the catalytic activity of CO_2RR. When the content of Cu was 50%, the $Cu/ICTF_{50}$ exhibited an FE of 35% for ethylene (Figure 24b) and a current density of 4.14 $mA{\cdot}cm^{-2}$. The path of Cu/ICTFs catalyzing the reduction of CO_2 to C_2H_4 was as follows: $CO_2 \rightarrow *COO^- \rightarrow *COOH \rightarrow *CO \rightarrow *OCCOH \rightarrow C_2H_4$, where *OCCOH was the key intermediate species for the formation of C_{2+} species. Qiu et al. selected phthalocyanine Cu-based COF with CuN_4 to catalyze CO_2RR to form an acetate product.[184] They prepared 2D PcCu-TFPN (Figure 24c) from copper (II) 2, 3, 9, 10, 16, 17, 23, 24-octahydroxyphthalocyaninate (PcCu-$(OH)_8$) and 2, 3, 5, 6-tetrafluoroterephthalonitrile (TFPN) with a conductivity of 1.71×10^{-5} $S{\cdot}m^{-1}$. At – 0.8 V (versus RHE), FE(acetate) was 90.3%, and the current density was 12.5 mA cm^{-2}. According to ATR-FTIR, $*CH_3$ was a key intermediate for the reduction of CO_2 to acetate. Figure 24d exhibits the feasibility of CO_2 reduction to acetate. The free energy barrier for the formation of acetate is thermodynamically feasible. On the contrary, the formation of CH_4 requires $*OCH_3$ intermediate with a large energy barrier, which limits the formation of CH_4. The electron density of PcCu-TFPN is 2.71 $e{\cdot}Å^{-3}$ (Figure 24e,f), which is larger than those of CuSAs and Cu-porphyrin, indicating stronger electron delocalization. Figure 24g shows that the adsorption energy of *CO on CuSAs is −0.03 eV, which is beneficial to the desorption of CO. The energy barrier of PcCu-TFPN to produce $*OOCCH_3$ is much lower than that of Cu-porphyrin, which indicates that PcCu-TFPN is more conducive to the formation of acetate, while Cu-porphyrin is more conducive to the formation of CH_4 (Figure 24h). PcCu-TFPN is a single active site catalyst, and the isolated Cu-phthalocyanine site is more conducive to the formation of acetate.

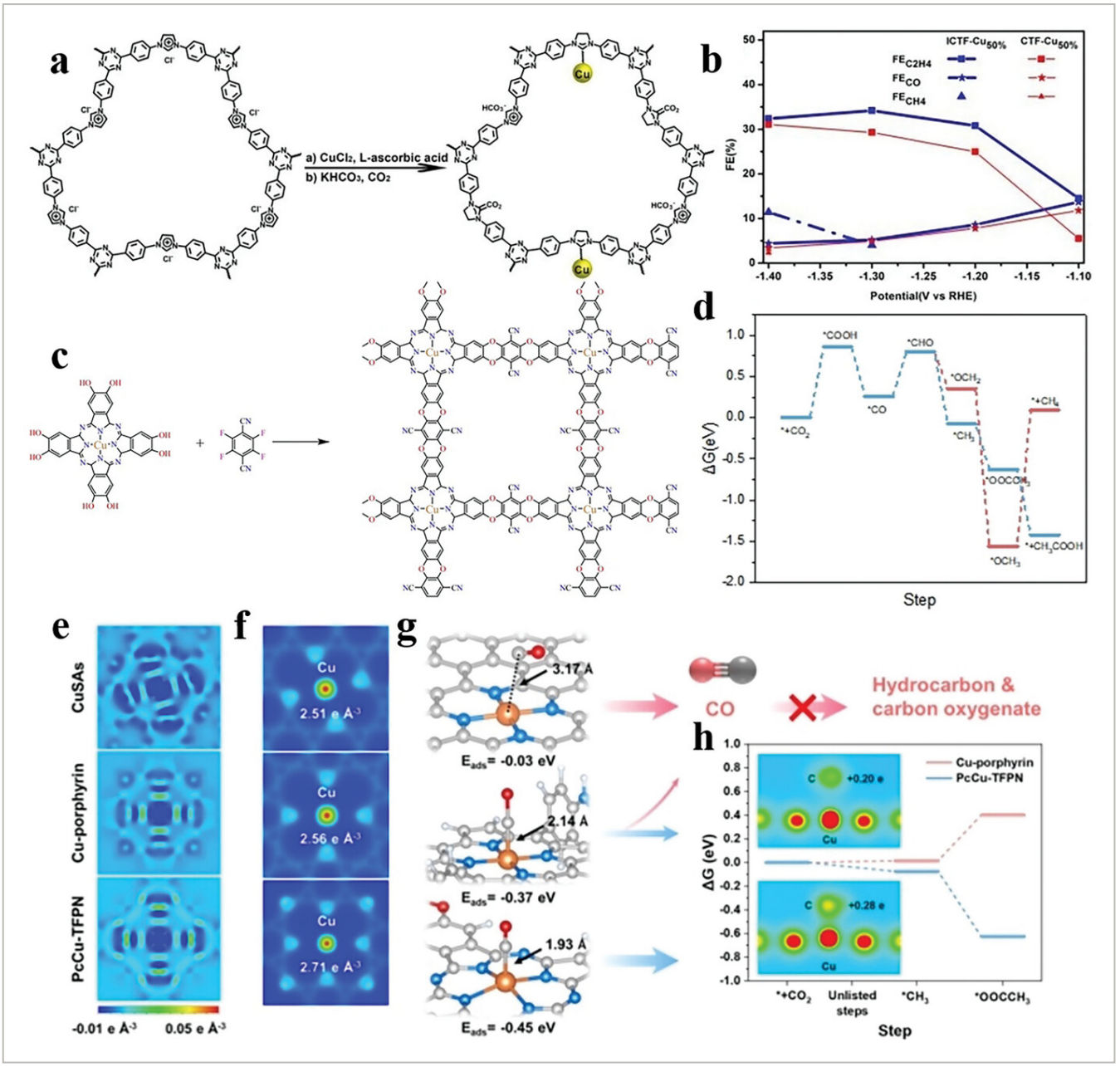

Figure 24

Open in figure viewer | PowerPoint

a) Synthesis of Cu/ICTF. b) FE of CO_2 reduction products. Reproduced with permission[183]. Copyright 2020, Wiley-VCH. c) Synthesis of PcCu-TFPN. d) Free energy diagrams. e) Charge density differences. f) Electron densities. g) Optimized structures of *CO intermediates. h) Free energy diagrams of $*CH_3$ and $*OOCCH_3$. Reproduced with permission[184]. Copyright 2022, Wiley-VCH.

4.4.5 CO_2 Reduction to C_3/C_{3+}

C_{3+} products, such as n-propanol, usually have higher economic value than C_2 and C_1. However, the formation of C_{3+} products requires more intermediates and subsequent C—C coupling, and thus the reduction of CO_2 to C_{3+} is more difficult and less selective. Du et al. designed a catalyst with multiple active sites to reduce CO_2 to C_3 product.[185] They designed

a FeCo—Pc—Ni—O—COF catalyst composed of a 2D COF constructed by a FeCo-Pc ligand and a square planar NiO_4, which reduces CO_2 to n-propanol by a tandem reaction. The ΔG of CO* → CHO* and *CO + *CHO → *COCHO on Fe-Co-Pc are low, which means that C—C coupling is more likely to occur. The D-band value is moderate, which is more conducive to the desorption of the product. NiO_4 is beneficial to the adsorption and desorption of CO intermediate. The *CH_3CHO adsorbed on FeCo-Pc and CO desorbed from NiO_4 undergo C_2 coupling to produce n-propanol. C_1-C_2 coupling could produce three different structures: $CH_3CHOCOH$*, $CH_3CHOCHO$* and $CH_3CHOHCO$*. DFT calculations showed that the energies of these intermediates are 0.25, −0.20, and −0.31 eV, respectively. Thereby, $CH_3CHOCOH$* is thermodynamically excluded. In the subsequent protonation and dehydration process, the free energy of $CH_3CHOHCO$* → CH_3CHCO* is 0.83 eV, which is lower than that of other intermediates. The synthesis process of $CH_3CH_2CH_2OH$ is as follows: *CO + *CO → *CO + *CHO → COCHO* → CHOCHO* → CHOCHOH* → $CHOCH_2OH$* → $CHOCH_2$* → $CHOCH_3$* + CO → $CH_3CHOHCO$* → CH_3CHCO* → CH_3CHCHO* → CH_3CH_2CHO* → $CH_3CH_2CH_2O$* → $CH_3CH_2CH_2OH$. NiO_4 and FeCo-Pc are dual active sites in FeCo—Pc—Ni—O—COFs, and they work independently. The desorbed CO on the NiO_4 is rapidly transferred to the FeCo-Pc site for C_1—C_2 coupling to form n-propanol.

Since the products of CO_2RR are very complex, it has been widely studied for improving the selectivity of a target product. Metal-based porphyrins, metal-based titanium cyanines, and even metal-functionalized s-triazine complexes in COFs have high CO selectivity. Cu-based catalysts can catalyze CO_2RR for the production of hydrocarbons and oxygen-containing compounds. Hence, for the produce of CH_4, HCOOH, CH_3OH, CH_3CH_2OH, and other products, transition metal Cu is generally chosen to combine with organic ligands. For example, Cu aggregates, including SA, NCs, and nanoparticles are limited to grow in the abundant pores of COFs to form Cu-COFs to promote the reduction of CO_2 to hydrocarbons. In addition, N and F co-doped s-triazine are also conducive to the generation of CH_4, and the introduction of Co single atoms into COFs with high N content will generate formate.

5 Optimization Strategies of COFs and their Derivatives

COFs have large specific surface area, low skeleton density, strong stability, and adjustable pore size molecular network, which make them have broad application prospects in the field of electrocatalysis. In recent years, the COF family has been expanding, and Schiff base, imine, triazine, and other series have emerged. At the same time, with the deepening of research, the stability and electron transport properties of COFs have been greatly improved. Hence, COFs with special structure and functionalization have great application potential. Here, we proposed optimization strategies for improving the electrocatalytic performances of COFs and their derivatives (**Figure** 25).

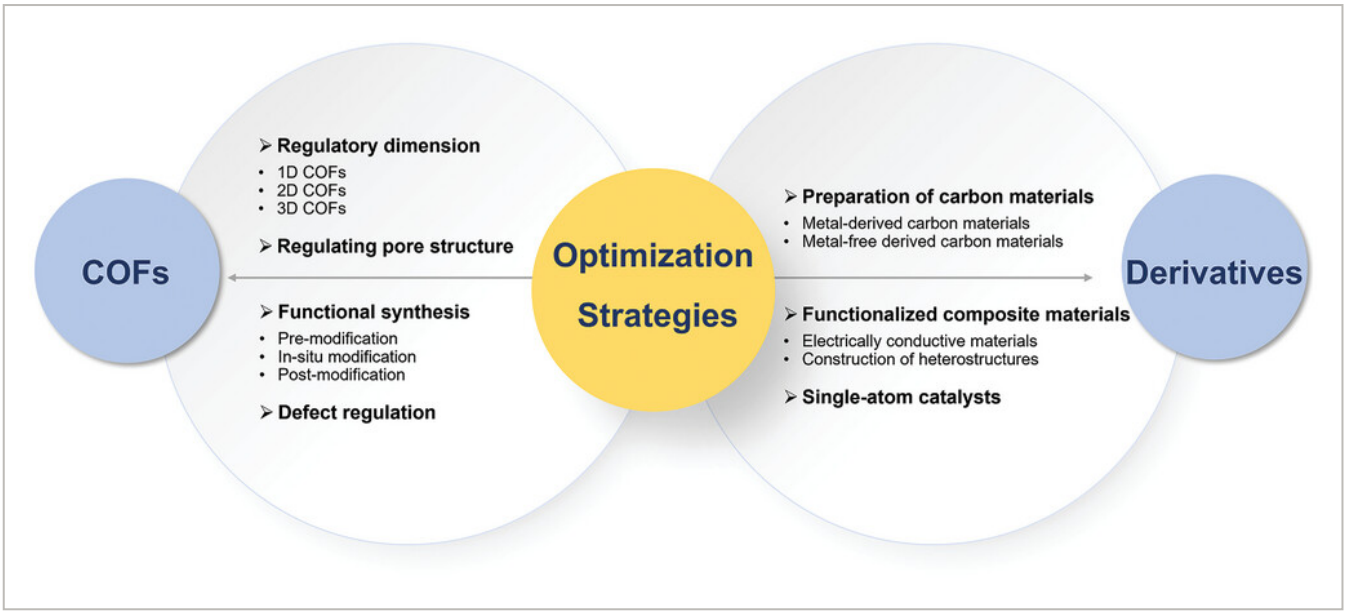

Figure 25

Open in figure viewer | PowerPoint

Optimization strategies for COFs and their derivatives.

5.1 Optimization Strategies of COFs

5.1.1 Regulatory Dimension

5.1.1.1 Framework

1D structure is a linear structure extending in one direction, and 1D COFs are constructed by 1D confined covalent bonds interacting with non-covalent bonds (such as π–π interactions and hydrogen bonds) in the vertical 2D direction. 1D COFs have high crystallinity, high specific surface area, and excellent stability. In addition, the small micropore structure and the large ring cavity generated in 1D COFs are beneficial to the adsorption of CO_2. Zhang et al. selected porphyrin groups as building blocks and connected each porphyrin group with four nonlinear right-angle carbazoles to form a 1D linear structure (COF-K), which crystallized in the triclinic *P1* space group.[186] At present, the smallest pore size of 2D porphyrin [4 + 2] COFs was 1.8 nm, while the pore size of COF-K was only 1.25 nm. The smaller pore size and pyrrole-containing macrocyclic cavity are conducive to the adsorption of CO_2 and enhance the catalytic activity of CO_2RR. The adsorption capacity of COF-K was 89 $mg{\cdot}g^{-1}$ at 298 K and 1 bar, which was higher than that of 2D porphyrin-based COF. However, the synthesis of 1D COFs is hindered by anisotropy and entropy-driven organic units, and thereby 1D COFs reported so far are not common.

5.1.1.2 Framework

2D COFs have attracted much attention due to their synergistic properties combined with porous graphene-like structures. Due to the strong designability of the planar structure of

2D COFs and the mature synthesis technology, they have been widely explored. As electrocatalysts, 2D COFs have multiple advantages: one is that the planar structure of 2D makes COFs have a larger specific surface area and closer active sites, which can reduce the mass transfer barrier. The second is that the face-to-face stacking mode of the 2D plane has a larger π orbital overlap, which can promote the migration of charges in the frame.[187] The third is to combine the strong covalent bonds of non-metallic elements with the 2D COFs skeleton to make them have low density and permanent porosity.[188] Liu et al. prepared 2D COF films with controllable thickness by vapor deposition.[189] By coupling 4, 4′, 4″, 4‴-(1, 3, 6, 8-tetrakis(4-aminophenyl)pyrene (PyTTA) with terephthalaldehyde (TPA) via Schiff base, 2D PyTTA-TPA COF with a thickness of 30 nm was prepared. The carrier transport rate of the film can reach 1.89×10^{-3} $cm^2 \cdot V^{-1} \cdot s^{-1}$. Many Schiff base-linked 2D-COFs have formed hexagonal sheets similar to graphene despite their different degrees of functionalization. The phenazine connection makes 2D-COFs have a rigid structure with a high plane in the graphene-like layer, showing good chemical stability and efficient hole conduction mobility. In addition, the phenazine-linked 2D-COFs possess uniform hexagonal pores and N atoms, forming N doping with higher N content.[190] Unlike N-doped graphene, where the N content and N doping position cannot be controlled, the N content and doping position in N-doped 2D-COFs are controllable. Graphdiyne (GDY) is a 2D artificial carbon allotrope formed by two acetylene bonds (-C≡C─C≡C─) of the aromatic ring.[191] GDY has sp-and sp^2-hybridized carbon atoms and natural semiconductor band gaps, which are conducive to exposing more sites and increasing carrier migration rate. Huang et al. prepared a GDY analog (PDY) and combined it with Co-porphyrin to form 2D Co-PDY.[192] Co-PDY was formed by four phenyl porphyrin ring repeating units connected by diacetylene bonds, in which the extended pores of the π-conjugated carbon skeleton were evenly distributed on the PDY plane. This conjugated structure not only produces more Co─N_4 active sites but also produces a large pore of 2.34 nm and a narrow band gap of 2.1 eV on the 2D plane, which improves the carrier migration rate and conductivity.

5.1.1.3 Framework

The unique advantages of 3D COFs in the field of electrocatalysis mainly include: 1) Different from the in-plane conjugation of 2D COFs, the entire 3D framework in 3D COFs is conjugated to ensure charge transfer within the framework. 2) Different from 1D channels in 2D COFs, the pores of 3D COFs are interconnected, which is conducive to rapid mass transfer. 3) Different from the face-to-face layered stacking in 2D COFs, 3D COFs have spatially separated building blocks, which is conducive to the complete exposure of active sites. Wang et al. synthesized a fully conjugated 3D COF by condensation of a fully thiophene-linked saddle-shaped conjugated building block with 1,4-diaminobenzene (DAB).[193] This fully conjugated 3D COF is a semiconductor material, which not only has abundant pores and active sites but also has a 3D π-expanded structure. Hence, fully conjugated 3D COFs can break the layer-layer charge transport barrier in 2D COFs and effectively ensure charge transport, making metal-free 3D COFs exhibit excellent ORR activity. Shao et al. constructed

a 3D porphyrin-based COF connected by covalent imine bonds through a Schiff base condensation reaction, which was named 3D-Por(Co/H)-COF.[177] The separation of Co-porphyrin as building blocks in 3D-Por(Co/H)-COF leads to the complete exposure of Co—N_4 active sites, which is beneficial to the adsorption and activation of CO_2 and improves the catalytic activity of CO_2RR. Li et al. prepared 3D COF-112Co and COF-112Fe by solvothermal method using 2, 6-pyridinedicarboxaldehyde, 4-(tert-butoxycarbonylamino)-aniline and metal (II) tetrafluoroborate hexahydrate.[194] According to XRD, both 3D COFs are non-interpenetrating structures with **dia** topology and rich pore space, which are conducive to rapid mass transfer in a rigid framework. Unlike 2D COFs, 3D COFs are still challenging in terms of structural designability and controllability.

The diversity of dimensions and structures of COFs mainly depends on the availability of topology and building units. Among them, the topology design of 2D COFs is the most common, mainly because the synthesis technology is mature and 2D COFs have multiple advantages as electrocatalysts. In addition, 2D COFs not only have a fully ordered π array but also have 1D open channels. Compared with 2D COFs, 3D COFs have unique advantages in the field of electrocatalysis, such as their interconnected channels. However, compared with 2D COFs, 3D COFs are still challenging in terms of structural design and controllability. Equally, 1D COFs are not common because they are hindered by anisotropy and organic unit entropy.

5.1.2 Regulating Pore Structure

The topological structure of COFs can be designed by utilizing the geometry of the monomer to achieve different skeletons and pores. The size and shape of the pore and the control of the pore wall environment are affected by the geometry of the monomer and the connection mode. At present, the pore size of COFs can be accurately controlled from nanometer to micron size, and different pore sizes will have different effects.[40a] If the framework is a small microporous structure, the specific surface area of the material is generally larger than other porous materials; while if the framework has a large pore structure, the material is more conducive to the rapid mass transfer during the catalytic process and the exposure of active sites. Zhao et al. prepared macro-TpBpy-Co with high porosity and macroporous structure by template-assisted method, in which polystyrene spheres (PSs) were used as the hard template, and the size of the pores can be adjusted by controlling the size of PSs.[111] The total pore volume of macro-TpBpy was 1.23 $cm^3 \cdot g^{-1}$, which was much higher than that of the original TpBpy (0.381 $cm^3 \cdot g^{-1}$), indicating that PSs successfully introduced additional macropores into macro-TpBpy. According to the cross-section SEM, obvious uniform macroporous structure can be observed, which plays a key role in the exposure of active sites and mass transfer during OER catalytic process. Li et al. prepared 3D COF with STP topology, with a specific surface area of up to 3300 $m^2 \cdot g^{-1}$ and a pore size of up to 43 Å.[195] The larger pore structure can effectively enhance the transport of substances in the catalytic process and increase the accessibility of the active surface. The pore wall environment is also an important factor affecting the catalytic activity of COFs. At

present, pore surface engineering is a general and effective strategy, which is to immobilize hydroxyl, azide, or alkyne reactive group functionalized linkers into the pores.[196] These functional groups can create specific interfaces on the pore wall, and combine the advantages of the pore itself to control the interaction with the guest element particles, charges, ions, and molecules, thereby creating new physical and chemical properties and functions, and improving catalytic activity.[197] Hao et al. installed multiple functional groups such as -C═N-, -OH, ─N═N- and -CF_3 into COF pores to improve the utilization efficiency of proton carriers.[198] This work enlightens us that pore surface engineering can be more widely used in the field of electrocatalysis.

5.1.3 Functional Synthesis

The properties and applications of COFs are determined by the functional groups and pore structures connected by the skeletons. At present, the commonly used methods for preparing functionalized COFs include pre-modification, in situ modification, and post-modification.

Pre-Modification Method

The pre-modification functionalization method refers to the combination of special functional units with other structural units before the synthesis of COFs, so that the functional groups can be evenly distributed in the COF and the position of the active site on the skeleton can be accurately controlled.[199] Nowadays, many important functional organic chemical functional groups have been gradually introduced into the skeleton of COFs. Substituting C atoms with N, P, and S with different electronegativity can effectively adjust the electronic structure and catalytic activity of carbon-based catalysts, but it is difficult to control the doping sites during heteroatom doping. COFs have a coordinated and controllable framework to control heteroatom-doping sites. In addition, ordered structures and arrays in COFs can provide channels for electron transfer. Ma et al. condensed thieno[3, 2-b] thiophene-2, 5-dicarboxaldehyde (TTDC) containing thiophene-S with 1, 3, 5-tris(4-aminophenyl) benzene (TAPB) to form S-doped COF, denoted as JLNU-300.[200] JLNU-300 existed in the space group $P6_3/m$ in the form of AA stacking. In JLNU-300, C, N, and S atoms are evenly distributed. The S doping increases the electronic energy level and the number of electrons, leading to the formation of an electron-rich structure of the thiophene S unit. This electron-rich structure can be used as an electron donor to react with H^+ to improve HER catalytic performance. Thiadiazole is a high N-content substance that can provide more active sites. Bhaumik et al. incorporated thiadiazole into imine-linked COF for the OER.[162] The heteroatoms in thiadiazole are rich in electrons and can be quickly transferred along the pore array in the framework. The diarylamine unit can be used as an electron donor and the core of redox. Liu et al. integrated diarylamine derivatives into the Co-porphyrin framework to form bifunctional Co-COFs for the OER and ORR.[32] This active unit can not only promote electron transport but also improve the active specific surface area.

In Situ Modification Method

There are some COFs in which the bond structure formed by synthesis reactions itself has certain active sites and can be used in the field of electrocatalysis. For instance, Zhang et al. prepared FePc-BBL COF with a double-chain trapezoidal structure,[154] which is composed of imide and imine groups and has excellent chemical and mechanical stability. In addition, BBL with a trapezoidal structure can improve the field-effect migration rate. FePc-BBL COF exhibited excellent ORR activity due to the strong covalent bond of BBL and the uniformly dispersed Fe─N_4 active sites. Cao et al. prepared NiPc-COF by connecting nickel phthalocyanine to conjugated 2D COF through a conductive pyrazine bond.[201] NiPc-COF achieved π-delocalization in the monolayer and out-of-plane π–π stacking along the *c*-axis, and the extended conjugation was connected by the intrinsic conductive pyrazine. The extended conjugated structure connected by the intrinsic conductive pyrazine provides more effective electron transfer, improves conductivity, and enhances the activity of CO_2RR. In addition, the stability of NiPc-COF was improved due to the covalent pyrazine linkage. The in situ functionalization modification method is very simple, but it is not suitable for most COFs, and therefore COFs synthesized by in situ functionalization method are very limited.

Post-Modification Method

The post-modification functionalization method is the most commonly used method to synthesize functionalized COFs, mainly by introducing functional groups with different properties into the pores.[197, 202] Generally, the functional groups with high reactivity are selected as the anchor points of the building units. The COFs are synthesized and then continue to react with the functional groups containing the target functional groups under mild conditions to connect the target functional groups on the skeleton. Metal coordination post-modification is a common post-modification functionalization method. Kurungot et al. prepared bipyridyl COF and then added Co^{2+} to synthesize Co-TpBby.[203] Co^{2+} was coordinated with the N atom of bipyridine to realize the charge transfer. Liang et al. post-functionalized COFs by anchoring single Co atoms.[181] Due to the modification of co-coordination, the band gap of the anchored Co atom was significantly reduced. This means that electrons are transferred from the top of the valence band to the bottom of the conduction band, which is beneficial to the absorption and activation of CO_2. Lan et al. prepared two 1D superstructured anthraquinone-based COFs, namely NSs and HT structures.[204] Two Cu-based catalysts with excellent CO_2RR activity were obtained by modifying the superstructure of the anthraquinone-based COFs. The post-modification was carried out by heat-assisted reflux, and the treated COF structure was retained. Transition metal Cu interacts with COF, and the carbonyl group in COF can change the electron cloud density around Cu. Most importantly, Cu is currently recognized as one of the few transition metals that reduce CO_2 to hydrocarbons. Accordingly, post-modification with Cu ions can improve the selectivity of hydrocarbons. Compared with the pre-modified functionalization method, although the post-modified functionalization method is easy to connect functional groups to the skeleton of COFs, the skeleton structure, crystallinity, and porosity of the material may be destroyed during the modification process. Therefore, exploring suitable

post-modification functionalization methods is very important for the synthesis of functionalized COFs.

The crystal structure, framework properties, pore structure, functional groups, active sites, and stability of COFs are affected by the construction unit, connection type, and topology.[205] The type of building units determines the basic chemical properties and functional sites of COFs, which provide the basis for the crystal structure and various applications.[206] The connection type determines the stability and synthesis conditions of COFs. The topological structure depends on the symmetry of the building unit, which affects the pore characteristics, stacking mode, interpenetration type, functional unit position, and other properties of COFs.[40b] It is feasible to prepare functionalized high-performance electrocatalysts by pre-regulating the construction unit, connection type, and topology of COFs.[207]

5.1.4 Defect Regulation

The surface composition of catalysts can be precisely controlled at the atomic scale by defect regulation, constructing the local microenvironment, regulating the electronic structure, and promoting the catalytic activity. When constructing COFs, a structure rich in N atoms can be selected to create N defect sites. For example, there are abundant N atoms in the covalent triazine skeleton, which is beneficial to expose more active sites. In addition, heteroatoms such as B/N/P/S can be doped into COFs to form doping defects, such as sulfur-containing pentagonal defects, which can promote charge transfer. For metal-based COFs, the creation of defect vacancies can regulate the coordination environment of metals and improve the catalytic activity by introducing coordination of unsaturated center defects. The introduction of new functional atoms or molecules into defect sites to give COFs new functions provides a new method for post-modification synthesis.

5.2 Optimization Strategies of COF Derivatives

5.2.1 Preparation of Carbon Materials

Carbon materials have great application potential in the field of catalysis due to their high charge conductivity, ordered transport channels, and heteroatom-rich sites.[208] Heteroatom doping can change the electronic structure, vibration mode, chemical activity, and mechanical properties of carbon substrates to meet the needs of practical applications.[209] The unique structural characteristics of COFs determine their potential as precursors for the fabrication of porous carbon materials. At present, there are many reports on COF-derived carbon materials for electrocatalysis, which are mainly divided into metal-free carbon materials and metal-containing carbon materials. Among them, metal-free carbon materials are not conducive to electrocatalysis because of the lack of metal sites, which have been less reported. Metal-containing carbon materials have rich metal ions as active sites and have received extensive attention in the field of electrocatalysis. However, metal ions may agglomerate during pyrolysis and reduce the exposure of active sites. Accordingly,

preventing the aggregation of metal ions during the preparation of metal-containing carbon materials is the key to improving the electrocatalytic activity.

COF-Derived Metal-Free Carbon Materials

Although COF-derived metal-free carbon materials lack metal active sites, researchers have found some methods to improve their catalytic activity. The most common method is doping heteroatoms such as N, P, and S into carbon materials.[210] These heteroatoms can not only be used as active sites for electrocatalysis but also have different electronegativity, which can affect the charge distribution of surrounding carbon atoms. The doping of heteroatoms such as N and S may also affect the specific surface area and pore size of carbon materials. You et al. used naphthyl COF as a precursor to prepare an efficient ORR electrocatalyst CPN-NS by N/S heteroatom co-doping.[211] After the introduction of N/S atoms, the number of mesopores/micropores in carbon materials increased significantly, and the BET surface area increased. At the same time, the addition of sulfur can adjust the relative composition of nitrogen. The content of oxidized N in the catalyst decreased, while the content of pyridine N and pyrrole N which were beneficial to ORR catalysis increased. CPN-NS achieved a high $E_{1/2}$ of 0.868 V in 0.1 M KOH. The introduction of heteroatoms not only effectively increases the total nitrogen content and active nitrogen content of the carbon material, but also greatly increases the specific surface area, thus exhibiting excellent ORR catalytic activity. Jiang et al. prepared COF-derived N-doped carbon nanospheres (N-COF) and optimized the pyrolysis temperature.[156] The N-COF-n (*n* = temperature) formed at different pyrolysis temperatures retains the spherical morphology. However, the pores and defects of the nanosphere framework increased with the increase in temperature, and the corresponding specific surface area and pore volume also increased gradually. According to the pore size diagram, as the temperature increased, the ultra-small pores increased first and then decreased, and the large pores increased. During the initial heating process, the combustion of N and O generates ultra-small micropores, but as the temperature increases, the combustion of N and O species increases the micropores to form larger micropores. XPS showed that high temperature contributed to the formation of graphite nitrogen and improved the conductivity. The increased specific surface area, enhanced graphitization degree, and appropriate ultra-small microporous structure (defects) make N-COF-n exhibit ORR catalytic activity similar to that of commercial 20% Pt/C.

In addition, edge engineering can be used to improve the catalytic activity of carbon materials. Compared with the inner basal carbon, the carbon edge has electron localization and unpaired electrons, which makes the carbon edge more active and more conducive to improving the catalytic activity. Liu et al. pyrolyzed COF with abundant micropores and mesopores to prepare carbon materials with rich carbon edges (COF_x, x: temperature).[212] After pyrolysis, COF_{800} well inherited the morphology and structure of the precursor, and there were abundant pores on its surface. Differently, the carbon sheets composed of curved graphite layers had sharp edges, confirming the generation of carbon edges. After pyrolysis, the nitrogen in the precursor framework formed abundant pyridine nitrogen and

graphite nitrogen, which increased the active nitrogen content and improved the conductivity. The rich carbon edge sites and uniform nitrogen doping make the catalytic ORR activity of COF_{800} similar to that of commercial Pt/C.

COF-Derived Metal-Containing Carbon Materials

The realization of non-precious metal catalysts replacing precious metal catalysts is the unremitting pursuit of researchers. At present, related research has made great progress, such as MOFs, metalized COFs, and their derivatives. Some non-noble metal catalysts comparable to noble metal catalysts for a single electrochemical process have appeared. Since there are metal ions or clusters in MOFs, the metal nodes will be transformed into nanoparticles during the pyrolysis process. However, it is difficult to control the size and metal content. In contrast, COFs are ideal precursors for the preparation of non-precious metal catalysts. The main advantages are as follows: 1) The structure and function of COF can be designed in advance to form a specific functionalized precursor. 2) The density of COF is low. During the pyrolysis process, active substances and carbon supports are generated simultaneously. 3) The larger specific surface area and abundant pores avoid the accumulation and agglomeration of active components during pyrolysis.[213] Peter et al. annealed s-tetrazine-based COF (TZA-COF) with graphene oxide and metal Co composites as precursors (TZA-COF-rGO-Co) to obtain N-doped graphite carbon Co@NC-600 (**Figure** 26a).[214] After pyrolysis, the degree of graphitization increased, and many N-rich defects were formed on the graphite carbon matrix. Elemental analysis showed that the relative Co content increased from 6% to 12% after pyrolysis, which proved that the pyrolysis made Co embedded in the carbon matrix. The C—N bond of the encapsulated Co particles is the actual active site and Co can optimize the electronic structure of the N-doped carbon matrix, which makes Co@NC-600 exhibit high activity and selectivity in the ORR. Multi-metal COF-derived carbon materials provide more metal ions, and the synergistic effect of multiple metals is more conducive to improving the catalytic activity. Zhu et al. selected triazine SNW-1 with a conjugated nitrogen-rich structure anchored by bimetallic Fe/Co as the precursor to form FeCo@SNC by pyrolysis (Figure 26b).[108] FeCo@SNC has abundant and uniformly dispersed Fe, Co, and N atoms and inherits the porous structure of COF precursor, which promotes the transport of electrons and protons in the OER. More graphite carbon and defect carbon were produced during pyrolysis, which increased the conductivity of FeCo@SNC. A small amount of Fe can optimize the electronic structure of the active site Co, and the synergistic effect of Fe and Co improves the catalytic activity of OER. Zhao et al. prepared a porous COF-derived material (m-CoRu@NC) as a bifunctional electrocatalyst for HER and OER (Figure 26c).[215] During the pyrolysis process, COF was carbonized to form a carbon matrix, and CoRu alloy was anchored on a macroscopic microporous carbon skeleton with 3D ordered interconnection (Figure 26d,e). Ru was doped into the lattice of Co to form Co—Ru bond. Due to the positive charge of Co, electrons were transferred from Co to Ru, which promoted HER kinetics. Figure 26f,g shows that the CoRu nanoalloy was easier to adsorb and activate H_2O, and the ΔG_{H*} of Ru site was closer to 0 V, which was beneficial

to the adsorption and desorption of H*. In the OER, the synergistic effect between Co and Ru made the η_{10} of m-CoRu@NC (280 mV) lower than that of RuO_2. The design and synthesis of novel COFs and the optimization of their structure, composition, and post-treatment conditions will make it possible to obtain novel, efficient, and stable non-precious metal catalytic materials.

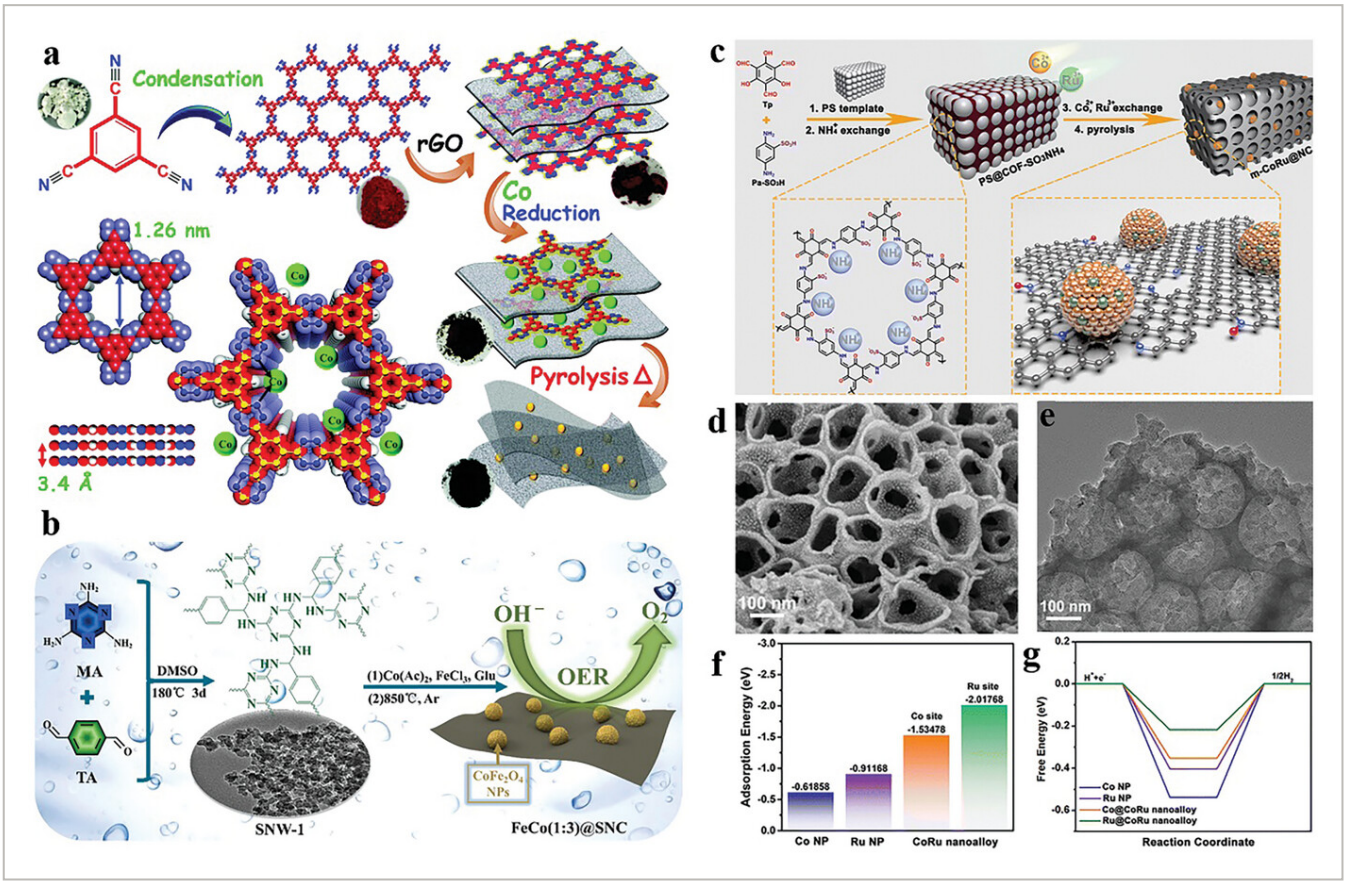

Figure 26

Open in figure viewer | PowerPoint

a) Synthesis and structure of Co@NC-600. Reproduced with permission[214]. Copyright 2020, Royal Society of Chemistry. b) Synthetic of FeCo@SNC. Reproduced with permission.[108] Copyright 2022, Elsevier Ltd. c) Synthesis of m-CoRu@NC. d) SEM and e) TEM image of m-CoRu@NC. f) H_2O adsorption energy. g) Free energy diagram. Reproduced with permission[215]. Copyright 2022, Royal Society of Chemistry.

5.2.2 Functionalized Composite Materials

Electrically Conductive Composite Materials

One of the factors limiting the catalytic activity of COFs is poor conductivity. Researchers have done profound research on improving the conductivity of COFs, such as adding heteroatoms containing lone electron pairs to COFs or adding metals with redox properties.[216] Moreover, researchers prepared COF derivatives with high conductivity to increase the electron cloud density of delocalized large π bonds, which can be also achieved by introducing other substances into COFs to form a conjugate effect. Ye et al. introduced

Co/CoO NPs into imino COF to form Co/CoO@COF catalyst for the OER. Co/CoO NPs were supported on the COF, breaking the π–π conjugated structure, which was beneficial to enrich active sites.[117] The 3d orbital of Co atom accepted the lone electron pair provided by N atom in the COF, and thereby Co/CoO NPs formed a conjugate effect with COF, improving the bonding strength of electron-rich benzimidazole unit, which was beneficial to the rearrangement of the large n-bond electron cloud density and the redox reaction at the interface. Co—N coordination not only increased the electron cloud density and improved the conductivity, but also reduced the barrier of O-O bond formation and promoted the OER catalytic activity. Another way to improve the conductivity is to introduce highly conductive materials into COFs to form composites. Chen et al. selected a highly conductive polymer 3, 4-ethylenedioxythiophene (PEDOT) as a coating to combine with Pd-loaded COF to form a composite material COF@Pd@PEDOT.[217] The formation of PEDOT coating greatly improved the conductivity of the composite. More importantly, it regulated the fusion growth of Pt NPs, thereby forming highly dispersed catalytic sites. The most common way to form highly conductive composites is to introduce carbon-based materials, such as graphene oxide and carbon nanotubes (CNTs). The conductive carbon substrate can balance the mass transfer and electron transport in the catalytic process, thereby exhibiting high electrocatalytic activity. Xu et al. in situ prepared 2D COF composites on the surface of CNTs, which had π–π stacking interactions.[218] The calculation of conductivity showed that the conductivity of pure COF was 5.8×10^{-10} S·m^{-1}, while the conductivity of COF@CNTs was 0.066 S·m^{-1} to 2058 S·m^{-1}, indicating that CNT increased the conductivity. Yang et al. coated COF on CNT to form COF-CNT, which showed an $E_{1/2}$ of 0.79 V and a diffusion current density of −5.5 mA·cm^{-2} in the ORR.[219] After binding with CNT, the TOF of COF-CNT increased by two orders of magnitude and the impedance decreased significantly. Theoretical calculations showed that there was an electronic interaction between COF and CNT, and the transfer of electrons to N atoms led to the enhancement of the intrinsic activity of COF. The combination of COFs and conductive carriers is beneficial to the transport of protons and electrons in the catalytic process, which is a feasible way to enhance electrochemical performance.

Construction of Heterostructures

The heterogeneous interface region formed between two semiconductors with similar thermal expansion coefficient, atomic spacing, and crystal structure is called heterojunction. MOF and COF as two semiconductors with energy band matching can form heterostructures to improve electrocatalytic activity.[208, 220] Wang et al. grew ZIF-67 on benzoic acid-modified COF to form ZIF-67/COF composite by top-down method.[221] After pyrolysis, Co_3O_4 was highly dispersed in N-doped porous carbon to form Co_3O_4/NPC. The unique interface formed between MOF/COF-based hybrid derivatives can create charge transfer channels and reduce band gaps. DFT calculations showed that Co_3O_4/NPC had unique geometric and electronic effects, which had a positive effect on the adsorption and desorption of O_2. Molybdenum disulfide (MoS_2) has excellent physical and chemical properties.[222] The 2D

heterostructure formed by decorating COF with MoS_2 can regulate the appropriate band structure and accelerate the interface OER kinetics. Zhang et al. used COF-C_4N as a substrate to synthesize N-doped MoS_2 in situ on the bottom to form N-MoS_2/COF-C_4N with vertical heterostructure.[223] The heterostructure can enhance charge transfer and promote overall water splitting. Experiments and calculations showed that the formation of vertical heterostructures exposed more active sites and improved the catalytic activity. In addition, N doping led to the formation of defect sites, which makes the catalyst have appropriate hydrogen-free radical adsorption and desorption-free energy. PEDOT@Metal-Salen COF with heterostructure was prepared by combining PEDOT with high conductivity as an electron transport cable and Metal-Salen COF.[132] Heterostructures not only induce intramolecular charge transfer but also construct interfacial active sites with high activity, which is beneficial to the HER.

5.2.3 COF-Derived Single-Atom Catalysts

The active components in SACs exist completely in the form of isolated single atoms, and the number of atoms at the metal site is only one atom. Compared with traditional catalysts, SACs have higher utilization of metal atoms and significantly reduce the use of precious metals.[224] They have the advantages of low cost, high catalytic activity, excellent selectivity, and stability, and have broad application prospects in the field of electrocatalysis.[225] COFs and their derivatives are considered to be excellent carriers for isolated single-atom site (ISAS) anchoring.[226] Compared with MOFs, COFs do not contain metals after pyrolysis, which effectively avoids the interference of metal elements as carrier impurities. However, the unique porous structure and nitrogen-rich properties of COFs make them more conducive to limiting single metal atoms. Wang et al. prepared Fe-SAC/COF with single metal Fe active sites by limiting Fe-SAC to COF at low temperatures.[109] FT-EXAFS analysis showed that the absence of a Fe—Fe bond in Fe-SAC/COF confirmed the single atom state of Fe. Fe may form a unique Fe—N/O coordination with one O and one N in the COF. DFT calculations showed that efficient atom utilization and unique Fe—N/O coordination reduced the free energy of key intermediates in OER and improved OER kinetics. Wei et al. anchored Fe ISAS on COF-derived N-doped carbon nanospheres to form Fe-ISAS/CN.[227] After pyrolysis, Fe, C, and N elements were uniformly dispersed on the substrate, and no metal nanoparticles were found, which proved that Fe element was dispersed on N-doped carbon nanospheres in the form of Fe single atom sites. Fe-ISAS/CN exhibited better ORR catalytic activity than 20 wt.% Pt/C. Yang et al. prepared single-atom catalysts by directly pyrolyzing Fe-COF.[228] The sp^2 carbon-linked COF was directly converted into a 2D carbon material. After pyrolysis, there were no aggregated metal particles on the surface, and the carbon defects were well retained after the addition of Fe element. EXAFS analysis showed that the configuration in Fe-COF_{900} was mainly two Fe atoms sharing two adjacent N atoms and the distance between Fe—Fe was much smaller than the distance between the graphite layers, and thereby the Fe—Fe linkage could be excluded. DFT calculations showed that this ultra-close single-atom site structure optimized the formation of *OH in ORR.

6 Summary and Prospects

6.1 Summary

As emerging crystalline porous materials that can be designed, COFs show unique advantages in the diversity of structure and properties, far exceeding the capabilities of other porous materials. This review paper introduces the structural design of COFs from the two aspects of dimensions and connection bond types. The crystal structure of COFs can be pre-designed by topological structure design combined with specific covalent bond polymerization connection between monomers to guide the growth of ordered structure. According to the topological structure design, 2D COFs can theoretically be composed of arbitrary polygonal frame structures, while 3D COFs can theoretically be composed of arbitrary polyhedron structures. Through the mature development of organic chemical methods, a variety of structurals with special functions can be synthesized and combined with topological theory. They are connected by covalent bonds and orderly stacked into crystalline COFs, realizing the practical applications. The high crystallinity and high porosity of COFs need to be formed by the assembly of organic block network structure under certain reaction conditions, and thereby it has high requirements for pressure, temperature, and solvent in the synthesis process. More importantly, during the formation of covalent bonds, adjusting the thermodynamic equilibrium is the key to forming a highly ordered covalent network. This paper summarizes four common synthesis methods, including solvothermal synthesis, ionic liquid synthesis, microwave-assisted synthesis, and mechanical grinding. Through these methods, powder, film, fiber, and single-crystal COFs can be successfully synthesized.

The specific surface area characteristics of COFs are similar to those of zeolites, MOFs, and amorphous porous organic polymers, which often show large porosity, pore size, and surface area. In addition, they can be used for gas adsorption and separation, small molecule catalytic reaction, ion and molecular separation by modifying the pores. Therefore, the applications of COFs in various fields are in the stage of explosion, especially in the field of electrocatalysis. At present, COFs and their derivatives are widely studied in the OER. Metal-functionalized COFs have transition metal atoms, such as Co, Ni, and Fe, which can improve the symmetry and strength of double bonds or triple bonds, and adjust the electronic band gap and electron density. More importantly, active sites such as Co─N, Ni─N, and Fe─N can be formed with N heteroatom, increasing the number of active sites. In addition, the addition of active metals increases the frame stability and electrical conductivity. Compared with single metal COFs, bimetallic COFs have higher OER catalytic activity, which is mainly attributed to the induction of electronic interaction between bimetallic atoms and the enhancement of intrinsic activity of metal sites. To improve the OER catalytic activity of COFs, metal nanoparticles, metal oxides, and transition metal phosphate nanoparticles can be incorporated into the skeleton to prepare COF derivatives. The NPs obtained after calcination are anchored on the carbon skeleton. Adding materials

such as graphene before calcination can not only reduce the degradation and agglomeration of NPs during pyrolysis but also increase the conductivity. Metal nanoparticles can regulate the p-band structure of COFs and weaken the binding strength of O* at active sites, which is more conducive to the OER. Metal oxides and phosphides can promote the redistribution of electron cloud density and expose more active sites, which is beneficial to enhance the catalytic performance of OER. Nonmetal COFs lack active metal sites, and thus there are few studies on nonmetal COFs in the field of OER since the efficiency of free electron transport is low. N-rich macrocyclic conjugated structures (such as triazines) can produce inter-layer π–π interactions, and electron transfer between heteroatoms such as N and C can enhance the electron density at C sites, thereby enhancing the catalytic activity of OER. Similar to OER, ORR requires complex reaction pathways and slow kinetics. Although there is a lack of metal active sites in non-metallic COFs, heteroatom catalytic sites can be formed by the flexible construction of monomers to promote the ORR. The aromatic C═N in the triazine unit can adsorb O_2 through the lateral mode to form a tetracyclic intermediate, and the formation of a thiophene ring significantly promotes the charge transfer efficiency and increase the adsorption capacity of active sites, while unsaturated bonds can optimize the electronic structure and adjust the catalytic reaction kinetics. In addition, doping with heteroatoms is a recognized strategy to introduce catalytic active sites in metal-free COFs. For metalized COFs, the effective active sites in the OER are generally suitable for the ORR. Based on the unique designable topological structure characteristics of COFs, it is possible to modify the active sites in the framework by metallization in the rigid secondary structural units with functional groups, such as metal-based porphyrins, metal-based phthalocyanines, and metalized triazine units. The triazine unit is rich in N atoms and is easy to coordinate with transition metal ions to form a stable structure. Porphyrins have a highly conjugated π-electron structure and excellent conductivity. Metalloporphyrins have a clear crystal structure and open metal active sites, and their structure is conducive to adjusting electronic properties. Phthalocyanine has a special 2D π-electronic structure, and the structure of metal phthalocyanine is adjustable, showing strong chemical stability. Rational use of functionalized structural units for design and development is the key to constructing highly active and selective ORR catalysts. The preparation of N-doped carbon materials by pyrolysis can provide more active sites and promote charge transport. The interaction between metal species and carbon shells provides high ORR catalytic activity and stability. The M─C─N hybrid nanostructures formed by pyrolysis show comparable ORR catalytic activity to Pt-based catalysts due to the formation of M─N_x active sites and the activation of adsorbed O_2. COFs can be combined with MOFs to prepare COFs/MOFs composites with heterojunctions, which complement each other and show stronger catalytic ability than each other. Compared with OER/ORR, there are few studies on COFs in HER. Triazine units and thiophene units in non-metallic COFs are commonly used to prepare HER catalysts. The N in the triazine unit can produce defect sites and has strong corrosion resistance, and the thiophene structure has high conductivity. Transition metals such as Ru, Co, Ni, Mo, and Rh have been reported to have HER catalytic activity. Encapsulating these metal ions in the pores of COFs can form new active sites and enhance intrinsic activity. Another method to

improve HER activity is to combine highly conductive materials with metal-based COFs to prepare heterostructures with highly active interfaces, forming strong electron and interface interactions. Improving the conductivity is the key to improving the HER catalytic activity. Hence, combining COFs with highly conductive carbon materials (such as graphene) and forming heteroatom-doped carbon materials by pyrolysis of COFs are common methods to improve conductivity. Among them, N doping makes the defect sites adsorb oxygen, and P doping defects can enhance the edge effect. COFs used as electrocatalysts for the CO_2RR are mainly metal-functionalized COFs. Metalized COFs containing triazine, porphyrin, phthalocyanine, and pyridine building units have shown important potential in electrocatalytic CO_2RR. The metal in the framework can improve the ability of COFs to adsorb CO_2 and reduce the activation barrier of CO_2, thus greatly improving the electrocatalytic efficiency. In addition to the electrocatalytic activity, the selectivity of the product is also a key factor in judging CO_2RR electrocatalysts. With the help of metal ions, the FE of COFs can reach almost 100%. However, non-metallic COFs are rarely used in electrocatalytic CO_2RR due to the lack of metal sites. Since most CO_2 electroreduction reactions are carried out in liquid-phase systems, the HER has become a competitive reaction, and the development of efficient CO_2RR catalysts requires the necessary adjustment of their reactivity. CO is the most common CO_2RR product, and its reaction path is relatively simple. At present, the FE_{CO} can reach 100%. Metal Cu is currently recognized as a metal that can reduce CO_2 to hydrocarbons and alcohols. In addition to the high selectivity of Cu catalysts, CH_3OH is almost not obtained on Cu-free catalysts. Generally, bimetallic centers are required to catalyze the electroreduction of CO_2 to CH_3OH. The interaction between bimetallic catalysts can reduce the energy barrier of CO_2RR, enhance selectivity, and inhibit competitive HER.

6.2 Prospects

In this paper, we review the application and optimization strategies of COFs and their derivatives in the field of electrocatalysis to accelerate their development. COFs have the advantages of low density, high specific surface area, regular pores, strong modifiability, and high stability, showing immeasurable potential in the field of electrocatalysis. However, at present, the exploration of COFs and their derivatives is still at the initial stage, and there are still many factors limiting the applications of COFs in the field of electrocatalysis.

1) For the framework design of COFs, the 1D framework structure is conducive to the formation of materials with high crystallinity and strong stability. However, due to the anisotropy of the synthesis process and the hindrance of organic unit entropy driving, the formation of a 1D framework structure is difficult. At present, the synthesis technology of 2D frame structure is mature and widely studied. The 2D frame structure produces 1D pores, while the pores in the 3D frame structure are interconnected, which is more conducive to rapid mass transfer. However, the 3D frame structure is still challenging in terms of design and controllability. Therefore, it is needed to design the structure and dimension of COFs reasonably and controllably. In the future, researchers

can explore some substances that can limit the growth direction to control the dimension of COFs. For example, dibenzaldehyde in TPEDH can limit the extension of the framework to 1D.

2) For the pore structure design of COFs, more micropores can increase the specific surface area, while larger mesopores can increase the mass transfer rate. Hence how to design and regulate the pore size according to the required properties and functions is a problem to be solved in the future. In addition, the pore environment is also an important factor affecting the catalytic activity of COF. In recent years, pore surface engineering has gradually entered the public's vision. It is to modify functional groups such as hydroxyl and azide groups on the pore wall to create a specific interface, thereby creating new physical and chemical properties and functions. We hope that in the near future, pore surface engineering can be widely used in the field of electrocatalysis.

3) Because COFs have pre-designability, three preparation methods, pre-modification, in situ modification, and post-modification, are used in the preparation of functionalized COFs. The pre-modified structural units generally have large steric hindrance, which will reduce the crystallinity of COFs. Although in situ modification method is simple to operate, it cannot be applied to most COFs. The post-modification method is the most widely used and more controllable method. However, the post-modification method is easy to break the original pores and structures during the modification process. Therefore, it is feasible and meaningful to prepare functionalized high-performance electrocatalysts by pre-regulating the construction unit, connection type, and topology of COFs.

4) Since ORR involves the adsorption, dissociation, recombination, and desorption processes of various oxygen intermediates at the catalytic sites, including multi-step electron and proton transfer steps, the ORR path and catalytic activity are closely related to the intrinsic site structure of the catalyst. The analysis of ORR active sites is of great significance for the development of efficient catalysts. Whether the ability of the catalyst to bind the intermediate is too strong or too weak will affect the catalytic activity. It is very important to find a catalyst with appropriate binding energy to achieve a compromise between the two extreme processes.

5) At present, CO_2RR still faces many challenges, such as low current density, poor product selectivity, poor stability, high production cost, and unclear reaction mechanisms. As framework materials with precisely adjustable structures, COFs provide an ideal platform for designing excellent CO_2RR electrocatalysts and exploring how these structures affect catalytic performance. However, the application of COFs in CO_2RR is still in the exploratory stage. For a wide variety of COFs, how to give full play to improve the efficiency and selectivity of CO_2RR is an important research direction.

6) At present, structural simulations and theoretical calculations of COFs are not mature, and the research on electrocatalytic mechanisms has not been deeply understood, which leads to the immature theoretical research of COFs in the field of electrocatalysis. The combination of experimental design and theoretical analysis is the key to making people

deeply understand the reaction mechanisms, which is an important part of the future applications of COFs and their derivatives in the field of electrocatalysis.

Acknowledgements

This work was supported by the National Natural Science Foundation of China (No. 22075099), the Natural Science Foundation of Jilin Province (No. 20220101051JC), and the Education Department of Jilin Province (No. JJKH20220968CY).

Conflict of Interest

The authors declare no conflict of interest

Biographies

Liyuan Xiao received her B.S. degree from Qufu Normal University in 2021. She is currently studying at Jilin University as a graduate student, under the guidance of Professor Jingqi Guan and Professor Zhenlu Wang. Her research focuses on the synthesis of metal/covalent organic frameworks for energy conversion and storage.

Zhenlu Wang received his B.S. and Ph.D. degrees from Jilin University in 1994 and 2002, respectively. He was promoted to the position of professor of Chemistry at Jilin University in 2009. He worked as a visiting scholar at the Spanish Institute of Petroleum and Catalysis from 2005 to 2006. His research interests focus on the polymerization and condensation catalysis.

Jingqi Guan is currently a Professor of Chemistry at Jilin University. He received his B.S. and Ph.D. degrees in chemistry from Jilin University. He worked as a postdoctoral research fellow at the University of California at Berkeley from 2012 to 2013 and at the Dalian Institute of Chemical Physics from 2014 to 2018. His research interests are in engineering single-atom catalysts and 2D materials for catalysis, energy, and biosensors. He is on the Editorial Board of Chin. J. Catal., Acta Phys.-Chim. Sin., and EcoEnergy. He has published more than 200 peer-reviewed papers, and the H-index is 44.

References

1 V. Hasija, S. Patial, P. Raizada, A. Aslam Parwaz Khan, A. Asiri, Q. Van Le, V. Nguyen, P. Singh, *Coord. Chem. Rev.* 2022, **452**, 214298.

CAS | Web of Science® | Google Scholar

2 Q. Tran, H. Lee, N. Tran, *Polymers* 2023, **15**, 1279.

CAS | PubMed | Google Scholar

3 a) E. Dautzenberg, G. Li, L. De Smet, *ACS Appl. Mater. Interfaces* 2023, **15**, 5118;

CAS | PubMed | Google Scholar

b) M. Nemiwal, *Mini Rev. Org. Chem.* 2021, **18**, 1026.

CAS | Web of Science® | Google Scholar

4 a) Y. Qian, J. Li, M. Ji, J. Li, D. Ma, A. Liu, Y. Zhao, C. Yang, *Front. Chem.* 2022, **10**, 943813;

CAS | PubMed | Google Scholar

b) X. Ma, J. Kang, Y. Wu, C. Pang, S. Li, J. Li, Y. Xiong, J. Luo, M. Wang, Z. Xu, *TrAC, Trends Anal. Chem.* 2022, **157**, 116793;

CAS | Web of Science® | Google Scholar

c) S. Zhang, D. Liu, G. Wang, *Molecules* 2022, **27**, 2586.

CAS | PubMed | Google Scholar

5 W. Zou, G. Jiang, W. Zhang, L. Zhang, Z. Cui, H. Song, Z. Liang, L. Du, *Adv. Funct. Mater.* 2023, **33**, 2213642.

CAS | Web of Science® | Google Scholar

6 S. Li, B. Kumbhakar, B. Mishra, J. Roeser, N. Chaoui, J. Schmidt, A. Thomas, P. Pachfule, *ACS Appl. Energy Mater.* 2023, **6**, 9256.

CAS | Web of Science® | Google Scholar

7 a) C. Wu, Z. Xing, S. Yang, Z. Li, W. Zhou, *Coord. Chem. Rev.* 2023, **477**, 214939;

CAS | Web of Science® | Google Scholar

b) Y. Wang, Y. Zhao, Z. Li, *Macromol. Rapid Commun.* 2022, **43**, 2200108;

CAS | Web of Science® | Google Scholar

c) L. Guo, W. Chen, Y. Li, Z. Wei, F. Li, C. Li, *Mater. Chem. Phys.* 2023, **301**, 127645.

CAS | Google Scholar

8 a) J. Jia, J. Li, S. Ma, Z. Zhang, X. Liu, *Macromol. Rapid Commun.* 2022;

Google Scholar

b) X. Liu, L. Feng, Y. Li, T. Xia, Z. Sui, Q. Chen, *Molecules* 2022, **27**, 5193.

CAS | PubMed | Google Scholar

9 P. Phan, Q. Ta, P. Nguyen, *Polymers* 2023, **15**, 887.

CAS | PubMed | Google Scholar

10 S. Patial, V. Soni, A. Kumar, P. Raizada, T. Ahamad, X. Pham, Q. Le, V. Nguyen, S. Thakur, P. Singh, *Environ. Res.* 2023, **218**, 114982.

CAS | PubMed | Google Scholar

11 J. Lee, *Nat. Rev. Mater.* 2023, **8**, 495.

Web of Science® | Google Scholar

12 P. Phan, Q. Ta, P. Nguyen, 2023, **15**, 887.

Google Scholar

13 T. He, Y. Zhao, *Angew. Chem., Int. Ed.* 2023, **62**, e202303086.

CAS | PubMed | Web of Science® | Google Scholar

14 a) Y. Li, W. Chen, G. Xing, D. Jiang, L. Chen, *Chem. Soc. Rev.* 2020, **49**, 2852;

CAS | PubMed | Web of Science® | Google Scholar

b) L. Li, Y. Ma, H. Yang, N. Wu, L. Peng, J. Wang, *ACS Applied Polymer Materials* 2023, **5**, 784;

CAS | Web of Science® | Google Scholar

c) Q. Ma, X. Liu, J. Qian, Q. Zhuang, *Sep. Purif. Technol.* 2023, **323**, 124368;

CAS | Google Scholar

d) Y. Sun, B. Zhang, C. Zhang, H. Lu, Y. Yang, B. Han, F. Dong, J. Lv, S. Zhang, Z. Li, Z. Lei, H. Ma, *ACS Appl. Mater. Interfaces* 2023, **15**, 4569.

CAS | PubMed | Web of Science® | Google Scholar

15 Y. Liu, H. Wu, Q. Wang, *J. Mater. Chem. A* 2023, **11**, 21470.

CAS | Web of Science® | Google Scholar

16 a) T. He, Z. Zhao, R. Liu, X. Liu, B. Ni, Y. Wei, Y. Wu, W. Yuan, H. Peng, Z. Jiang, Y. Zhao, *J. Am. Chem. Soc.* 2023, **145**, 6057;

CAS | PubMed | Web of Science® | Google Scholar

b) J. Ding, X. Guan, J. Lv, X. Chen, Y. Zhang, H. Li, D. Zhang, S. Qiu, H. Jiang, Q. Fang, *J. Am. Chem. Soc.* 2023, **145**, 3248.

CAS | PubMed | Web of Science® | Google Scholar

17 S. Huang, K. Chen, T. Li, *Coord. Chem. Rev.* 2022, **464**, 214563.

CAS | Web of Science® | Google Scholar

18 Z. Zhao, X. Chen, B. Li, S. Zhao, L. Niu, Z. Zhang, Y. Chen, *Adv. Sci.* 2022, **9**, 2203832.

CAS | Google Scholar

19 A. Côté, A. Benin, N. Ockwig, M. O'Keeffe, A. Matzger, O. Yaghi, *Science* 2005, **310**, 1166.

CAS | PubMed | Web of Science® | Google Scholar

20 H. El-Kaderi, J. Hunt, J. Mendoza-Cortés, A. Côté, R. Taylor, M. O'Keeffe, O. Yaghi, *Science* 2007, **316**, 268.

CAS | PubMed | Web of Science® | Google Scholar

21 P. Kuhn, M. Antonietti, A. Thomas, *Angew. Chem., Int. Ed.* 2008, **47**, 3450.

CAS | PubMed | Web of Science® | Google Scholar

22 S. Ding, J. Gao, Q. Wang, Y. Zhang, W. Song, C. Su, W. Wang, *J. Am. Chem. Soc.* 2011, **133**, 19816.

CAS | PubMed | Web of Science® | Google Scholar

23 N. Huang, L. Zhai, D. Coupry, M. Addicoat, K. Okushita, K. Nishimura, T. Heine, D. Jiang, *Nat. Commun.* 2016, **7**, 12325.

PubMed | Web of Science® | Google Scholar

24 R. Liang, S. Xu, L. Zhang, R. A., P. Chen, F. Cui, Q. Qi, J. Sun, X. Zhao, *Nat. Commun.* 2019, **10**, 4609.

PubMed | Web of Science® | Google Scholar

25 Z. Mu, Y. Zhu, B. Li, A. Dong, B. Wang, X. Feng, *J. Am. Chem. Soc.* 2022, **144**, 5145.

CAS | PubMed | Web of Science® | Google Scholar

26 W. Zhang, L. Chen, S. Dai, C. Zhao, C. Ma, L. Wei, M. Zhu, S. Chong, H. Yang, L. Liu, Y. Bai, M. Yu, Y. Xu, X. Zhu, Q. Zhu, S. An, R. Sprick, M. Little, X. Wu, S. Jiang, Y. Wu, Y. Zhang, H. Tian, W. Zhu, A. Cooper, *Nature* 2022, **604**, 72.

CAS | PubMed | Web of Science® | Google Scholar

27 Y. Yin, Y. Zhang, X. Zhou, B. Gui, G. Cai, J. Sun, C. Wang, *J. Am. Chem. Soc.* 2023, **145**, 22329.

CAS | PubMed | Web of Science® | Google Scholar

28 a) J. Han, X. Niu, J. Guan, *J. Colloid Interface Sci.* 2023, **635**, 167;

CAS | PubMed | Web of Science® | Google Scholar

b) T. Tang, S. Jiao, J. Han, Z. Wang, J. Guan, *Int. J. Hydrogen Energy* 2023, **48**, 5774;

CAS | Web of Science® | Google Scholar

c) T. Tang, Z. Duan, D. Baimanov, X. Bai, X. Liu, L. Wang, Z. Wang, J. Guan, *Nano Res.* 2022, **16**, 2218.

Web of Science® | Google Scholar

---

29 a) T. Tang, Z. Wang, J. Guan, *Chin. J. Catal.* 2022, **43**, 636;

CAS | Web of Science® | Google Scholar

b) T. Gao, K. Kumar, Z. Yan, M. Marinova, M. Trentesaux, M. Amin, S. Szunerits, Y. Zhou, V. Martin-Diaconescu, S. Paul, R. Boukherroub, V. Ordomsky, *J. Mater. Chem. A* 2023, **11**, 19338.

CAS | Web of Science® | Google Scholar

---

30 a) T. Tang, Y. Wang, J. Han, Q. Zhang, X. Bai, X. Niu, Z. Wang, J. Guan, *Chin. J. Catal.* 2023, **46**, 48;

CAS | Web of Science® | Google Scholar

b) S. Chang, C. Li, H. Li, L. Zhu, Q. Fang, *Chem. Res. Chin. Univ.* 2022, **38**, 396.

CAS | Web of Science® | Google Scholar

---

31 a) T. Tang, Z. Wang, J. Guan, *Adv. Funct. Mater.* 2022, **32**, 2111504;

CAS | Web of Science® | Google Scholar

b) Q. Miao, C. Lu, Q. Xu, S. Yang, M. Liu, S. Liu, C. Yu, X. Zhuang, Z. Jiang, G. Zeng, *Chem. Eng. J.* 2022, **450**, 138427;

CAS | Google Scholar

c) M. Liu, S. Yang, X. Yang, C. Cui, G. Liu, X. Li, J. He, G. Chen, Q. Xu, G. Zeng, *Nat. Commun.* 2023, **14**, 3800.

CAS | PubMed | Web of Science® | Google Scholar

---

32 S. Mondal, B. Mohanty, M. Nurhuda, S. Dalapati, R. Jana, M. Addicoat, A. Datta, B. Jena, A. Bhaumik, *ACS Catal.* 2020, **10**, 5623.

CAS | Web of Science® | Google Scholar

---

33 X. Zhao, P. Pachfule, S. Li, T. Langenhahn, M. Ye, C. Schlesiger, S. Praetz, J. Schmidt, A. Thomas, *J. Am. Chem. Soc.* 2019, **141**, 6623.

CAS | PubMed | Web of Science® | Google Scholar

34 C. Lin, L. Zhang, Z. Zhao, Z. Xia, *Adv. Mater.* 2017, **29**, 1606635.

CAS | Web of Science® | Google Scholar

35 J. Han, J. Guan, *Nano Res.* 2022, **16**, 1913.

Web of Science® | Google Scholar

36 S. Lin, C. Diercks, Y. Zhang, N. Kornienko, E. Nichols, Y. Zhao, A. Paris, D. Kim, P. Yang, O. Yaghi, C. Chang, *Science* 2015, **349**, 1208.

CAS | PubMed | Web of Science® | Google Scholar

37 Y. Lu, J. Zhang, W. Wei, D. Ma, X. Wu, Q. Zhu, *ACS Appl. Mater. Interfaces* 2020, **12**, 37986.

CAS | PubMed | Web of Science® | Google Scholar

38 L. Gong, D. Zhang, Y. Shen, X. Wang, J. Zhang, X. Han, L. Zhang, Z. Xia, *J. Catal.* 2020, **390**, 126.

CAS | Web of Science® | Google Scholar

39 H. Liu, J. Chu, Z. Yin, X. Cai, L. Zhuang, H. Deng, *Chem* 2018, **4**, 1696.

CAS | Web of Science® | Google Scholar

40 a) J. Tang, C. Su, Z. Shao, *Small Methods* 2021, **5**, 2100945;

CAS | PubMed | Web of Science® | Google Scholar

b) X. Cui, S. Lei, A. Wang, L. Gao, Q. Zhang, Y. Yang, Z. Lin, *Nano Energy* 2020, **70**, 104525.

CAS | Web of Science® | Google Scholar

41 J. Guo, Y. Xu, S. Jin, L. Chen, T. Kaji, Y. Honsho, M. Addicoat, J. Kim, A. Saeki, H. Ihee, S. Seki, S. Irle, M. Hiramoto, J. Gao, D. Jiang, *Nat. Commun.* 2013, **4**, 2736.

PubMed | Web of Science® | Google Scholar

42 J. Mahmood, E. Lee, M. Jung, D. Shin, I. Jeon, S. Jung, J. Choi, J. Seo, S. Bae, S. Sohn, N. Park, J. Oh, H. Shin, J. Baek, *Nat. Commun.* 2015, **6**, 6286.

PubMed | Google Scholar

43 J. Shi, R. Chen, H. Hao, C. Wang, X. Lang, *Angew. Chem. Int. Ed. Engl.* 2020, **59**, 9088.

CAS | PubMed | Web of Science® | Google Scholar

44 M. Zhang, D. Si, J. Yi, S. Zhao, Y. Huang, R. Cao, *Small* 2020, **16**, 2005254.

CAS | PubMed | Web of Science® | Google Scholar

45 Z. Pang, T. Zhou, R. Liang, Q. Qi, X. Zhao, *Chem. Sci.* 2017, **8**, 3866.

CAS | PubMed | Web of Science® | Google Scholar

46 P. Wang, X. Chen, Q. Jiang, M. Addicoat, N. Huang, S. Dalapati, T. Heine, F. Huo, D. Jiang, *Angew. Chem., Int. Ed.* 2019, **58**, 15922.

CAS | PubMed | Web of Science® | Google Scholar

47 H. El-Kaderi, J. Hunt, J. Mendoza-Corte, A. Côté, R. Taylor, M. O'Keeffe, O. Yaghi, *Science* 2007, **316**, 268.

CAS | PubMed | Web of Science® | Google Scholar

48 F. Uribe-Romo, J. Hunt, H. Furukawa, C. Klöck, M. O'Keeffe, O. Yaghi, *J. Am. Chem. Soc.* 2009, **131**, 4570.

CAS | PubMed | Web of Science® | Google Scholar

49 G. Lin, H. Ding, R. Chen, Z. Peng, B. Wang, C. Wang, *J. Am. Chem. Soc.* 2017, **139**, 8705.

CAS | PubMed | Web of Science® | Google Scholar

50 Y. Zhang, J. Duan, D. Ma, P. Li, S. Li, H. Li, J. Zhou, X. Ma, X. Feng, B. Wang, *Angew. Chem., Int. Ed.* 2017, **56**, 16313.

CAS | PubMed | Web of Science® | Google Scholar

51 O. Yahiaoui, A. Fitch, F. Hoffmann, M. Fröba, A. Thomas, J. Roeser, *J. Am. Chem. Soc.* 2018, **140**, 5330.

CAS | PubMed | Web of Science® | Google Scholar

52 X. Kang, X. Wu, X. Han, C. Yuan, Y. Liu, Y. Cui, *Chem. Sci.* 2020, **11**, 1494.

CAS | Web of Science® | Google Scholar

53 T. Ma, E. Kapustin, S. Yin, L. Liang, Z. Zhou, J. Niu, L. Li, Y. Wang, J. Su, J. Li, X. Wang, W. Wang, W. Wang, J. Sun, O. Yaghi, *Science* 2018, **361**, 48.

CAS | PubMed | Web of Science® | Google Scholar

54 Y. Wang, C. Wu, W. Sun, Q. Pan, W. Hao, H. Liu, J. Sun, Z. Li, J. Sun, Y. Zhao, *Mater. Chem. Front.* 2021, **5**, 944.

CAS | Web of Science® | Google Scholar

55 H. Li, F. Chen, X. Guan, J. Li, C. Li, B. Tang, V. Valtchev, Y. Yan, S. Qiu, Q. Fang, *J. Am. Chem. Soc.* 2021, **143**, 2654.

CAS | PubMed | Web of Science® | Google Scholar

56 X. Kang, X. Han, C. Yuan, C. Cheng, Y. Liu, Y. Cui, *J. Am. Chem. Soc.* 2020, **142**, 16346.

CAS | PubMed | Web of Science® | Google Scholar

57 C. Gropp, T. Ma, N. Hanikel, O. Yaghi, *Science* 2020, **370**, 424.

Web of Science® | Google Scholar

58 H. Nguyen, C. Gropp, Y. Ma, C. Zhu, O. Yaghi, *J. Am. Chem. Soc.* 2020, **142**, 20335.

CAS | Web of Science® | Google Scholar

59 Z. Li, L. Sheng, H. Wang, X. Wang, M. Li, Y. Xu, H. Cui, H. Zhang, H. Liang, H. Xu, X. He, *J. Am. Chem. Soc.* 2021, **143**, 92.

CAS | PubMed | Web of Science® | Google Scholar

60 Y. Liu, C. Wu, Q. Sun, F. Hu, Q. Pan, J. Sun, Y. Jin, Z. Li, W. Zhang, Y. Zhao, *CCS Chemistry* 2021, **3**, 2418.

CAS | Google Scholar

61 S. Wang, L. Da, J. Hao, J. Li, M. Wang, Y. Huang, Z. Li, Z. Liu, D. Cao, *Angew. Chem., Int. Ed.* 2021, **60**, 9321.

CAS | PubMed | Web of Science® | Google Scholar

62 Y. Wang, Y. Liu, H. Li, X. Guan, M. Xue, Y. Yan, V. Valtchev, S. Qiu, Q. Fang, *J. Am. Chem. Soc.* 2020, **142**, 3736.

CAS | PubMed | Web of Science® | Google Scholar

63 Y. Meng, Y. Luo, J. Shi, H. Ding, X. Lang, W. Chen, A. Zheng, J. Sun, C. Wang, *Angew. Chem., Int. Ed.* 2020, **59**, 3624.

CAS | PubMed | Web of Science® | Google Scholar

64 B. Gui, X. Liu, Y. Cheng, Y. Zhang, P. Chen, M. He, J. Sun, C. Wang, *Angew. Chem., Int. Ed.* 2022, **61**, 1907289.

Google Scholar

65 H. Li, J. Ding, X. Guan, F. Chen, C. Li, L. Zhu, M. Xue, D. Yuan, V. Valtchev, Y. Yan, S. Qiu, Q. Fang, *J. Am. Chem. Soc.* 2020, **142**, 13334.

CAS | PubMed | Web of Science® | Google Scholar

66 Q. Zhu, X. Wang, R. Clowes, P. Cui, L. Chen, M. Little, A. Cooper, *J. Am. Chem. Soc.* 2020, **142**, 16842.

CAS | PubMed | Web of Science® | Google Scholar

67 X. Guan, F. Chen, Q. Fang, S. Qiu, *Chem. Soc. Rev.* 2020, **49**, 1357.

CAS | PubMed | Web of Science® | Google Scholar

68 S. Park, Z. Liao, B. Ibarlucea, H. Qi, H. H. Lin, D. Becker, J. Melidonie, T. Zhang, H. Sahabudeen, L. Baraban, C. Baek, Z. Zheng, E. Zschech, A. Fery, T. Heine, U. Kaiser, G. Cuniberti, R. Dong, X. Feng, *Angew. Chem., Int. Ed.* 2020, **59**, 8218.

CAS | PubMed | Web of Science® | Google Scholar

69 J. Chen, Q. Zheng, S. Xiao, L. Zhang, R. Liang, G. Ouyang, J. Qiu, *Anal. Chem.* 2022, **94**, 2517.

CAS | PubMed | Web of Science® | Google Scholar

70 X. Guo, T. Mao, Z. Wang, P. Cheng, Y. Chen, S. Ma, Z. Zhang, *ACS Cent. Sci.* 2020, **6**, 787.

CAS | PubMed | Web of Science® | Google Scholar

71 C. Zhao, C S. Diercks, C. Zhu, N. Hanikel, X. Pei, O M. Yaghi, *J. Am. Chem. Soc.* 2018, **140**, 16438.

CAS | PubMed | Web of Science® | Google Scholar

72 G. Kim, J. Yang, N. Nakashima, T. Shiraki, *Chem. – Eur. J.* 2017, **23**, 17504.

CAS | PubMed | Web of Science® | Google Scholar

73 S. Kandambeth, K. Dey, R. Banerjee, *J. Am. Chem. Soc.* 2019, **141**, 1807.

CAS | PubMed | Web of Science® | Google Scholar

74 T. Wang, R. Xue, H. Chen, P. Shi, X. Lei, Y. Wei, H. Guo, W. Yang, *New J. Chem.* 2017, **41**, 14272.

CAS | Web of Science® | Google Scholar

75 R. Van Der Jagt, A. Vasileiadis, H. Veldhuizen, P. Shao, X. Feng, S. Ganapathy, N. Habisreutinger, M. Van Der Veen, C. Wang, M. Wagemaker, S. Van Der Zwaag, A. Nagai, *Chem. Mater.* 2021, **33**, 818.

CAS | PubMed | Web of Science® | Google Scholar

76 S. Kim, H. Jung, M. Okyay, H. Noh, S. Chung, Y. Kim, J. Jeon, B. Wong, K. Cho, J. Seo, J. Yoo, J. Baek, *Angew. Chem., Int. Ed.* 2023, **62**, e202310560.

CAS | PubMed | Google Scholar

77 Z. Lei, F. Lucas, E. Canales Moya, S. Huang, Y. Rong, A. Wesche, P. Li, L. Bodkin, Y. Jin, A. Holewinski, W. Zhang, *Chin. Chem. Lett.* 2021, **32**, 3799.

CAS | Web of Science® | Google Scholar

78 C. Yang, Z. Yang, H. Dong, N. Sun, Y. Lu, F. Zhang, G. Zhang, *ACS Energy Lett.* 2019, **4**, 2251.

CAS | Web of Science® | Google Scholar

79 Y. Yang, X. Chu, H. Zhang, R. Zhang, Y. Liu, F. Zhang, M. Lu, Z. Yang, Y. Lan, *Nat. Commun.* 2023, **14**, 593.

CAS | PubMed | Web of Science® | Google Scholar

80 E. Jin, M. Asada, Q. Xu, S. Dalapati, M. Addicoat, M. Brady, H. Xu, T. Nakamura, T. Heine, Q. Chen, D. Jiang, *Science* 2017, **357**, 673.

CAS | PubMed | Web of Science® | Google Scholar

81 S. Lyle, T. Osborn Popp, P. Waller, X. Pei, J. Reimer, O. Yaghi, *J. Am. Chem. Soc.* 2019, **141**, 11253.

CAS | PubMed | Web of Science® | Google Scholar

82 C. Zhao, H. Lyu, Z. Ji, C. Zhu, O. Yaghi, *J. Am. Chem. Soc.* 2020, **142**, 14450.

CAS | PubMed | Web of Science® | Google Scholar

83 Z. Zhou, P. Tian, J. Yao, Y. Lu, Q. Qi, X. Zhao, *Nat. Commun.* 2022, **13**, 2180.

CAS | PubMed | Web of Science® | Google Scholar

84 H. Qian, M. Zhu, M. Du, X. Ran, X. Yan, *J. Hazard. Mater.* 2022, **427**, 128156.

CAS | PubMed | Google Scholar

85 Z. Yang, J. Liu, Y. Li, G. Zhang, G. Xing, L. Chen, *Angew. Chem., Int. Ed.* 2021, **60**, 20754.

CAS | PubMed | Web of Science® | Google Scholar

86 X. Li, J. Zou, T. Wang, H. Ma, G. Chen, Y. Dong, *J. Am. Chem. Soc.* 2020, **142**, 6521.

CAS | PubMed | Web of Science® | Google Scholar

87 J. Liu, T. Yang, Z. Wang, P. Wang, J. Feng, S. Ding, W. Wang, *J. Am. Chem. Soc.* 2020, **142**, 20956.

CAS | PubMed | Web of Science® | Google Scholar

88 L. Peng, J. Sun, J. Huang, C. Song, Q. Wang, L. Wang, H. Yan, M. Ji, D. Wei, Y. Liu, D. Wei, *Chem. Mater.* 2022, **34**, 2886.

CAS | Web of Science® | Google Scholar

89 B. Patra, S. Bhattacharya, *Chem. Mater.* 2021, **33**, 8512.

CAS | Web of Science® | Google Scholar

90 S. Liu, Q. Su, W. Qi, K. Luo, X. Sun, H. Ren, Q. Wu, *Catal. Sci. Technol.* 2022, **12**, 2837.

CAS | Web of Science® | Google Scholar

91 X. Guan, Y. Ma, H. Li, Y. Yusran, M. Xue, Q. Fang, Y. Yan, V. Valtchev, S. Qiu, *J. Am. Chem. Soc.* 2018, **140**, 4494.

CAS | PubMed | Web of Science® | Google Scholar

92 S. Gao, Z. Li, Y. Yang, Z. Wang, Y. Wang, S. Luo, K. Yao, J. Qiu, H. Wang, L. Cao, Z. Lai, J. Wang, *ACS Appl. Mater. Interfaces* 2021, **13**, 36507.

CAS | PubMed | Web of Science® | Google Scholar

93 W. Ji, Y. Guo, H. Xie, X. Wang, X. Jiang, D. Guo, *J. Hazard. Mater.* 2020, **397**, 122793.

CAS | PubMed | Web of Science® | Google Scholar

94 L. Zhao, L. Zheng, X. Li, H. Wang, L. Lv, S. Chen, W. Sun, Y. Wang, *ACS Appl. Mater. Interfaces* 2021, **13**, 48913.

CAS | PubMed | Web of Science® | Google Scholar

95 B. Biswal, S. Chandra, S. Kandambeth, B. Lukose, T. Heine, R. Banerjee, *J. Am. Chem. Soc.* 2013, **135**, 5328.

CAS | PubMed | Web of Science® | Google Scholar

96 G. Das, D. Balaji Shinde, S. Kandambeth, B. Biswal, R. Banerjee, *Chem. Commun. (Camb.)* 2014, **50**, 12615.

CAS | PubMed | Web of Science® | Google Scholar

97 H. Lv, X. Zhao, H. Niu, S. He, Z. Tang, F. Wu, J. Giesy, *J. Hazard. Mater.* 2019, **369**, 494.

CAS | PubMed | Web of Science® | Google Scholar

98 X. Shi, D. Ma, F. Xu, Z. Zhang, Y. Wang, *Chem. Sci.* 2020, **11**, 989.

CAS | Web of Science® | Google Scholar

99 S. Wang, L. Yang, K. Xu, H. Chen, N. Huang, *ACS Appl. Mater. Interfaces* 2021, **13**, 44806.

CAS | PubMed | Web of Science® | Google Scholar

100 W. Zhao, P. Yan, H. Yang, M. Bahri, A. James, H. Chen, L. Liu, B. Li, Z. Pang, R. Clowes, N. Browning, J. Ward, Y. Wu, A. Cooper, *Nature Synthesis* 2022, **1**, 87.

Google Scholar

101 K. Duan, J. Wang, Y. Zhang, J. Liu, *J. Membr. Sci.* 2019, **572**, 588.

CAS | Web of Science® | Google Scholar

102 C. Gong, X. Yang, X. Wei, F. Dai, T. Zhang, D. Wang, M. Li, J. Jia, Y. She, G. Xu, Y. Peng, *Mater. Chem. Front.* 2023, **7**, 230.

CAS | Web of Science® | Google Scholar

103 W. Zhou, L. Yang, X. Wang, W. Zhao, J. Yang, D. Zhai, L. Sun, W. Deng, *JACS Au* 2021, **1**, 1497.

CAS | PubMed | Google Scholar

104 V. Rajagopal, M. Manivannan, M. Kathiresan, V. Suryanarayanan, L. Jones, *Mater. Chem. Phys.* 2022, **285**, 126104.

CAS | Google Scholar

105 N. Sinha, S. Pakhira, *ACS Appl. Electron. Mater.* 2021, **3**, 720.

CAS | Google Scholar

106 Y. Zhou, L. Chen, L. Sheng, Q. Luo, W. Zhang, J. Yang, *Nano Res.* 2022.

Google Scholar

107 W. Li, J. Wang, C. Jia, J. Chen, Z. Wen, A. Huang, *J. Colloid Interface Sci.* 2023, **650**, 275.

CAS | PubMed | Web of Science® | Google Scholar

108 X. Zhu, N. He, J. Ding, R. Yue, S. He, W. Liu, N. Liu, R. Guo, Z. Mo, *J. Alloys Compd.* 2022, **924**, 166442.

CAS | Web of Science® | Google Scholar

109 X. Wang, L. Sun, W. Zhou, L. Yang, G. Ren, H. Wu, W. Deng, *Cell Rep. Phys. Sci.* 2022, **3**, 100804.

CAS | Google Scholar

110 T. Li, C. Atish, K. Silambarasan, X. Liu, A. O'mullane, *Electrochim. Acta* 2020, **362**, 137212.

CAS | Web of Science® | Google Scholar

111 X. Zhao, P. Pachfule, S. Li, T. Langenhahn, M. Ye, C. Schlesiger, S. Praetz, J. Schmidt, A. Thomas, *J. Am. Chem. Soc.* 2019, **141**, 6623.

CAS | PubMed | Web of Science® | Google Scholar

112 J. Park, C. Lee, J. Ju, J. Lee, J. Seol, S. Lee, J. Kim, *Adv. Funct. Mater.* 2021, **31**, 2101727.

CAS | Web of Science® | Google Scholar

113 J. Ju, C. Lee, J. Park, J. Lee, H. Lee, J. Shin, S. Kwak, S. Lee, J. Kim, *ACS Appl. Mater. Interfaces* 2022, **14**, 24404.

CAS | PubMed | Web of Science® | Google Scholar

114 Y. Zhao, Y. Yang, T. Xia, H. Tian, Y. Li, Z. Sui, N. Yuan, X. Tian, Q. Chen, *ChemSusChem* 2021, **14**, 4556.

CAS | PubMed | Web of Science® | Google Scholar

115 Q. Ma, R. Liao, Y. Lu, S. Liu, Y. Tang, Y. Zhu, D. Wu, *Chem. – Asian J.* 2021, **16**, 3102.

CAS | PubMed | Web of Science® | Google Scholar

116 A. Wang, L. Cheng, W. Zhao, X. Shen, W. Zhu, *J. Colloid Interface Sci.* 2020, **579**, 598.

CAS | PubMed | Web of Science® | Google Scholar

117 X. Ye, J. Fan, Y. Min, P. Shi, Q. Xu, *Nanoscale* 2021, **13**, 14854.

CAS | PubMed | Web of Science® | Google Scholar

118 Q. Shao, Y. Li, X. Cui, T. Li, H. Wang, Y. Li, Q. Duan, Z. Si, *ACS Sustainable Chem. Eng.* 2020, **8**, 6422.

CAS | Web of Science® | Google Scholar

119 Y. Liu, X. Yan, T. Li, W. Zhang, Q. Fu, H. Lu, X. Wang, Z. Gu, *New J. Chem.* 2019, **43**, 16907.

CAS | Web of Science® | Google Scholar

120 D. Huang, Q. Wang, W. Dong, L. Liao, H. Chen, J. Ye, *Energy Fuels* 2022, **36**, 11601.

CAS | Google Scholar

121 X. Wang, L. Sun, W. Zhou, L. Yang, G. Ren, H. Wu, W. Deng, *Cell Rep. Phys. Sci.* 2022, **3**, 100804.

CAS | Google Scholar

122 Z. Gao, L. Gong, X. He, X. Su, L. Xiao, F. Luo, *Inorg. Chem.* 2020, **59**, 4995.

CAS | PubMed | Web of Science® | Google Scholar

123 D. Wu, Q. Xu, J. Qian, X. Li, Y. Sun, *Chem. – Eur. J.* 2019, **25**, 3105.

CAS | PubMed | Web of Science® | Google Scholar

124 W. Zhou, L. Yang, F. Zhou, Q. Deng, X. Wang, D. Zhai, G. Ren, K. Han, W. Deng, L. Sun, *Chem. – Eur. J.* 2020, **26**, 7720.

CAS | PubMed | Web of Science® | Google Scholar

125 M. Wang, C. Wang, J. Liu, F. Rong, L. He, Y. Lou, Z. Zhang, M. Du, *ACS Sustainable Chem. Eng.* 2021, **9**, 5872.

CAS | Web of Science® | Google Scholar

126 J. Chang, G. Xu, H. Li, Q. Fang, *Chem. J. Chinese U.* 2020, **41**, 1609.

CAS | Google Scholar

127 H. Jena, C. Krishnaraj, S. Parwaiz, F. Lecoeuvre, J. Schmidt, D. Pradhan, P. Van Der Voort, *ACS Appl. Mater. Interfaces* 2020, **12**, 44689.

CAS | PubMed | Web of Science® | Google Scholar

128 B. Ball, C. Chakravarty, P. Sarkar, *J. Phys. Chem. Lett.* 2020, **11**, 1542.

CAS | PubMed | Web of Science® | Google Scholar

129 Y. Ma, Y. Fu, W. Jiang, Y. Wu, C. Liu, G. Che, Q. Fang, *J. Mater. Chem. A* 2022, **10**, 10092.

CAS | Web of Science® | Google Scholar

130 Y. Zhao, Y. Liang, D. Wu, H. Tian, T. Xia, W. Wang, W. Xie, X. Hu, X. Tian, Q. Chen, *Small* 2022, **18**, 2107750.

CAS | Web of Science® | Google Scholar

131 Q. Wang, A. Wang, Y. Dou, X. Shen, M. Sudi, L. Zhao, W. Zhu, L. Li, *Chem. Commun.* 2022, **58**, 7423.

CAS | PubMed | Web of Science® | Google Scholar

132 B. Zhang, L. Chen, Z. Zhang, Q. Li, P. Khangale, D. Hildebrandt, X. Liu, Q. Feng, S. Qiao, *Adv. Sci.* 2022, **9**, 2105912.

CAS | Google Scholar

133 Q. Zhao, S. Chen, H. Ren, C. Chen, W. Yang, *Ind. Eng. Chem. Res.* 2021, **60**, 11070.

CAS | Web of Science® | Google Scholar

134 S. Sun, G. Wang, Y. Zhou, F. Wang, X. Xia, *ACS Appl. Mater. Interfaces* 2019, **11**, 19176.

CAS | PubMed | Web of Science® | Google Scholar

135 S. Maiti, A. Chowdhury, A. Das, *ChemNanoMat* 2020, **6**, 99.

CAS | Web of Science® | Google Scholar

136 V. Rajagopal, M. Manivannan, M. Kathiresan, V. Suryanarayanan, L. Jones, *Mater. Chem. Phys.* 2022, **285**, 126104.

CAS | Google Scholar

137 J. Yue, X. Ding, L. Song, Y. Wang, P. Yang, Y. Ma, B. Tang, *Microporous Mesoporous Mater.* 2022, **344**, 112169.

CAS | Google Scholar

138 S. Ruidas, B. Mohanty, P. Bhanja, E. Erakulan, R. Thapa, P. Das, A. Chowdhury, S. Mandal, B. Jena, A. Bhaumik, *ChemSusChem* 2021, **14**, 5057.

CAS | PubMed | Web of Science® | Google Scholar

139 R. Pan, J. Wu, W. Wang, C. Cheng, X. Liu, *Colloids Surf., A* 2021, **621**, 126511.

CAS | Google Scholar

140 M. Liu, Q. Xu, Q. Miao, S. Yang, P. Wu, G. Liu, J. He, C. Yu, G. Zeng, *J. Mater. Chem. A* 2022, **10**, 228.

Web of Science® | Google Scholar

141 S. Yuan, L. Cui, X. He, W. Zhang, T. Asefa, *Int. J. Hydrogen Energy* 2020, **45**, 28860.

CAS | Web of Science® | Google Scholar

142 B. Zhang, L. Chen, Z. Zhang, Q. Li, P. Khangale, D. Hildebrandt, X. Liu, Q. Feng, S. Qiao, *Adv. Sci.* 2022, **9**, 2105912.

CAS | Google Scholar

143 S. Bhunia, S. Das, R. Jana, S. Peter, S. Bhattacharya, M. Addicoat, A. Bhaumik, A. Pradhan, *ACS Appl. Mater. Interfaces* 2017, **9**, 23843.

CAS | PubMed | Web of Science® | Google Scholar

144 X. Fan, F. Kong, A. Kong, A. Chen, Z. Zhou, Y. Shan, *ACS Appl. Mater. Interfaces* 2017, **9**, 32840.

CAS | PubMed | Web of Science® | Google Scholar

145 J. Yi, R. Xu, G. Chai, T. Zhang, K. Zang, B. Nan, H. Lin, Y. Liang, J. Lv, J. Luo, R. Si, Y. Huang, R. Cao, *J. Mater. Chem. A* 2019, **7**, 1252.

CAS | Web of Science® | Google Scholar

146 G. Xu, H. Lei, G. Zhou, C. Zhang, L. Xie, W. Zhang, R. Cao, *Chem. Commun.* 2019, **55**, 12647.

CAS | PubMed | Web of Science® | Google Scholar

147 S. Qiao, B. Zhang, Q. Li, Z. Li, W. Wang, J. Zhao, X. Zhang, Y. Hu, *ChemSusChem* 2019, **12**, 5032.

CAS | PubMed | Web of Science® | Google Scholar

148 a) J. Nørskov, J. Rossmeisl, A. Logadottir, L. Lindqvist, J. R. Kitchin, T. Bligaard, H. Jónsson, *J. Phys. Chem. B* 2004, **108**, 17886;

CAS | Web of Science® | Google Scholar

b) I. Stephens, A. Bondarenko, U. Grønbjerg, J. Rossmeisl, I. Chorkendorff, *Energy Environ. Sci.* 2012, **5**, 6744.

CAS | Web of Science® | Google Scholar

149 Z. Xiang, D. Cao, L. Huang, J. Shui, M. Wang, L. Dai, *Adv. Mater.* 2014, **26**, 3315.

CAS | PubMed | Web of Science® | Google Scholar

150 T. Boruah, S. Das, G. Kumar, S. Mondal, R. Dey, *Chem. Commun.* 2022, **58**, 5506.

CAS | PubMed | Web of Science® | Google Scholar

151 R. Bao, Z. Xiang, Z. Qiao, Y. Yang, Y. Zhang, D. Cao, S. Wang, *Angew. Chem., Int. Ed. Engl.* 2022, **62**, 202216751.

PubMed | Google Scholar

152 X. Yan, B. Wang, J. Ren, X. Long, D. Yang, *Angew. Chem., Int. Ed.* 2022, **61**, 202209583.

CAS | PubMed | Web of Science® | Google Scholar

153 J. Yue, Y. Wang, X. Wu, P. Yang, Y. Ma, X. Liu, B. Tang, *Chem. Commun.* 2021, **57**, 12619.

CAS | PubMed | Web of Science® | Google Scholar

154 Z. Zhang, W. Wang, X. Wang, L. Zhang, C. Cheng, X. Liu, *Chem. Eng. J.* 2022, **435**, 133872.

CAS | Web of Science® | Google Scholar

155 C. Tang, Q. Zhang, *Adv. Mater.* 2017, **29**, 1604103.

CAS | Web of Science® | Google Scholar

156 T. Jiang, W. Jiang, Y. Li, Y. Xu, M. Zhao, M. Deng, Y. Wang, *Carbon* 2021, **180**, 92.

CAS | Web of Science® | Google Scholar

157 a) L. Xiao, Z. Wang, J. Guan, *Coord. Chem. Rev.* 2022, **472**, 214777;

CAS | Web of Science® | Google Scholar

b) X. Wen, Q. Zhang, J. Guan, *Coord. Chem. Rev.* 2020, **409**, 213214.

CAS | Web of Science® | Google Scholar

158 W. Li, J. Wang, J. Chen, K. Chen, Z. Wen, A. Huang, *Small* 2022, **18**, 2202018.

CAS | PubMed | Web of Science® | Google Scholar

159 Q. Miao, S. Yang, Q. Xu, M. Liu, P. Wu, G. Liu, C. Yu, Z. Jiang, Y. Sun, G. Zeng, *Small Struct* 2022, **3**, 2100225.

CAS | Web of Science® | Google Scholar

160 S. Das, G. Kumar, M. Das, R. Dey, presented at *Int. Symp. Mater. Millen. – Emerg. Trends Future Prosp.*, Pandit Deendayal Petr Univ, Raysan, India Nov 19–21, 2021.

Google Scholar

161 L. Zhai, S. Yang, X. Yang, W. Ye, J. Wang, W. Chen, Y. Guo, L. Mi, Z. Wu, C. Soutis, Q. Xu, Z. Jiang, *Chem. Mater.* 2020, **32**, 9747.

CAS | Web of Science® | Google Scholar

162 M. Liu, S. Liu, C. Cui, Q. Miao, Y. He, X. Li, Q. Xu, G. Zeng, *Angew. Chem., Int. Ed.* 2022, **61**, e202213522.

CAS | PubMed | Web of Science® | Google Scholar

163 Q. Zuo, G. Cheng, W. Luo, *Dalton Trans.* 2017, **46**, 9344.

CAS | PubMed | Web of Science® | Google Scholar

164 Y. Mo, S. Liu, G. Liu, G. Wang, W. Lu, *ChemNanoMat* 2022, **8**, 202200330.

CAS | Web of Science® | Google Scholar

165 J. Chen, L. Li, Y. Cheng, Y. Huang, C. Chen, *Int. J. Hydrogen Energy* 2022, **47**, 16025.

CAS | Web of Science® | Google Scholar

166 Q. Xu, J. Qian, D. Luo, G. Liu, Y. Guo, G. Zeng, *Adv. Sustainable Syst.* 2020, **4**, 2000115.

CAS | Web of Science® | Google Scholar

167 Z. Zhu, B. Yu, S. Chen, Y. Wang, X. Li, L. Lv, *J. Power Sources* 2022, **542**, 231583.

CAS | Google Scholar

168 Z. Wang, L. Zhou, R. Li, K. Qu, L. Wang, W. Kang, H. Li, S. Xiong, *Microporous Mesoporous Mater.* 2022, **330**, 111609.

CAS | Google Scholar

169 Y. Huang, F. Kong, H. Tian, F. Pei, Y. Chen, G. Meng, Z. Chang, C. Chen, X. Cui, J. Shi, A. Sustain, *Chem. Eng.* 2022, **10**, 6370.

CAS | Google Scholar

170 A. Garcia, T. Haynes, M. Retuerto, P. Ferrer, L. Pascual, M. Pena, M. Salam, M. Mokhtar, D. Gianolio, S. Rojas, *Ind. Eng. Chem. Res.* 2021, **60**, 18759.

CAS | PubMed | Web of Science® | Google Scholar

171 Y. Guo, S. Yang, Q. Xu, P. Wu, Z. Jiang, G. Zeng, *J. Mater. Chem. A* 2021, **9**, 13625.

CAS | Web of Science® | Google Scholar

172 M. Zhou, M. Liu, Q. Miao, H. Shui, Q. Xu, *Adv. Mater. Interfaces* 2022, **9**, 2201263.

CAS | Google Scholar

173 H. Liu, L. Hu, W. Cai, X. Feng, F. Zhang, R. Shao, L. Wang, B. Wang, *ChemElectroChem* 2022, **9**, 202200123.

CAS | Web of Science® | Google Scholar

174 S. Lin, C. Diercks, Y. Zhang, N. Kornienko, E. Nichols, Y. Zhao, A. Paris, D. Kim, P. Yang, O. Yaghi, C. Chang, *Science* 2015, **349**, 1208.

CAS | PubMed | Web of Science® | Google Scholar

175 M. Li, H. Wang, W. Luo, P. Sherrell, J. Chen, J. Yang, *Adv. Mater.* 2020, **32**, 2001848.

CAS | PubMed | Web of Science® | Google Scholar

176 B. Han, X. Ding, B. Yu, H. Wu, W. Zhou, W. Liu, C. Wei, B. Chen, D. Qi, H. Wang, K. Wang, Y. Chen, B. Chen, J. Jiang, *J. Am. Chem. Soc.* 2021, **143**, 7104.

CAS | PubMed | Web of Science® | Google Scholar

177 S. Chi, Q. Chen, S. Zhao, D. Si, Q. Wu, Y. Huang, R. Cao, *J. Mater. Chem. A* 2022, **10**, 4653.

CAS | Web of Science® | Google Scholar

178 J. Kurisingal, H. Kim, J. Choe, C. Hong, *Coord. Chem. Rev.* 2022, **473**, 214835.

Web of Science® | Google Scholar

179 Y. Wang, H. Ding, X. Ma, M. Liu, Y. Yang, Y. Chen, S. Li, Y. Lan, *Angew. Chem., Int. Ed.* 2022, **61**, e202114648.

CAS | PubMed | Web of Science® | Google Scholar

180 Y. Yang, Y. Wang, L. Dong, Q. Li, L. Zhang, J. Zhou, S. Sun, H. Ding, Y. Chen, S. Li, Y. Lan, *Adv. Mater.* 2022, **34**, 2206706.

CAS | PubMed | Web of Science® | Google Scholar

181 S. Ali, R. Iqbal, F. Wahid, P. M. Ismail, A. Saleem, S. Ali, F. Raziq, S. Ullah, I. Ullah, M. Tahir, X. Wu, H. Xiao, X. Zu, L. Qiao, *Fuel Process. Technol.* 2022, **237**, 107451.

CAS | Google Scholar

182 C. He, D. Si, Y. Huang, R. Cao, *Angew. Chem., Int. Ed.* 2022, **61**, 202207478.

CAS | PubMed | Web of Science® | Google Scholar

183 M. Mao, M. Zhang, D. Meng, J. Chen, C. He, Y. Huang, R. Cao, *ChemCatChem* 2020, **12**, 3530.

CAS | Web of Science® | Google Scholar

184 X. Qiu, J. Huang, C. Yu, Z. Zhao, H. Zhu, Z. Ke, P. Liao, X. Chen, *Angew. Chem., Int. Ed.* 2022, **61**, 202206470.

CAS | PubMed | Web of Science® | Google Scholar

185 J. Du, L. Guo, *Catal. Lett.* 2022, **153**, 3270.

Web of Science® | Google Scholar

186 S. An, X. Li, S. Shang, T. Xu, S. Yang, C. Cui, C. Peng, H. Liu, Q. Xu, Z. Jiang, J. Hu, *Angew. Chem., Int. Ed. Engl.* 2023, **62**, 202218742.

CAS | PubMed | Web of Science® | Google Scholar

187 X. Huang, C. Sun, X. Feng, *Science China-Chemistry* 2020, **63**, 1367.

CAS | Web of Science® | Google Scholar

188 F. Haase, B. Lotsch, *Chem. Soc. Rev.* 2020, **49**, 8469.

CAS | PubMed | Web of Science® | Google Scholar

189 M. Liu, Y. Liu, J. Dong, Y. Bai, W. Gao, S. Shang, X. Wang, J. Kuang, C. Du, Y. Zou, J. Chen, Y. Liu, *Nat. Commun.* 2022, **13**, 1411.

PubMed | Web of Science® | Google Scholar

190 J. Mahmood, E. Lee, M. Jung, D. Shin, I. Jeon, S. Jung, H. Choi, J. Seo, S. Bae, S. Sohn, N. Park, J. Oh, H. Shin, J. Baek, *Nat. Commun.* 2015, **6**, 6486.

CAS | PubMed | Web of Science® | Google Scholar

191 a) C. Huang, Y. Li, N. Wang, Y. Xue, Z. Zuo, H. Liu, Y. Li, *Chem. Rev.* 2018, **118**, 7744;

CAS | PubMed | Web of Science® | Google Scholar

b) X. Bai, J. Guan, *Chin. J. Catal.* 2022, **43**, 2057.

CAS | Web of Science® | Google Scholar

192 H. Huang, F. Li, Y. Zhang, Y. Chen, *J. Mater. Chem. A* 2019, **7**, 5575.

CAS | Web of Science® | Google Scholar

193 R. Bao, Z. Xiang, Z. Qiao, Y. Yang, Y. Zhang, D. Cao, S. Wang, *Angew. Chem., Int. Ed.* 2022.

PubMed | Google Scholar

194 J. Li, P. Liu, J. Mao, J. Yan, W. Song, *Nanoscale* 2022, **14**, 6126.

CAS | PubMed | Web of Science® | Google Scholar

195 H. Li, J. Ding, X. Guan, F. Chen, C. Li, L. Zhu, M. Xue, D. Yuan, V. Valtchev, Y. Yan, S. Qiu, Q. Fang, *J. Am. Chem. Soc.* 2020, **142**, 13334.

CAS | PubMed | Web of Science® | Google Scholar

196 J. Yao, Y. Lu, H. Sun, X. Zhao, *Chem. Res. Chin. Univ.* 2022, **38**, 364.

CAS | Web of Science® | Google Scholar

197 J. Segura, S. Royuela, M. Ramos, *Chem. Soc. Rev.* 2019, **48**, 3903.

CAS | PubMed | Web of Science® | Google Scholar

198 L. Hao, S. Jia, X. Qiao, E. Lin, Y. Yang, Y. Chen, P. Cheng, Z. Zhang, *Angew. Chem., Int. Ed. Engl.* 2023, **62**, 202217240.

CAS | PubMed | Google Scholar

199 Y. Yao, R. Zhang, T. Liu, H. Yu, G. Lu, *Inorg. Chem. Commun.* 2019, **101**, 160.

CAS | Web of Science® | Google Scholar

200 Y. Ma, Y. Fu, Y. Han, J. Li, W. Jiang, Y. Lu, C. Liu, G. Che, B. Hu, *CrystEngComm* 2022, **24**, 7447.

CAS | Web of Science® | Google Scholar

201 M. Zhang, D. Si, J. Yi, S. Zhao, Y. Huang, R. Cao, *Small* 2020, **16**, 2005254.

CAS | PubMed | Web of Science® | Google Scholar

202 J. Kim, D. Kang, H. Yun, M. Kang, N. Singh, J. Kim, C. Hong, *Chem. Soc. Rev.* 2022, **51**, 43.

CAS | PubMed | Web of Science® | Google Scholar

203 H. Aiyappa, J. Thote, D. Shinde, R. Banerjee, S. Kurungot, *Chem. Mater.* 2016, **28**, 4375.

CAS | Web of Science® | Google Scholar

204 M. Liu, Y. Wang, H. Ding, M. Lu, G. Gao, L. Dong, Q. Li, Y. Chen, S. Li, Y. Lan, *Sci. Bull.* 2021, **66**, 1659.

CAS | PubMed | Web of Science® | Google Scholar

205 R. Liu, K. Tan, Y. Gong, Y. Chen, Z. Li, S. Xie, T. He, Z. Lu, H. Yang, D. Jiang, *Chem. Soc. Rev.* 2021, **50**, 120.

CAS | PubMed | Web of Science® | Google Scholar

206 H. Lyu, C. Diercks, C. Zhu, O. Yaghi, *J. Am. Chem. Soc.* 2019, **141**, 6848.

CAS | PubMed | Web of Science® | Google Scholar

207 C. Wang, Z. Lv, W. Yang, X. Feng, B. Wang, *Chem. Soc. Rev.* 2023.

Google Scholar

208 B. Cui, G. Fu, *Nanoscale* 2022, **14**, 1679.

CAS | PubMed | Web of Science® | Google Scholar

209 C. Tang, M. Titirici, Q. Zhang, *J. Energy Chem.* 2017, **26**, 1077.

Web of Science® | Google Scholar

210 Y. Zhi, Z. Wang, H. Zhang, Q. Zhang, *Small* 2020, **16**, 2001070.

CAS | PubMed | Web of Science® | Google Scholar

211 C. You, X. Jiang, X. Wang, Y. Hua, C. Wang, Q. Ling, S. Liao, *ACS Appl. Energy Mater.* 2018, **1**, 161.

CAS | Web of Science® | Google Scholar

212 M. Liu, X. Zhu, Y. Song, G. Huang, J. Wei, X. Song, Q. Xiao, T. Zhao, W. Jiang, X. Li, W. Luo, *Adv. Funct. Mater.* 2023, **33**, 2213395.

CAS | Web of Science® | Google Scholar

213 M. Zhang, C. Lai, F. Xu, D. Huang, S. Liu, Y. Fu, L. Li, H. Yi, L. Qin, L. Chen, *Coord. Chem. Rev.* 2022, **466**, 214592.

CAS | Web of Science® | Google Scholar

214 S. Roy, S. Mari, M. Sai, S. Sarma, S. Sarkar, S. Peter, *Nanoscale* 2020, **12**, 22718.

CAS | PubMed | Web of Science® | Google Scholar

215 H. Zhao, X. Zhang, Y. Zhang, Y. Song, C. Li, K. Liu, D. Ma, *J. Mater. Chem. A* 2022, **10**, 25272.

CAS | Web of Science® | Google Scholar

216 W. Wang, L. Zhang, T. Wang, Z. Zhang, X. Wang, C. Cheng, X. Liu, *J. Energy Chem.* 2023, **77**, 543.

CAS | Web of Science® | Google Scholar

217 Y. Chen, Q. Zhou, J. Zheng, A. Sustain, *Chem. Eng.* 2022, **10**, 1961.

CAS | Google Scholar

218 J. Xu, W. Tang, C. Yang, I. Manke, N. Chen, F. Lai, T. Xu, S. An, H. Liu, Z. Zhang, Y. Cao, N. Wang, S. Zhao, D. Niu, R. Chen, *ACS Energy Lett.* 2021, **6**, 3053.

CAS | Web of Science® | Google Scholar

219 S. Yang, Q. Xu, P. Qiao, J. Liu, X. Chen, Z. Tian, N. Zhang, S. Kim, S. Lu, X. Liu, X. Li, Z. Jiang, *Mater. Today Chem.* 2022, **24**, 100936.

CAS | Google Scholar

220 C. Guo, F. Duan, S. Zhang, L. He, M. Wang, J. Chen, J. Zhang, Q. Jia, Z. Zhang, M. Du, *J. Mater. Chem. A* 2022, **10**, 475.

CAS | Web of Science® | Google Scholar

221 G. Zhuang, Y. Gao, X. Zhou, X. Tao, J. Luo, Y. Gao, Y. Yan, P. Gao, X. Zhong, J. Wang, *Chem. Eng. J.* 2017, **330**, 1255.

CAS | Web of Science® | Google Scholar

222 Z. Zhou, P. Li, X. Gao, J. Chen, K. Akhtar, E. Bakhsh, S. Khan, Y. Shen, M. Wang, *J. Environ. Chem. Eng.* 2022, **10**, 106900.

CAS | Web of Science® | Google Scholar

223 N. Zhang, Z. Yang, W. Liu, F. Zhang, H. Yan, *Catalysts* 2023, **13**, 90.

CAS | Google Scholar

224 X. Bai, J. Guan, *Small Struct.* 2023, **4**, 2200354.

CAS | Web of Science® | Google Scholar

225 a) K. Shah, R. Dai, M. Mateen, Z. Hassan, Z. Zhuang, C. Liu, M. Israr, W. Cheong, B. Hu, R. Tu, C. Zhang, X. Chen, Q. Peng, C. Chen, Y. Li, *Angew. Chem., Int. Ed.* 2022, **61**, 202114951;

CAS | PubMed | Web of Science® | Google Scholar

b) S. Li, Q. Li, Y. Chen, Y. Zhao, L. Gan, *Appl. Surf. Sci.* 2022, **605**, 154828.

CAS | Google Scholar

226 J. Ji, C. Zhang, S. Qin, P. Jin, *Sustain. Energ Fuels* 2021, **5**, 5615.

CAS | Web of Science® | Google Scholar

227 S. Wei, Y. Wang, W. Chen, Z. Li, W. Cheong, Q. Zhang, Y. Gong, L. Gu, C. Chen, D. Wang, Q. Peng, Y. Li, *Chem. Sci.* 2020, **11**, 786.

CAS | Web of Science® | Google Scholar

228 S. Yang, X. Li, T. Tan, J. Mao, Q. Xu, M. Liu, Q. Miao, B. Mei, P. Qiao, S. Gu, F. Sun, J. Ma, G. Zeng, Z. Jiang, *Appl. Catal., B* 2022, **307**, 121147.

CAS | Web of Science® | Google Scholar

Citing Literature

Download PDF